Effect of Thermal Ageing on the Corrosion and Stress Corrosion Cracking of Type 310S Stainless Steel in Supercritical Water

By Yinan Jiao, B. E.

A Thesis Submitted to the School of Graduate Studies in Partial Fulfillment of the Requirements for the Degree Doctor of Philosophy

McMaster University

Doctor of Philosophy (2017) McMaster University

Department of Materials Science and Engineering Hamilton, Ontario

Title: Effect of Thermal Ageing on the Corrosion and Stress Corrosion Cracking of Type 310S Stainless Steel in Supercritical Water

Author: Yinan Jiao, B. E., (Inner Mongolia University of Science and Technology)

Supervisor: Prof. Joseph Kish and Prof. Wenyue Zheng

Number of pages: CCXXVIII, 228

Abstract

This thesis documents a multi-faceted investigation of the effects of thermal ageing-induced microstructure instability on the corrosion/oxidation and stress corrosion cracking (SCC) susceptibility of Type 310S stainless steel in supercritical water (SCW). The motivation for this study is the exiting knowledge gap associated with these two material performance aspects, which are considered essential to help guide the selection of a fuel cladding material for application in the Canadian Gen IV Supercritical Water-Cooled Reactor (SCWR) design concept. The focus was placed on the pressurized light water coolant outlet conditions (25 MPa SCW at 500-550 °C) considering that the likelihood for corrosion and SCC in combination with microstructure instability resulting from thermal ageing is presumed to be relatively high. The working hypotheses being that (i) Cr-rich intermetallic precipitate formation would serve to bind alloyed Cr, thus preventing the formation of protective Cr-rich oxide scales required for suitable corrosion/oxidation performance and (ii) Cr-rich grain boundary precipitate formation would serve to enhance SCC susceptibility by either sensitizing (chemical factor) or embrittling (mechanical factor) grain boundaries.

Two limiting thermal ageing treatments were evaluated. The ‘S’ treatment, designed to ‘sensitize’ the microstructure, induced significant Cr-rich $M_{23}C_6$ carbide precipitation on the grain boundaries concomitant with the development of adjacent

Cr-depleted zones. This limiting case represented a short-term exposure condition for the fuel cladding. The ‘TT’ treatment, designed to ‘mechanically embrittle’ the microstructure, induced significant Cr-rich sigma (σ)-phase precipitate formation on the grain boundaries and within the grains. This limiting case represented a long-term exposure condition for the fuel cladding. The ‘SA’ treatment, designed to solution anneal the microstructure, served as the baseline microstructure exhibiting a low extent of microstructure instability.

Long term thermal ageing of Type 310S austenitic stainless steel at the maximum expected fuel cladding temperature operation temperature range of Canadian-SCWR concept to produce the TT material induced significant σ phase precipitate formation within the grains and on grain boundaries, all without the concomitant adjacent Cr-depleted zone formation. Such microstructure instability did not have a major effect on the general corrosion/oxidation susceptibility since the thermally-aged material exhibited a similar weight gain and oxide scale structure after exposure in 25 MPa SCW at 550 °C as the solution annealed material, albeit after relative short exposure time (500 h). The likely reason for this was the discontinuous nature of the σ phase precipitate formation.

The remaining research conducted was aimed towards investigating the effect of thermal ageing on the intergranular SCC susceptibility of Type 310S stainless steel in SCW. A ‘first approximation’ attempt to isolate and assess the potential contribution of the likely chemical factor (sensitization) and mechanical factor (embrittlement) to the overall cracking mechanism. The overall ranking in terms of an increasing degree of sensitization, as determined by Double Loop – Electrochemical Potentiokinetic Reactivation (DL-EPR) testing, of three heat-treated materials studied is: SA ~ TT << S. The ranking reflects the controlling role played by Cr-depleted zones, which were only observed in the S material. The absence of a Cr-depleted zone accompanying the σ phase grain boundary precipitates in the TT material indicates that the treatment time of a 1000 h was sufficient to “self-heal” the Cr-depleted zone, which was expected to have formed during the early stages of the treatment at 800 °C.

Bulk uniaxial tensile measurements revealed both the S and TT material were embrittled relative to the SA material. The associated fractography revealed that the grain boundaries in the S material were sufficiently embrittled to cause intergranular fracture, whereas the grain boundaries in the TT material were not sufficiently embrittled to cause intergranular fracture. Classic micro-void formation involving a $M_{23}C_6$/matrix decohesion process occurs on the S material grain boundaries. Intergranular facture occurs as these micro-voids coalesce on the grain boundaries. In contrast, micro-void formation involving cracking of the large hard σ phase precipitates occurs on the TT material grain boundaries. Transgranular ductile fracture of the softer austenite matrix occurs as these micro-voids coalesce across the grains as the softer grains need to accommodate the stress after fracture of hard σ phase

precipitates.

The effect of thermal ageing on the SCC susceptibility of Type 310S in SCW was evaluated using the Slow Strain Rate Test (SSRT) technique, straining samples to 10% in 25 MPa SCW at 500 °C. The results were interpreted in light of the likely contributions of the chemical (sensitization) and mechanical (embrittlement) factors as revealed by the above mentioned research. The sensitized material exhibited well-developed intergranular SCC after straining to 10% (about 7.5% plastic strain). The TT material exhibited neither intergranular nor transgranular SCC susceptibility under the same exposure conditions. The localized deformation model for SCC initiation was combined with a void-assisted film-cleavage model for SCC propagation to explain the SCC susceptibility of thermally-aged Type 310S stainless steel in SCW.

Acknowledgements

Firstly, I would like to express my deepest gratitude to my supervisors Prof. Joey Kish and Prof. Wenyue Zheng for their support and guidance. Thanks a lot for your patience and supervision during my Ph.D. study. It’s my honor to have such a great chance to working with you both. Your enthusiasm, inspiration and efforts to clearly explain concepts helped me during my study and set me on the right path to become a research scientist.

I also would like to thank my committee members, Prof. Joe McDermid and Dr. Dave Guzonas for their valuable time in evaluating my work and provide suggestions and comments. Additionally, I also appreciate suggestions, discussions and guidance from Prof. Ken Coley (McMaster University), Prof. Gu Xu (McMaster University), Prof. Roger Newman (University of Toronto), Prof. Wiliam Cook (University of New Brunswick), Prof. Mark Daymond (Queens University), Prof. Gary Was (University of Michigan), Prof. Robert Klassen (Western University), Dr. Jian Li (CanmetMATERIALS) and Dr. Yimin Zeng (CanmetMATERIALS).

I would like to express my profound thanks to the CAMC group members and friends Shooka Mahboubi, Mehdi Taheri, Stephen Jones, Jenny Thuss, Yaning Hu, Darren Feenstra, Zach Cano, Sara Filice, Dan Tapp and Qiang Wang. Technical assistance and support from technicians and staff members at McMaster University, Xiaogang Li, Vicky Jarvis, Chris Butcher, Steve Koprich, Travis Casagrande, Andrei

Carmen are also greatly appreciated.

Last, but not least, I wish to express my appreciation to my family. I would like to thank my dear parents for their unselfish support. I also would like to thank my wife Xiaohui Jia for her patience, encouragement and support both in my study and life.

Declaration of Academic Achievements

This dissertation was used to fulfill the requirement of Ph.D. degree. The major research project was undertaken from September 2011 to December 2016. Over the course of this thesis study, I carried out experimental and theoretical research on general corrosion and stress corrosion cracking of Type 310S stainless steel in supercritical water environment. The major contribution of this study came from my supervisor and me.

The results of this dissertation were published in 6 papers in peer-reviewed journals, in which I was the first author on these papers. The papers were listed below.

1. Yinan Jiao, Wenyue Zheng, David Guzonas, William Cook and Joseph Kish, Effect of thermal treatment on the corrosion resistance of Type 316L stainless steel exposed in supercritical water. ***Journal of Nuclear Materials***, 464 (2015) 356-364.
2. Yinan Jiao, Joseph Kish, Graham Steeves, William Cook, Wenyue Zheng and David Guzonas, Effect of thermal pretreatment on the corrosion of stainless steel in flowing supercritical water. ***Journal of Nuclear Engineering and Radiation Science***, 2 (2016) 011015.
3. Yinan Jiao, Wenyue Zheng, David Guzonas and Joseph Kish. Microstructure instability of candidate fuel cladding alloys: corrosion and stress corrosion

cracking implications, ***JOM***, 68 (2016) 485-489.

4. Yinan Jiao, Jamshad Mahmood, Wenyue Zheng, Preet Singh and Joseph Kish. Effect of thermal ageing on the intergranular stress corrosion cracking susceptibility of Type 310S stainless steel, accepted for publication in ***Corrosion***, November 2017.
5. Yinan Jiao, Qiang Wang, Wenyue Zheng, Joseph McMermid, Mark Daymond and Joseph Kish. Manuscript to be submitted to ***Materials Science and Engineering A***, January 2018.
6. Yinan Jiao, Wenyue Zheng, Joseph Kish. Stress corrosion cracking susceptibility of thermally-aged Type 310S stainless steels in supercritical water, revised manuscript (minor revisions) submitted to ***Corrosion Science***, December 2017.

Tables of Contents

List of Figures

List of Tables

Abbreviations

SCW	SuperCritical Water
SCWR	SuperCritical Water-cooled Reactor
LWR	Light Water Reactor
AFM	Atomic Force Microscopy
BWR	Boiling Water Reactor
PWR	Pressurized Water Reactor
CERT	Constant Extension Rate Test
SSRT	Slow Strain Rate Test
CW	Cold Working
DO	Dissolved Oxygen
EBSD	Electron Back-Scattered Diffraction
SEM	Scanning Electron Microscopy
SLM	Standard Light Microscopy
TEM	Transmission Electron Microscopy
STEM	Scanning Transmission Electron Microscopy
HAADF	High Angle Annular Dark Field
EELS	Electron Energy Loss Spectroscoty
IG	Intergranular
SCC	Stress Corrosion Cracking

TG	Transgranular
IGSCC	Intergranular Stress Corrosion Cracking
TGSCC	Transgranular Stress Corrosion Cracking
IASCC	Irradiation Assisted Stress Corrosion Cracking
RIS	Radiation Induced Segregation
SAD	Selected Area Diffraction
DL-EPR	Double Loop – Electrochemical Potentiokinetic Reactivation

Preface

This thesis summarizes the findings of effects of thermal treatment on the corrosion and stress corrosion cracking of Type 310S stainless steel in SCW environment. The thesis is organized as a “sandwich” thesis consisting of 8 chapters: an introductory chapter; a literature review chapter; four chapters written as manuscripts that have been submitted for publication; a draft article written as manuscripts to be submitted for publication; and a concluding chapter.

I was responsible for conceiving the research questions, developing the research protocol, collecting and analyzing the data, and writing the manuscripts. The study was approved by the McMaster Research Ethics Board at McMaster University (Hamilton, Ontario).

1. Introduction

1.1 Overall Context

With the increasing concern of greenhouse gases and global warming, a considerable effort has been devoted towards replacing current fossil fuel electrical power plants with clean nuclear power plants [1-11]. As one of Generation IV reactors, the supercritical water-cooled reactor (SCWR) design concept is expected to be a promising future nuclear power system due the fact that the concept is based on two successful current-generation power generation system designs: namely the boiling water reactor (BWR) design and fossil-fueled supercritical water (SCW) plant design, with higher thermal efficiency and smaller volume than current generation light water reactor (LWR) design [2, 6, 8, 9]. The Canadian SCWR core and fuel channel design concepts are illustrated in Figure 1.1. During operation, "cold" pressurized (25 MPa) light water coolant (350 °C) enters the reactor through the inlet valve and flows towards the bottom of reactor through the fuel channels from an inlet plenum. Driven by turbines, the "cold" pressurized light water coolant then flows upwards through reactor fuel channels and becomes "heated" along the way as it extracts heat from the cladded fuel element. The "hot" pressurized light water coolant then exits the reactor from the outlet plenum and flows towards the turbines.

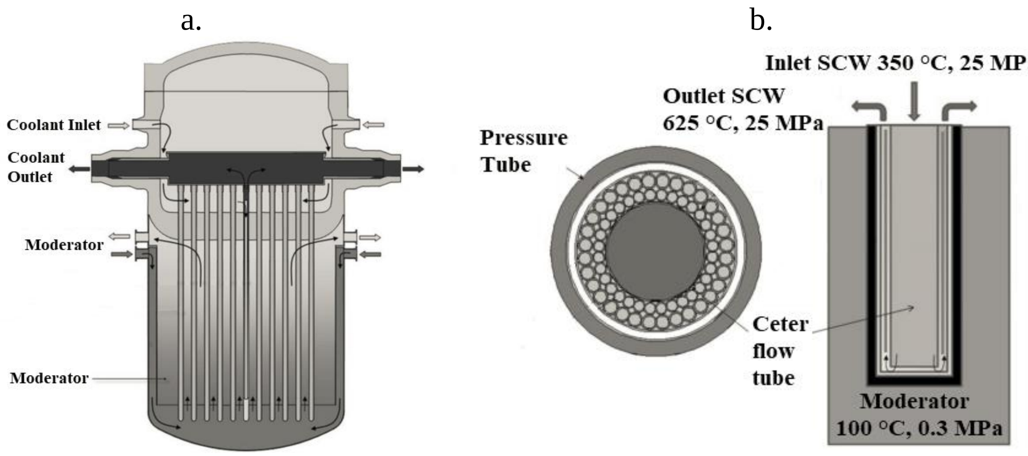

Figure 1.1 Schematic of Canadian SCWR: (a): core design and (b): fuel channel concept reproduced from [12].

Selection of a suitable fuel cladding material remains elusive, regardless of the details specific to a given SCWR design concept [2, 6, 9]. From a materials performance perspective, severe conditions are expected during operation including a wide range of temperatures at high pressure and a high dose of neutron irradiation [2, 6, 9]. Thus, the cladding material is required to possess, among other factors, a high resistance to both general corrosion/oxidation, stress corrosion cracking (SCC) and irradiation damage, including irradiation-assisted stress corrosion cracking (IASCC) in particular [2-5, 7, 8]. As an example, Figure 1.2 superimposes some of the more prominent expected irradiation damage modes onto the expected temperature variation along the length of the fuel channel in the Canadian SCWR design concept [2].

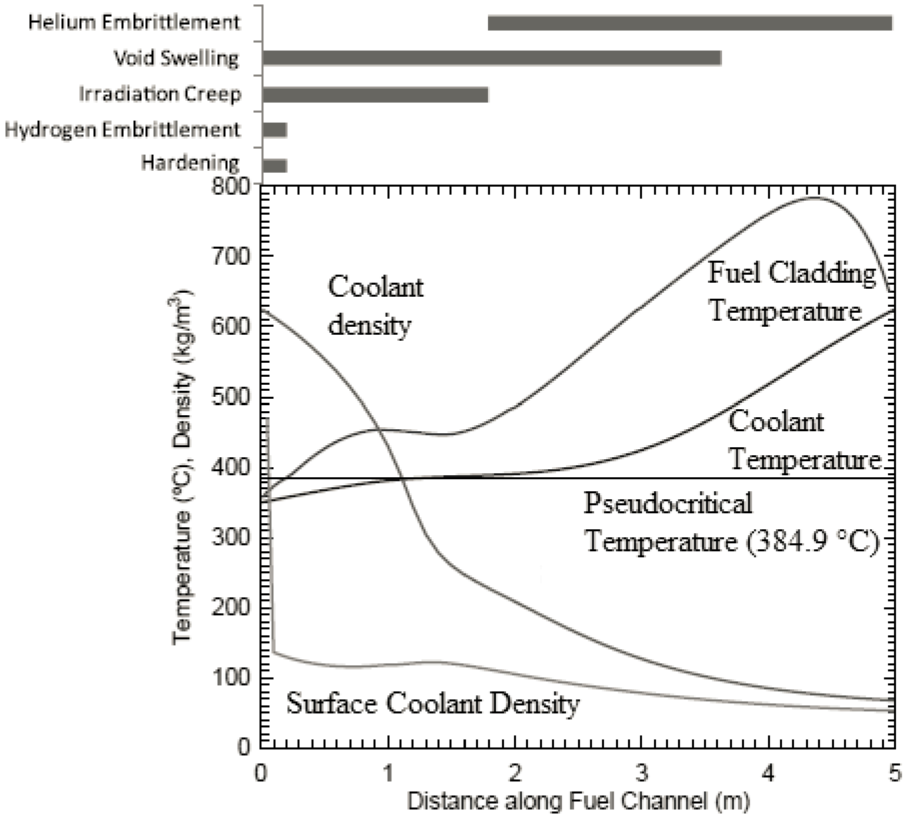

Figure 1.2 Expected bulk and surface SCW coolant density and surface cladding temperature profiles along the heated section of the Canadian SCWR fuel channel. Superimposed bar chart (top) showing temperature range associated with irradiation damage modes expected throughout the core reproduced from [2].

Austenitic 300-series stainless steels are widely used as structural materials in current generation LWRs due to their relatively good corrosion, SCC, and radiation damage resistance in combination with their high temperature mechanical integrity [1-5, 13]. Naturally, they have been considered for the fuel claddings in the Generation IV SCWR design concepts, for which extensive supportive corrosion and SCC testing has been conducted in supercritical water (SCW) environments [2, 6]. For example, Zr-modified versions of Type 316L and Type 310S stainless steels have been identified as the primary fuel cladding materials for Japan's SCWR pressure-vessel concept [6]. Similarly, Ti-stabilized Type 1.4970 stainless steel was initially identified as the primary fuel cladding material for the EU's SCWR pressure-vessel concept [2]. As for the Canadian SCWR design concept, the key materials performance indicators identified to qualify a suitable material are listed in Table 1.1 along with a qualitative relative performance ranking of the five short-listed candidate alloys [12]. The Green fill indicates that data is available that suggests the alloy meets the performance criterion under all of the major process conditions expected. Note that the alloys are assumed to be in the mill-annealed condition). The yellow fill indicates that some (or all) data suggests the alloy may not meet the performance criterion under some process conditions expected. The red fill indicates that some (or all) data suggests the alloy will not meet the performance criteria under some process conditions. The grey fill indicates that there is insufficient data available to make an assessment.

Table 1.1 Results of overall assessment of candidate alloys reproduced from [12]

Alloy	Corrosion	Oxide thickness	SCC	IASCC	Void swelling	Creep	Ductility	strength
347	🟩	🟨	🟩	🟨	🟥	🟩	▨	🟩
310S	🟩	🟩	🟩	▨	🟨	🟩	▨	🟨
800H	🟩	🟨	🟩	🟨	🟩	🟩	▨	🟩
625	🟩	🟩	🟩	🟨	🟩	🟩	▨	🟩
214	🟩	🟩	🟩	▨	▨	▨	▨	▨

Austenitic stainless steels have long been known to exhibit microstructure instability (including formation of secondary phases, radiation induced defects, redistribution of alloying elements for example) with prolonged exposed to both high temperature (thermal ageing) and radiation (irradiation damage) [1, 7, 8, 13-20]. Such microstructure instability has been found to degrade resistance to both corrosion and SCC in aqueous and LWR environments [1, 16, 19]. Among the set of materials properties listed in Table 1.1, SCC /IASCC resistance arguably are the most critical ones as all five candidate alloys have been shown to crack under specific conditions during slow strain rate testing (SSRT) in supercritical water [12].

IASCC has long been a major problem affecting 300-series austenitic stainless steels being utilized as core components in LWRs [7, 12]. It is now widely accepted that the concomitant increase in material hardness and the formation of Cr-depleted zones adjacent to grain boundaries from exposure to radiation are two predominant microstructure instability factors that control the intergranular SCC process [7, 21-23]. However, neither of these two factors have been found to control intergranular SCC initiation alone [21]. The onset of cracking in LWR environments is more likely controlled by permanent damage (microstructure instability) in the alloy that is introduced by radiation [22]. Thermal aging of irradiated alloys have been reported to relieve radiation-induced microstructure instabilities (defects and dislocations for example) [21, 22]. Radiation-induced segregation (RIS), however, cannot be easily removed by post-irradiation annealing [21] whereas the intergranular SCC susceptibility of irradiated alloys decreases with annealing temperature and time [21, 22]. Both Jiao [24] and Bruemmer et al. [25] reported various thresholds such as hardness, yield strength, stacking fault energy (SFE), dislocation loops, etc. above which intergranular IASCC occurred. These phenomena indicate that crack initiation and propagation are likely controlled by the mechanical properties of degraded microstructures.

By increasing temperature and pressure to the supercritical region, water tends to become more “gas-like” [9] than “liquid-like”, which suggests similar chemical factors (such as the enhanced anodic dissolution of Cr-depleted zones formed adjacent to grain boundaries) may have less control of the intergranular SCC process.

1.2 Research Objectives and Hypotheses

As introduced above, the effects of microstructure instability on the corrosion and SCC resistance of austenite stainless steels in SCW are not well understood at this time. The research embodied in this thesis dissertation aims to establish links between the microstructure instability expected from prolonged exposure to high temperature (thermal ageing) to exacerbated corrosion and SCC of Type 310S stainless steel: one of the five short-listed candidate fuel cladding material being considered in the Canadian SCWR design concept. The focus was placed on the pressurized light water coolant outlet conditions (25 MPa SCW at 500-550 °C) considering that the likelihood for corrosion and SCC in combination with microstructure instability resulting from thermal ageing is presumed to be relatively high. Two limiting thermal ageing treatments were evaluated. The ‘S’ treatment, designed to ‘sensitize’ the microstructure, induced significant Cr-rich $M_{23}C_6$ carbide precipitation on the grain boundaries concomitant with the development of adjacent Cr-depleted zones. This limiting case represented a short-term exposure condition for the fuel cladding. The ‘TT’ treatment, designed to mechanically embrittle the microstructure, induced significant Cr-rich sigma (σ)-phase precipitate formation on the grain boundaries and within the grains. This limiting case represented a long-term exposure condition for the fuel cladding. The ‘SA’ treatment, designed to solution anneal the microstructure, served as the baseline microstructure exhibiting a low extent of microstructure instability.

In terms of corrosion susceptibility, it is now well established that a chromia (Cr_2O_3)-based surface scale, formed in-situ during exposure in SCW, are more protective than a spinel ($FeCr_2O_4$)-based scale [9, 26, 27]. Formation of the protective (Cr_2O_3)-based scale relies the presence of short-circuit paths for Cr diffusion from the bulk to the surface such as grain boundaries and dislocations [28]. Thermal ageing is expected to cause a significant amount microstructure instability including the formation of Cr-rich intermetallic precipitates within grains and on grain boundaries with possible Cr-depleted zone formation adjacent to such precipitates [29-31]. One concern is that the intermetallic precipitates binds Cr locally on the short-circuit diffusion paths, making less Cr available for diffusion and subsequent Cr_2O_3-based scale formation. Another concern is that the Cr-rich intermetallic precipitates may also act as a physical barrier when located on short diffusion paths, thus blocking the outward diffusion of Cr to the surface. Thus, the hypothesis here is that such Cr-rich intermetallic precipitates formed on grain boundaries will exacerbate corrosion and some means of microstructure ‘stabilization’ may be necessary to control corrosion.

In terms of SCC susceptibility, the reported correlation between increased intergranular SCC of pre proton-irradiated austenitic stainless steel in SCW with simultaneous increased hardness and degree of RIS [32, 33] raises an important question about which factor, chemical (sensitization) or mechanical (embrittlement) controls the mechanism. A better understanding of the key factors involved is paramount to any future attempt to modify the microstructure to control intergranular SCC. While it is understood that the contribution of each factor, and possible interactions between them, can be complex, a “first approximation” attempt to isolate and assess the potential contribution of each factor to the IGSCC susceptibility in SCW is warranted. Thus, the hypothesis here is that a thermal ageing will exacerbate intergranular SCC and that a grain boundary ‘sensitivity’ map can be constructed and then correlated with the intergranular SCC susceptibility as measured in SCW to distinguish which factor (chemical and/or mechanical) controls the process. The envisioned map plots an appropriate chemical factor (such as the degree of sensitization) against an appropriate mechanical factor (such as degree of grain boundary embrittlement) for various degraded microstructures including, but not limited to, thermal ageing.

1.3 Thesis Layout

The remainder of this thesis contains seven subsequent chapters. A description of the contents and how they relate to one another is provided below.

- Chapter 2 presents a literature review of the current state of knowledge pertaining to the corrosion and SCC susceptibility of austenitic stainless steel (Fe-Cr-Ni) alloys in SCW environments.
- Chapter 3 reproduces an invited published article that provides a concise literature review of the microstructure instability expected from prolonged exposure of the fuel cladding to both high temperature (thermal ageing) and radiation (irradiation damage) and the associated corrosion and SCC implications for the Canadian SCWR design concept [2, 9]. The article was invited to be part of a special issue dedicated to the current status (at the time of publication) of materials selection for the Canadian SCWR design concept. The implications section in this article provides the rationale underpinning research described in this thesis (next four Chapters).
- Chapter 4 reproduces another published article, which documents the research conducted to elucidate the effect of thermal ageing on the corrosion behaviour of Type 310S stainless steel in SCW. The Results and Discussion sections in the

article (chapter) specifically address the corrosion implications of a long-term thermally-aged microstructure in SCW described in Section 1.2 above and in the Corrosion Implications Section in Chapter 3.

- Chapter 5 reproduces a submitted article, which documents the research conducted to isolate and assess the intergranular SCC susceptibility of the two limiting thermally-aged Type 310S stainless steel conditions relative to the baseline in terms of the contributing chemical factors only (degree of grain boundary sensitization in particular). This article is the first of three that, as a set, specifically address the SCC implications of both short-term and long-term thermally-aged microstructures in SCW described in Section 1.2 above and in the Stress Corrosion Cracking Implications Section in Chapter 3. The relative intergranular SCC susceptibility of the thermally-aged materials was evaluated in terms of the degree of sensitization (chemical factor) determined using the double loop electrochemical potentiokinetic reactivation (DL-EPR) technique and validated through slow strain rate testing (SSRT) technique using a pressurized hot alkaline solution. The latter solution is known to promote intergranular SCC in stainless steel that is driven predominantly by chemical factors (preferential anodic dissolution of the Cr-depleted zones).
- Chapter 6 presents a draft article (not yet submitted for publication), which documents research conducted to isolate and assess the intergranular SCC

susceptibility of the two limiting thermally-aged Type 310S stainless steel conditions relative to the baseline in terms of the contributing mechanical factors only (degree of grain boundary embrittlement). This article is the second of three that, as a set, specifically address the SCC implications of both short-term and long-term thermally-aged microstructures in SCW described in Section 1.2 above and in the Stress Corrosion Cracking Implications Section in Chapter 3. Micro-mechanical measurements in combination with the uniaxial tensile measurements were conducted to provide key insight into how individual thermally-aged grain boundaries (micro-scale) controlled the bulk fracture (macro-scale) in the absence of a corrosive environment.

- Chapter 7 presents a draft article (not yet submitted for publication), which documents the research conducted to comparatively evaluate the intergranular SCC susceptibility of the two limiting thermally-aged Type 310S stainless steel conditions relative to the baseline in SCW. This article is the final of three that, as a set, specifically addresses the SCC implications of both short-term and long-term thermally-aged microstructures in SCW described in Section 1.2 above and in the Stress Corrosion Cracking Implications Section in Chapter 3. The results of SSRT measurements in 25 MPa SCW at 500 °C in combination with the post-exposure metallographic examinations were benchmarked against the findings presented of the two previous Chapters to elucidate key factors that likely control the intergranular SCC susceptibility of austenitic stainless steel exposed in SCW.

- Chapter 8 presents the set of integrated conclusions extracted from the preceding chapters, which reflects the general theme of this thesis (effect of thermal ageing on the corrosion and SCC behaviour of Type 310S stainless steel in SCW) and discusses the overall implications of the research findings.

References:

[1] E.A. Kenik, J.T. Busby, Radiation-induced degradation of stainless steel light water reactor internals, Materials Science and Engineering R: Reports, 73 (2012) 67-83.

[2] D. Guzonas, R. Novotny, Supercritical water-cooled reactor materials – Summary of research and open issues, Progress in Nuclear Energy, 77 (2014) 361-372.

[3] X. Ru, R.W. Staehle, Historical experience providing bases for predicting corrosion and stress corrosion in emerging supercritical water nuclear technology: Part 1 - Review, Corrosion, 69 (2013) 211-229.

[4] X. Ru, R.W. Staehle, Historical experience providing bases for predicting corrosion and stress corrosion in emerging supercritical water nuclear technology-part 2: Review, Corrosion, 69 (2013) 319-334.

[5] X. Ru, R.W. Staehle, Historical experience providing bases for predicting corrosion and stress corrosion in emerging supercritical water nuclear technology: Part 3-review, Corrosion, 69 (2013) 423-447.

[6] J. Kaneda, S. Kasahara, F. Kano, N. Saito, T. Shikama, H. Matsui, Material development for supercritical water-cooled reactor, Proc. ISSCWR-5, Vancouver, Canada, March, 13 (2011) 2011.

[7] G.S. Was, Y. Ashida, P.L. Andresen, Irradiation-assisted stress corrosion cracking, Corrosion Reviews, 29 (2011) 7-49.

[8] S.J. Zinkle, G.S. Was, Materials challenges in nuclear energy, Acta Materialia, 61 (2013) 735-758.

[9] D.A. Guzonas, W.G. Cook, Cycle chemistry and its effect on materials in a supercritical water-cooled reactor: a synthesis of current understanding, Corrosion Science, 65 (2012) 48-66.

[10] G.S. Was, P. Ampornrat, G. Gupta, S. Teysseyre, E.A. West, T.R. Allen, K. Sridharan, L. Tan, Y. Chen, X. Ren, C. Pister, Corrosion and stress corrosion cracking in supercritical water, Journal of Nuclear Materials, 371 (2007) 176-201.

[11] T.R. Allen, Y. Chen, X. Ren, K. Sridharan, L. Tan, G.S. Was, E. West, D. Guzonas, 5.12 - Material Performance in Supercritical Water, in: R.J.M. Konings (Ed.) Comprehensive Nuclear Materials, Elsevier, Oxford, 2012, pp. 279-326.

[12] W. Zheng, D. Guzonas, K.P. Boyle, J. Li, S. Xu, Materials Assessment for the Canadian SCWR Core Concept, JOM, 68 (2016) 456-462.

[13] S.J. Zinkle, P.J. Maziasz, R.E. Stoller, Dose dependence of the microstructural evolution in neutron-irradiated austenitic stainless steel, Journal of Nuclear Materials, 206 (1993) 266-286.

[14] P.J. Maziasz, Overview of microstructural evolution in neutron-irradiated austenitic stainless steels, Journal of Nuclear Materials, 205 (1993) 118-145.

[15] P. Shankar, H. Shaikh, S. Sivakumar, S. Venugopal, D. Sundararaman, H.S. Khatak, Effect of thermal aging on the room temperature tensile properties of AISI type 316LN stainless steel, Journal of Nuclear Materials, 264 (1999) 29-34.

[16] T. Sourmail, Precipitation in creep resistant austenitic stainless steels, Materials science and technology, 17 (2001) 1-14.

[17] T. Sourmail, H. Bhadeshia, Modelling simultaneous precipitation reactions in austenitic stainless steels, Calphad, 27 (2003) 169-175.

[18] L.P. Stoter, Thermal ageing effects in AISI type 316 stainless steel, Journal of Materials Science, 16 (1981) 1039-1051.

[19] B. Weiss, R. Stickler, Phase instabilities during high temperature exposure of 316 austenitic stainless steel, Metallurgical Transactions, 3 (1972) 851-866.

[20] Y. Jiao, J. Kish, W.G. Cook, G. Steeves, W. Zheng, D. Guzonas, Effect of Thermal Ageing on the Corrosion Resistance of Stainless Steels in Supercritical Water,

in: The 7th International Symposium on Supercritical Water-Cooled Reactors, Proc. ISSCWR-7, Helsinki, Finland, 2015.

[21] J.T. Busby, G.S. Was, E.A. Kenik, Isolating the effect of radiation-induced segregation in irradiation-assisted stress corrosion cracking of austenitic stainless steels, Journal of Nuclear Materials, 302 (2002) 20-40.

[22] J.T. Busby, M. Sowa, G.S. Was, E.P. Simonen, Post-irradiation annealing of small defect clusters, Philosophical Magazine, 85 (2005) 609-617.

[23] G.S. Was, J.T. Busby, T. Allen, E.A. Kenik, A. Jensson, S.M. Bruemmer, J. Gan, A.D. Edwards, P.M. Scott, P.L. Andreson, Emulation of neutron irradiation effects with protons: validation of principle, Journal of Nuclear Materials, 300 (2002) 198-216.

[24] Z. Jiao, G.S. Was, Impact of localized deformation on IASCC in austenitic stainless steels, Journal of Nuclear Materials, 408 (2011) 246-256.

[25] S.M. Bruemmer, E.P. Simonen, P.M. Scott, P.L. Andresen, G.S. Was, J.L. Nelson, Radiation-induced material changes and susceptibility to intergranular failure of light-water-reactor core internals, Journal of Nuclear Materials, 274 (1999) 299-314.

[26] S. Mahboubi, G.A. Botton, J.R. Kish, On the Oxidation Resistance of Alloy 800HT Exposed in Supercritical Water (SCW), Corrosion, 71 (2015) 992-1002.

[27] S. Mahboubi, G. Button, J. Kish, Oxide scales formed on austenitic Fe–Cr–Ni alloys exposed to supercritical water: role of alloying elements, in: 19th Pacific Basin Nucl. Conf., Vancouver, 2014.

[28] Y. Tsuchiya, F. Kano, N. Saito, M. Ookawa, J. Kaneda, N. Hara, Corrosion and SCC properties of fine grain stainless steel in subcritical and supercritical pure water, in: Corrosion 2007, March 11, 2007 - March 15, 2007, National Assoc. of Corrosion Engineers International, Nashville, TN, United states, 2007, pp. 074151-0741513.

[29] S.S.M. Tavares, V. Moura, V.C. da Costa, M.L.R. Ferreira, J.M. Pardal, Microstructural changes and corrosion resistance of AISI 310S steel exposed to 600-800C, Materials Characterization, 60 (2009) 573-578.

[30] J.K. Shin, H.J. Jang, K.W. Cho, C.J. Park, Effects of sigma and chi phases on the localized corrosion resistance of SR50A super austenitic stainless steel, Corrosion, 69 (2013) 364-371.

[31] A. Kriaa, N. Hamdi, H. Sidhom, Assessment of intergranular corrosion of heat treated austenitic stainless steel (AISI316L grade) by electron microscopy and electrochemical tests, Protection of Metals, 44 (2008) 506-513.

[32] S. Teysseyre, G.S. Was, Stress corrosion cracking of neutron-irradiated stainless steel in supercritical water, in: 13th International Conference on Environmental Degradation of Materials in Nuclear Power Systems 2007, April 19, 2007 - April 23, 2007, Canadian Nuclear Society, Whistler, BC, Canada, 2007, pp. 540-552.

[33] S. Teysseyre, Z. Jiao, E. West, G. Was, Effect of irradiation on stress corrosion cracking in supercritical water, Journal of Nuclear Materials, 371 (2007) 107-117.

2. Literature Review

2.1 Supercritical Water (SCW) as a Corrosive Environment

Water (H_2O) exhibits a thermodynamic critical point (22.1 MPa, 374 °C) above which it is not possible to liquefy the gas by the application of pressure [1-6]. Figure 2.1 shows the pressure-temperature phase diagram for H_2O with the typical H_2O coolant operating conditions of current generation reactors and the Canadian SCWR concept superimposed [4, 6].

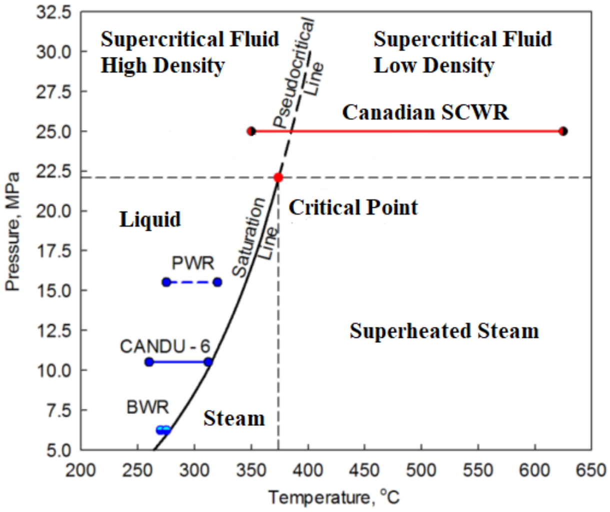

Figure 2.1 Pressure-temperature phase diagram for H_2O with the typical H_2O coolant operating conditions of current generation reactors and the Canadian SCWR concept superimposed reproduced from (reproduced from [6]).

In the supercritical region, there is no distinction between the liquid phase and gas phase; there is no phase segregation leading to liquid and vapor co-existence hence, no boiling. SCW can be either liquid-like or gas-like depending on its density, which depends on temperature [2, 4, 5]. In both cases, it has high diffusivity and good heat-transfer properties and possesses a complete solvency for most gases (at high temperature/low density) and organic compounds (at low temperature/high density) [2]. The physical properties undergo dramatic change when the temperature approaches and traverses the thermodynamic critical point [3].

From a corrosion perspective, the varied densities of SCW lead to separate and distinct oxidation mechanisms. The chemical oxidation (CO) mechanism favored in low-density/high-temperature H_2O involves direct chemical reactions between the metal surface and H_2O molecules, whereas the classical electrochemical oxidation (EO) mechanism favored in high-density/high-temperature H_2O involves separated cathodic and anodic processes on the metal surface [7]. The EO mechanism prevails in condensed (liquid phase) H_2O ($\rho > 0.06$ g/cm^3). The expected distance along the fuel channel in which the EO mechanism is expected to dominate is shown in Figure 2.2b [4]. Figure 2.2a shows the effect of temperature and pressure on the dielectric constant of H_2O [6]. The dielectric constant, which is a key parameter that provides a measure of how well a solvent is able to dissolve ionic substances, exhibits a sharp drop at the pseudo-critical point. The varied dielectric constant is expected to affect oxide solubility as the critical point is traversed , as shown in Figure 2.2b [4]. All oxides considered show a drastic decrease in their predicted solubility when the temperature increases above the critical point. After reaching a minimum value, the predicted solubility of Cr_2O_3 and Fe_3O_4, expected corrosion products of stainless steel exposed in SCW, tends to increase slowly [4].

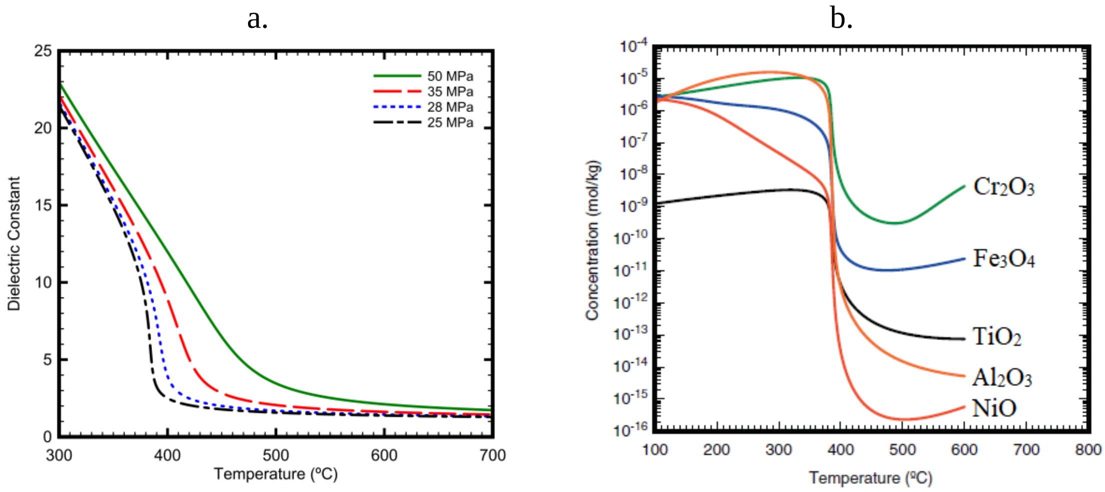

Figure 2.2 (a): Dielectric constant of H_2O as a function of temperature and pressure reproduced from (reproduced from [4]); (b): Predicted oxide solubility in H_2O as a function of temperature at 25 MPa reproduced from (reproduced from [4]).

2.2 General Corrosion of Austenitic Stainless Steels in SCW

2.2.1 Corrosion Kinetics

The corrosion kinetics of austenitic stainless steels is typically extracted from weight change data. It is well known that the corrosion/oxidation rates are thermally activated and the temperature dependence can be described by an Arrhenius behavior. Thus, Chen et al. [8] evaluated the SCW corrosion kinetics by fitting the weight gain data with the following empirical model:

$$\Delta W = Ae^{(Q/kT)}t^n = A't^n \tag{2.1}$$

Where ΔW is the weight change (mg/dm^2), A is a constant, Q is activation energy (kJ/mol), k is the Boltzmann constant (1.38×10^{-23} J/K), T is temperature (K), t is exposure time (h) and n is the time exponent. The time exponent (n) is dependent on the dissolved oxygen content. The fitting model is based on the assumption that there is no weight loss during exposure to SCW. As described in some details later, austenitic stainless steels are prone to oxide scale spallation during exposure in SCW. Thus, the activation energy calculated in this fashion is likely an approximate value. In terms of a rate law, corrosion tends to follow parabolic ($n\approx2$) kinetics for pure deaerated SCW, while it follows linear ($n\approx1$) kinetics for SCW with a certain concentration of oxygen [8]. Figure 2.3 shows a typical example of the corrosion kinetics, showing the weight gain of alloy D9 (Fe-14Cr-16Ni-1.6Mo) in 25 MPa SCW as a function of both temperature (Figure 2.3a) and dissolved oxygen (Figure 2.3b). The oxidation kinetics of austenite stainless steel in SCW tends to be parabolic but the data are scattered [9, 10]. Scattered weight change data were attributed to oxide spallation during SCW oxidation [8, 10]. The possible reason for oxide spallation was attributed to high expansion coefficient of austenitic steels, formation voids within oxide layers and lattice parameter mismatches [8, 11].

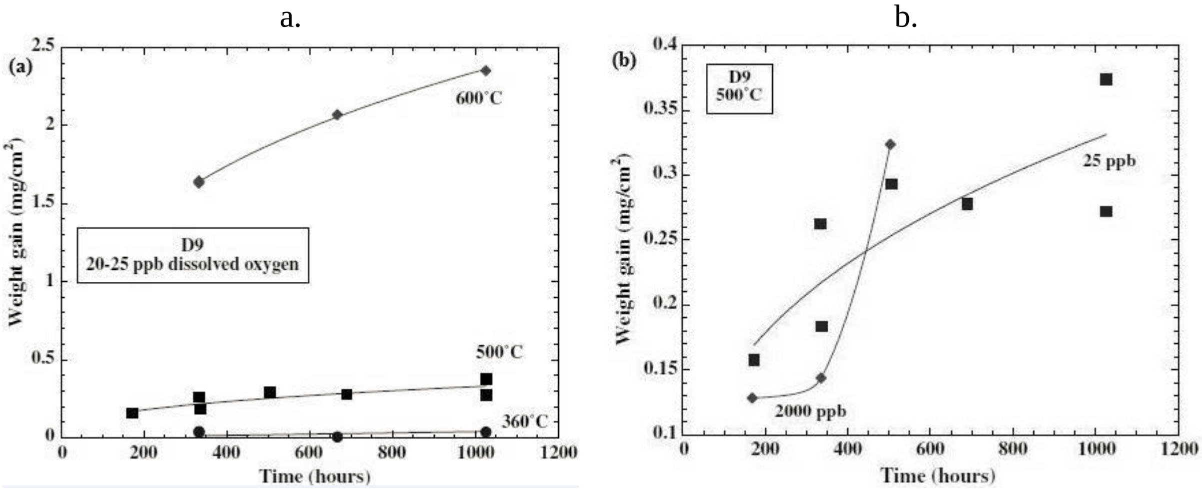

Figure 2.3 Weight gain of alloy D9 as a function of (a) time and temperature, (b) time and dissolved oxygen in a flow loop autoclave testing facility in 25 MPa SCW (reproduced from [9]).

A simple relationship between oxide thickness and weight change is typically not evident for many austenitic stainless steels exposed in SCW because of the tendency of oxide scale spallation. Guzonas and Cook [4] proposed using an overall mass balance to account for oxide scale spallation. This method involves estimating the mass of Fe, Ni, Cr and other elements in the oxide scale using surface analysis (oxide scale chemistry) in combination with oxide weight measurements, the latter of which is compared with the weight loss of the test coupon measured after descaling. Figure 2.4 shows an example of the mass balance approach applied to Type 304 stainless steel (Fe-18Cr-8Ni) exposed in flowing 25 MPa SCW at 500 °C with a low concentration of dissolved oxygen [4]. several key points are evident: (i) after-exposure weight gain significantly underestimates the actual corrosion of the alloy (taken here as a positive value) by a factor of 5 to 6, (ii) metal contained in the oxide scale is not sufficient to account for the total corrosion weight loss, indicating that some portion of the oxide scale was released to the SCW environment (iii) actual corrosion rate of the alloy decreases with time as expected despite the after-exposure weight gain exhibiting a relatively constant value [4].

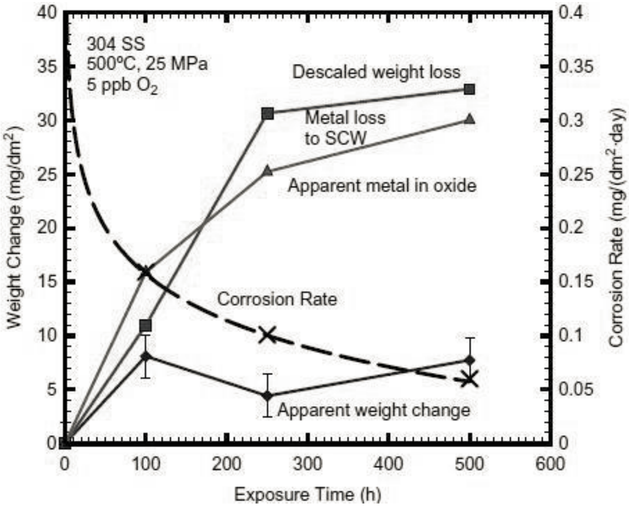

Figure 2.4 Mass balance for Type 304 stainless steel corrosion in flowing 25 MPa SCW at 500 °C (reproduced from [4]).

As discussed above, the overall weight gain data is the combination of oxide scale formation and oxide scale release (removal) as shown in Figure 2.5 [4]. Oxide scale formation originates from the inward diffusion of oxygen during high temperature exposure in SCW [12, 13]. Oxide scale release into the solution can occur by either oxide scale spallation (mechanical) [8, 9] or dissolution (chemical) [4]. Alloys with Cr content above 20 wt.% tend to form corundum type (M_2O_3) oxide during high temperature oxidation [14, 15] that are known to provide better corrosion resistance

[16]. However, Cr_2O_3 scales are known to volatilize during high temperature oxidation in presence of H_2O and O_2 [15]. Mahboubi et al. showed evidence in support of volatilization of Cr_2O_3-based scales in flowing oxygenated (8 ppm dissolved oxygen) SCW at just 550 °C [17]. Thus, the actual oxidation kinetics in SCW should be calculated using descaled weight loss data, rather than the post oxidation weight gain, and with appropriate consideration given to the likely oxide scale release mechanism.

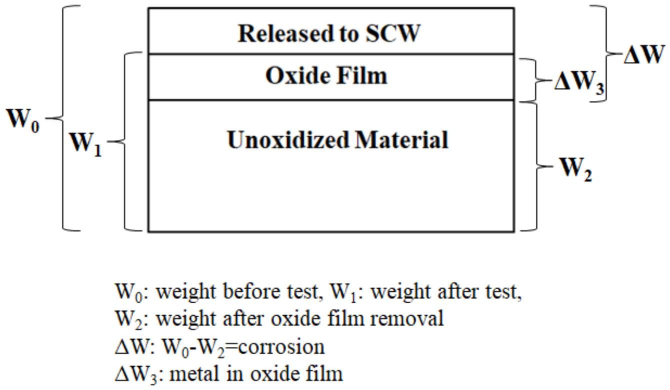

Figure 2.5 Corrosion rate evaluation method to account for the key processes taken place during corrosion in SCW (reproduced from [18]).

Several studies have been done to evaluate the corrosion of austenitic stainless steels in SCW and the main factors affecting it [4, 5]. Corrosion testing in support of SCWR development has been performed at temperatures ranging from below the critical temperature up to 650 °C. The water chemistry has typically been low conductivity "pure" water with nominal dissolved oxygen concentrations ranging from <10 ppb to 8 ppm. Test coupons have been examined after SCW exposures ranging from 24 h to 3000 h in both static autoclaves and flow loop autoclaves. Based on the test results, the overall ranking of the relative contributions of the various factors that contribute to corrosion in SCW, from the highest to the lowest importance are [5]:

Temperature ≈ Surface Finish > Water Chemistry > Density

It has been reported that the major factor affecting the reproducibility of corrosion testing in SCW is the sample preparation method (e.g., abrasion and polishing) [4, 5, 8, 10]. The effect of cold working associated with mechanical abrasion and/or polishing has long been known to improve the corrosion resistance of stainless steels in SCW environments [4, 5, 8, 10]. This is believed to result from the rapid build-up of a protective Cr-rich oxide during high temperature oxidation from enhanced Cr diffusion to the alloy surface via the multiple diffusion pathways created by local deformation [19]. It is noted that the systematic weight change analysis from the literature is difficult to interpret as the experimental parameters (temperatures, pressure, surface finish and water chemistry) are all varied [4]. Thus, the discussion of significance of each factor needs to be restricted to individual tests [20].

Temperature is the most critical factor as corrosion in SCW (above 400 ºC) follows solid state diffusion process [8, 12]. Increasing temperature can increase oxidation rate exponentially [12]. Besides, temperatures within the range from 500 ºC to 900 ºC have been reported to induce internal-external transition (including grain boundary oxidation) on austenitic stainless steels during steam oxidation [21]. Due to the similarity between steam oxidation and SCW oxidation [7, 22], austenitic stainless steels may also experience preferential grain boundary oxidation causing enhanced IGSCC susceptibility. Another problem associated with increased temperature is volatilization/dissolution of the protective oxide scale [11, 15, 23-26]. Oxide scales formed on austenitic stainless steels were reported volatile in moisture air/oxygen and oxygenated steam by forming volatile species such as $CrO_2(OH)_2$ during higher temperature oxidation [11, 15, 24-26]. Mahboubi et al. reported continuous weight loss kinetics of high Cr Alloy 33 (Fe-33Cr-32Ni), whereas weight gain of Type 310S (Fe-24Cr-20Ni) continuously increase in flowing 25 MPa SCW at 550 ºC [23].

As a typical example of corrosion kinetics and some factors that affect it. Figure 2.6 shows the weight gain of Type 316 (Fe-16Cr-10Ni-2Mo) as a function of dissolved oxygen and time in 500 °C 25 MPa flow loop SCW. Type 316 (Fe-16Cr-10Ni-2Mo) initially exhibited lower weight gain when exposed in SCW with high dissolved oxygen. At longer times, however, the weight gain increased significantly. The weight change method has limitations because of possible spallation of the oxide scale formed on the alloy surface during exposure. For example, the weight gain of Type 316 (Fe-16Cr-10Ni-2Mo) exposed at 500 °C 25 MPa flow loop SCW reaches a maximum value after 500 h exposure, after which it almost remain constant due to oxide scale growth and oxide scale spallation, as shown in Figure 2.6a. A higher concentration of dissolved oxygen accentuated oxide spallation on Type 316

(Fe-16Cr-10Ni-2Mo) as shown in Figure 2.6b. Thus, weight gain measurements can show a cumulative effect (weight gain due to oxide scale formation counterbalanced by weight loss due to oxide scale spallation and must be interpreted with appropriate care [10]. Their results show that immersion in high dissolved oxygen containing SCW results in a greater corrosion in almost all cases, but corrosion is lower at intermediate levels of dissolved oxygen (25-110 ppb) than compared to fully deaerated (< 10 ppb) SCW [9]. Due to the complexity of this weight-change data, the role dissolved oxygen plays in SCW corrosion still needs further research.

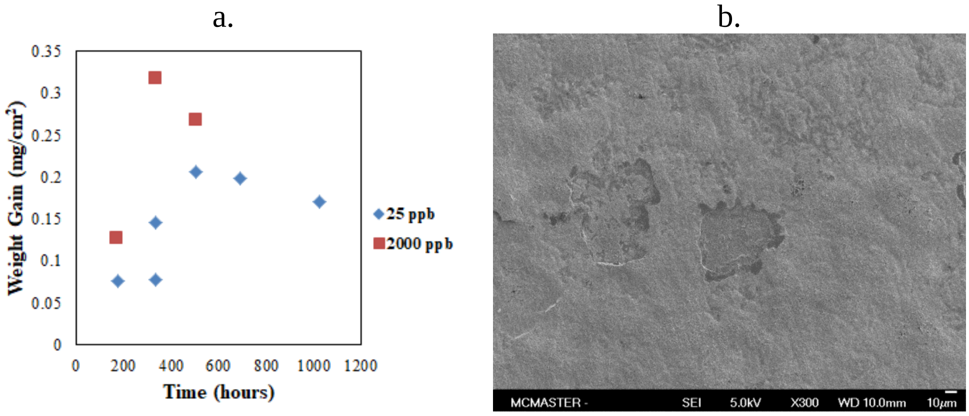

Figure 2.6 (a) Weight gain as a function of time for Type 316 exposed in a flow loop autoclave testing facility in 25 MPa SCW at 500 °C (reproduced from [9]); (b) SEM image showing the oxide scale morphology of Type 316 (Fe-16Cr-10Ni-2Mo) sample after exposure in a flow loop autoclave testing facility 25 MPa SCW at 550 °C.

2.2.2 Oxide Scale Formation

Most austenitic stainless steel oxide scales formed in SCW show a two- or three-layer structure dependent upon the exposure temperature and SCW chemistry including the dissolved oxygen content [13, 27, 28]. The inner layer, usually comprised of Fe-Cr spinel ($FeCr_2O_4$) and/or corundum (Cr_2O_3), tends to be more compact and offers improved corrosion protection relative to the outer layer [4, 5, 13, 14, 27, 28]. The outer layer, rich in Fe and more porous, is usually comprised of either magnetite (Fe_3O_4) or hematite (Fe_2O_3) depending on the temperature, pressure and dissolved oxygen content of the SCW [12, 13, 28]. The outer layer also may divide into two sub-layers including a magnetite-rich inner layer and a hematite-rich outer layer [13, 28]. An SEM image showing the typical cross-sectional appearance of the dual oxide scale formed on austenitic stainless steel (Type 316L in this case) is shown in Figure 2.7. The inner layer is Cr-rich Fe-Cr spinel ($FeCr_2O_4$) and the outer layer is porous magnetite (Fe_3O_4) [29]. Increasing Cr content inducing more protective inner layer by forming more compact spinel ($FeCr_2O_4$) or corundum (Cr_2O_3) [11, 15].

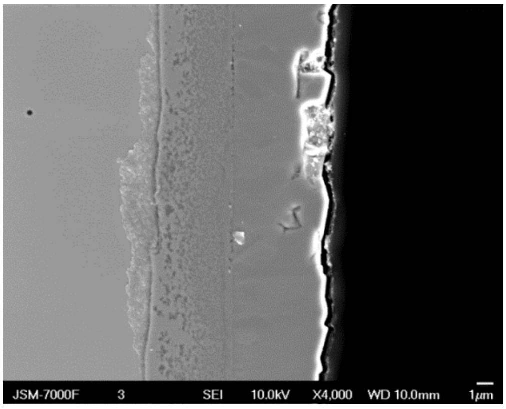

Figure 2.7 Cross-section of the oxide formed on Type 316L exposed in static autoclave to SCW 550 °C with 8 ppm dissolved oxygen concentration for 500 h.

Due to the similarity between high temperature (low pressure) steam oxidation and SCW corrosion [4, 7, 22], previous oxidation models [30-33] applicable for high temperature water corrosion have been applied to explain the corrosion in SCW [4, 12, 28, 34-36]. Was et al. [12] proposed that the corrosion mechanism of austenitic stainless steels in SCW can be adequately explained by the Robertson model [32], as shown in Figure 2.8: the outer layer, consisting of magnetite, is formed by outward diffusion of Fe and grows with the same crystallographic orientation as the inner layer. The inner layer (spinel/corundum) grows with the same crystallographic orientation as the substrate. As Cr and Ni diffuse slower than Fe in the metal, they are left behind when Fe diffuses outward. The inner layer likely grows from oxidation of the metal due to inward diffusion of oxygen. Thus, the rate-controlling diffusion process controls the corrosion rate of austenitic stainless steels in SCW.

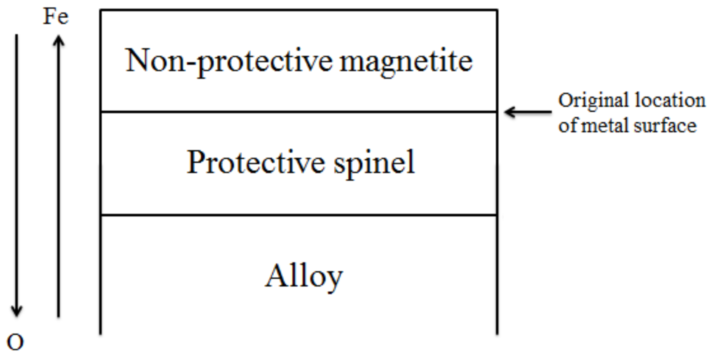

Figure 2.8 Schematic illustration of the corrosion mechanism for austenitic stainless steels exposed to SCW (reproduced from [12]).

Was et al. proposed a possible rate-controlling diffusion process that was strongly influenced by the oxide structure [12]. The outer layer formed on Type 316L stainless steel is dense and grows with the same orientation as the inner layer and the underlying metal. The outer layer formed on Type 304 stainless steel, albeit more porous, also grows with the same orientation as the inner layer and the underlying metal. The observation that Type 304 stainless steel has a more porous outer layer (less protective), yet exhibits a lower corrosion rate than Type 316L in SCW indicates the outer layer is not the protective layer, nor is it the limiting factor controlling the process. This implies that both inward diffusion of oxygen and outward diffusion of the alloying elements through the inner layer actually control corrosion [12]. However, the biggest criticism of Was et al.'s proposed mechanism is that the thickness of the oxide layer was not considered. The inward diffusion of oxygen could either be volume diffusion or grain boundary diffusion in the magnetite outer layer. Volume diffusion of oxygen in magnetite is too slow to account for the measured corrosion rate [12]. Grain boundary diffusion of oxygen is more consistent with the measured corrosion rate (and oxide scale thickness), but the typical activation energy associated with grain boundary diffusion (167 kJ/mol [37]) is much lower than the experimentally-determined activated energy (264 kJ/mol [37]). Thus, Was et al. [12] proposed that diffusion of oxygen along grain boundaries or by some other short-circuit path is required to explain the measured weight gains and oxide scale thickness. Was et al.'s calculation did not consider any oxide scale spallation or dissolution to help account for this discrepancy.

From Table 1.1, Type 310S stainless steel is reported to exhibit acceptable corrosion resistance in SCW environments [5, 20, 38-40]. Based on published work, the corrosion rate (weight change) of Type 310S stainless steel in SCW could be expressed by [39]:

$$\Delta W = (0.031T - 22.4) + 2.71 \bullet t \bullet \exp(-\frac{46500}{RT}) \quad (2.2)$$

where ΔW is the weight gain in mg/dm^2, T is the absolute temperature in K, t is the exposure time in h and R is gas constant (8.314 J/mol/K). The predicted weight gain of Type 310S in SCW at temperature range 400-800 ºC is shown in Figure 2.9. The maximum weight gain (weight gain at 800 ºC for 3.5 years) is approximately 454 mg/dm^2, corresponding to 15 μm penetration (corrosion penetration=0.033ΔW [39]). And the maximum allowed penetration is 200 μm [38]. So Type 310S stainless steel can meet the requirement for general corrosion in the Canadian-SCWR design concept.

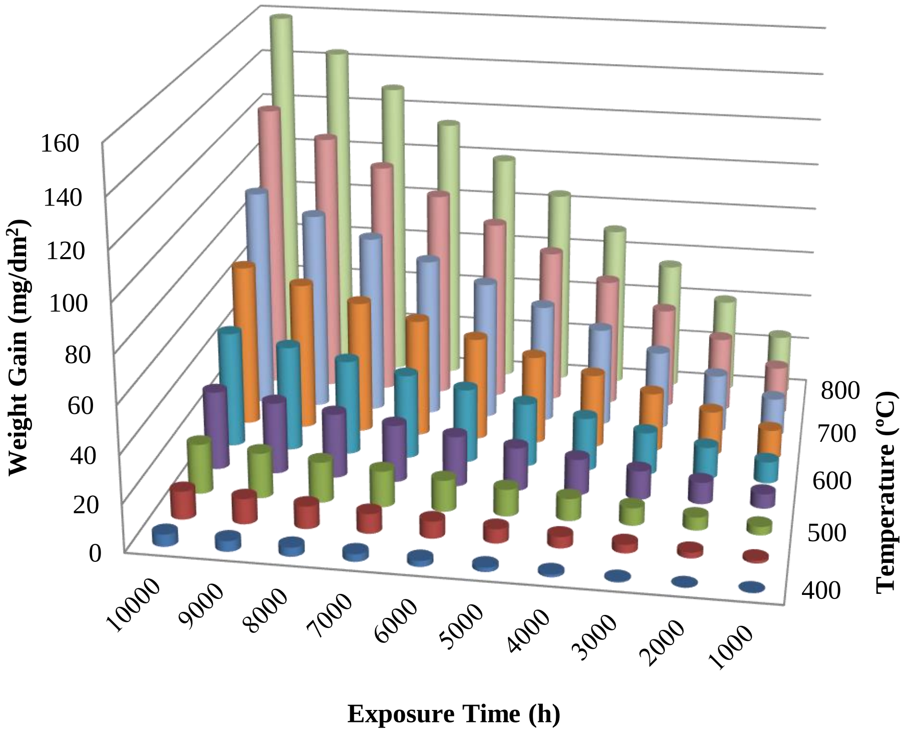

Figure 2.9 Predicted weight gain of Type 310S stainless steel in SCW based on equation 2.2.

2.3 SCC of Austenitic Stainless Steels in SCW

Fundamentally, the occurrence of SCC in general depends on the simultaneous achievement of three conditions: 1) susceptible material, 2) environment that causes SCC and 3) tensile stress. A reactor core in general has an extreme environment consisting of high temperature pressurized water, imposed stress and strain, radiation fields and corrosive environment as shown in Figure 2.10. The SCC mode experienced in current generation LWRs is predominantly intergranular [41, 42]. In a SCWR concept, on the other hand, electrochemistry in the SCW water coolant is expected to be absence above 500 °C [4-7, 22]. Nevertheless, investigations of IGSCC susceptibility of austenitic stainless steel in SCW have been normally conducted by raising intergranular SCC temperature from subcritical to supercritical [18, 43-47] and then interpreting the results using the existing knowledge base derived research and engineering experience with current LWRs [48-52]. Thus, a review of the SCC susceptibility of austenitic stainless steels in current generation LWR environments is present next, followed by a review of the SCC susceptibility in SCW environments.

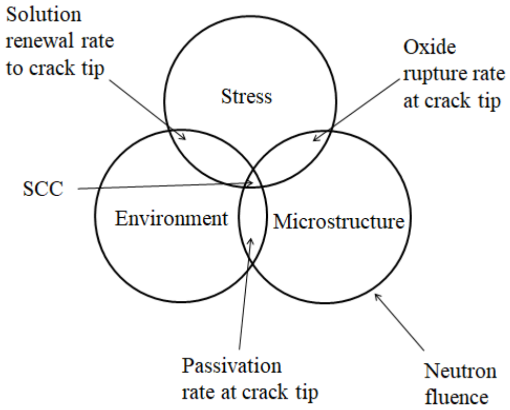

Figure 2.10 Schematic of the primary engineering parameters that effect SCC (reproduced from [41]).

2.3.1 SCC of Austenitic Stainless Steels in LWR Environments

A brief summary of intergranular SCC and intergranular IASCC mechanisms are shown in Table 2.1. A significant research effort has been devoted to better understand the intergranular SCC of austenite stainless steels exposed simulated hot water LWR environments [41, 42, 53-61] with or without irradiation. The onset of intergranular SCC in LWR environments have been attributed to radiolysis, formation of Cr depleted zones adjacent to grain boundaries, segregation of minor alloying elements at grain boundaries, hardening , localized deformation and formation of voids on grain boundaries [28, 41, 62, 63].

Table 2.1 Summary of intergranular SCC/intergranular IASCC mechanisms in LWR environments.

SCC mechanisms	Key factor	References
Slip oxidation mechanism	Corrosion potential and ion transportation	[64]
Grain boundary Cr depletion (arising from RIS)	Minimum Cr content and Cr depletion width	[65]
Irradiation hardening	Hardness increase induced by irradiation	[66]
Localized deformation	Stacking fault energy	[57]
Grain boundary voids nucleation	Creep	[63]

A schematic of the slip oxidation model (also known as Ford-Andresen model) is shown in Figure 2.11. This model assume failure due to SCC exhibit IG cracking, and oxide film on the crack front is ruptured by dislocation movement at crack tip, which exposes bare metal the crack tip to the corrosive environment. The pure metal exposed to corrosive environment can dissolve to solutions by dealloying [41]. With subsequent oxidation reforming the oxide film again (repassivation), and the slip oxidation process repeats [41, 64]. Water radiolysis has long been known to change the corrosion potential in a manner that is more amenable to support IASCC by affecting rate of metal ions dissolve to corrosive solutions and oxide file repassivation [42, 64, 67].

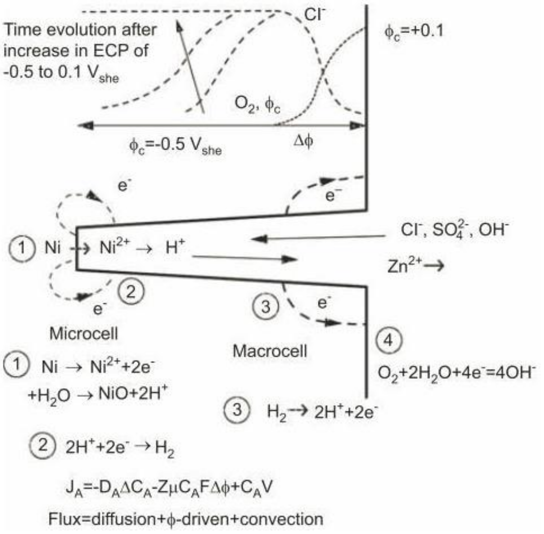

Figure 2.11 Schematic of crack chemistry transport processes in high temperature water with O_2 (reproduced from [41]).

The Cr depletion and hardening are the primary two radiation damage effects that account for IASCC [42, 48, 55, 64, 67-69]. Similar to thermally-induced sensitization for creating a Cr depleted zone adjacent to grain boundaries, Cr depleted zone are believed to preferentially dissolved to oxidizing environments inducing onset of IASCC in LWR environments [65, 68]. Large amount of research shows an increased intergranular SCC susceptibility with grain boundary Cr depletion in both laboratory and plant operational experience [28, 34, 41, 42, 62, 67, 70]. Similar to the Cr depletion theory segregation of minor alloy elements has also been proposed as a key factor affecting intergranular SCC susceptibility causing the preferential dissolution of grain boundaries. Undersize solutes (such as Si and P) tend to enriched along the grain boundaries under radiation flux [55, 68]. Moreover, Si enrichment along the grain boundaries can form SiO_2, which tend to dissolve in hot water given the relatively high solubility [41, 62]. The role played by RIS in the intergranular IASCC process is illustrated in Figure 2.12. Due to the Cr depletion, the oxide film formed on grain boundary exhibited less protectivity compared with that formed on grains. The porous grain boundary oxide can easily ruptured by external stress inducing crack initiation/propagation.

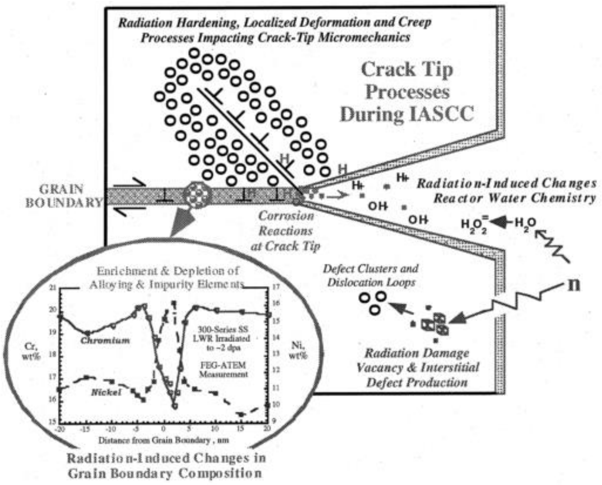

Figure 2.12 Schematic illustrating mechanistic issues believed to influence crack propagation during IASCC of austenitic stainless steels (reproduced from [68]).

Radiation induced defects (point defects, voids/vacancies), dislocation loops and intermetallic precipitates can act as pinning pints and obstacles for dislocation movements, result in radiation hardening and embrittlement [53-55, 71-74]. The yield strength (YS) and ultimate tensile strength (UTS) increase correspondingly and ductility and work hardening rate decrease at relatively low doses [72, 73]. Busby et al. correlated change in YS and change in hardness to be:

$$\Delta\sigma_y = 3.03\ \Delta Hy \tag{2.3}$$

where $\Delta\sigma_y$ is increase in YS expressed in MPa and ΔH_y is increase in hardness expressed in kg/mm^2 [54]. The source for the increased YS and hardness could be either cold working or radiation induced hardening. Similar to thermally-induced sensitization (Cr depleted zone formation) and RIS, cold working and radiation induced hardening exhibited increased SCC susceptibility [41, 53, 60, 69, 75]. Cold working have been vastly applied to simulate radiation induced damage when investigating SCC properties [41, 53, 60, 69, 75]. Hash et al. shown that cold working induced hardening typically coincides with TGSCC, whereas radiation induced hardening coincides with intergranular SCC [53]. This suggests hardening alone is necessary, but not sufficient to promote IASCC.

Busby et al. investigated the contribution of Cr depletion and hardening caused by radiation damage to IASCC by isolating Cr depletion using post radiation annealing [55]. Interestingly, neither Cr depletion nor hardening was found to control the occurrence of IASCC alone despite their good correlation to IASCC susceptibility [55]. The occurrence of IASCC has been attributed to radiation induced microstructure [76]. During external straining of irradiated materials dislocations move along a given slip plane, the dislocation movement could clear majority of barrier defects, and subsequent dislocation movement primarily occurs in these channels, resulting in localized deformation [41, 53, 56-58, 77]. Types of interactions between dislocation channels and grain boundaries are shown in Figure 2.13. Was and coworkers [50, 53, 56-58, 65, 68] have devoted a large amount of effort investigating IASCC in LWR and SCWR environments and they report that the straining at intersection between dislocation channels and grain boundaries could be as large as 100% even though the bulk straining only few percent. The stress introduced by such a huge straining may rupture oxide on the surface causing crack initiation. Dislocation channeling has also been reported in irradiated stainless steels without the need of any mechanical straining [78, 79].

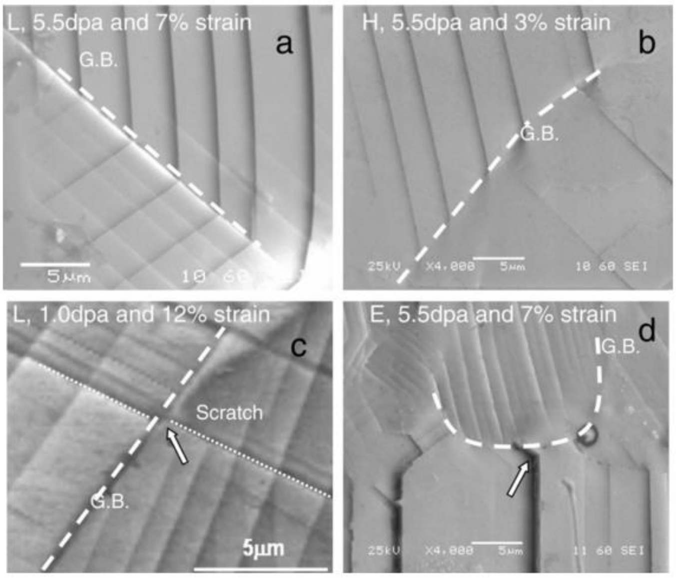

Figure 2.13 Types of interactions between dislocation channels and grain boundaries: (a) slip transmission from one grain to another, (b) slip termination at a grain boundary, (c) grain boundary sliding and (d) deformation ledge formation at a grain boundary [56].

Arioka and co-workers suggests a strong similarity between SCC and creep (up to 550 ºC) [59-61, 63, 75, 80-83]. They propose stress induce aggregation of vacancies to produce cavities, which weakening grain boundaries and induce initiation and propagation of cracks [59-61, 63, 75, 80-83]. The biggest problem with the testing conducted by Arioka and co-workers (both SCC and creep tests) is that the tests were conducted using compact tension (CT) tests with very high stress intensity (normally above 30 MPa·$m^{1/2}$). Stress intensity may increase rapidly during crack propagate in CT tests and crack growth rates can be more than two orders of magnitude higher than those under constant stress intensity conditions [70, 84]. This potentially may explain why Arioka and co-workers reported trivial effects of corrosive environments in their work. Despite the relatively high stress intensity used in the Arioka et al. work, creep is still recognized as a major factor that contributes to intergranular cracking during SCC testing in high temperature water environments [41, 50, 59, 61]. An equicohesive temperature (ECT) exists at which the matrix and grain boundaries have equal strength [85]. The grain boundaries are stronger than matrix below the ECT and weaker than the matrix above the ECT. The ECT is known to decrease with strain rate [85] due to occurrence of grain boundary sliding [86]. At high stresses and intermediate temperatures, fracture often occurs in the form of wedge cracks due to inability to accommodate grain boundary sliding driven by shear stresses [85-87]. Grain boundary voids/cavity nucleation, growth and coalescence become the dominant mode for intergranular creep fracture at high temperature and low stress range [85, 86]. Grain boundary voids/cavity nucleation tend to initiated along grain boundaries aligned for maximum shear [85] and tend to be accelerated by nanometer scale secondary phases/precipitate at grain boundaries [88, 89] due to dislocation pile up.

2.3.2 SCC of Austenitic Stainless Steels in SCW Environments

As it referred above, investigations of IGSCC susceptibility of austenitic stainless steel in SCW have been normally conducted by raising intergranular SCC temperature from subcritical to supercritical [18, 43-47] and then interpreting the results using the existing knowledge base derived research and engineering experience with current LWRs [48-52]. But there are some debate in data interpreting as there is no operational SCWRs to give SCC instructions. Tsuchiya et al. [45] and Fujisawa et al. [43] have used the percent intergranular crack (%IG) found on the fracture surface as a specific measure of intergranular SCC susceptibility, whereas Was et al. [13, 50] have used both crack depth and density found on the gage surface as a measure of general SCC susceptibility. Unfortunately, these measurements are not always in agreement [13]. This is likely because %IG metric falls to zero if there is no obvious crack growth on the fracture surface and the crack density metric is more sensitive to small cracks, which may serve to better capture crack initiation. Teysseyre and Was [50] reported that the SCC severity of solution annealed Type 304 and Type 316L in deaerated SCW is highly temperature-dependent. The crack growth (measured by crack depth/time) increased nonlinearly with temperature and the dependence could be described by Arrhenius behavior. Tsuchiya et al. [45] noted that the SCC susceptibility, measured as %IG on the fracture surface of sensitized (formation of Cr-depleted zones adjacent to grain boundaries induced by thermal ageing as a pre-treatment) Type 304 in SCW with 8 ppm dissolved oxygen, dropped from 100% at 290 °C to 0% above 400 °C. This suggests the effects of sensitization (thermally-induced formation of Cr depleted zones adjacent to grain boundaries) on intergranular SCC decreases with increasing temperature as a result of a decreased tendency for electrochemistry to control the process. But the crack density shows a significant increase as the temperature is increased to 550 °C. These observations show that the %IG metric is insufficient to characterize the full extent of SCC in SCW. Consequently, it was suggested both measurements of intergranular SCC propensity (%IG on the fracture surface and crack density on the gage surface) should be considered when discussing intergranular SCC susceptibility in SCW environments [10].

The intergranular SCC susceptibility of pre-irradiated austenitic stainless steels in SCW has been shown to be affected by factors similar to those affected intergranular SCC in hot water environments simulating LWR environments [48, 49, 51]: IASCC cracking correlate with both increased hardening and decreased grain boundary Cr content. However, both Cr depletion and hardening are unlikely solely control onset of intergranular SCC in SCW environments as well. Solution annealed Type 316L (Fe-16Cr-10Ni-2Mo), alloy 625 (Ni-22Cr-9Mo) and alloy 690 (Ni-29Cr-10Fe) exhibited intergranular SCC cracks over the temperature range from 400 ºC to 550 ºC [50]. Occurrence of intergranular SCC on solution annealed microstructure that free of cold working/radiation induced hardening with uniformly distributed alloying elements suggests that the influence of Cr depletion and/or hardening are even less profound in SCW. Besides, radiation-induced hardening is more serious at 400 ºC, whereas cracking is more serious at 500 ºC for Type 316L and alloy 690 [48]. Alloy 690 exhibited severe intergranular SCC cracks with 24 wt.% Cr at grain boundary in 400 ºC SCW [48]. All these results suggest even combined effect of Cr depletion and radiation-induced hardening cannot account for occurrence of intergranular SCC of austenitic stainless steels in SCW. An alternative root cause such as localized deformation or void formation is likely necessary to explain intergranular SCC susceptibility in SCW regime. Even through intergranular SCC susceptibility was reported to increase with radiation dose [48, 49, 51], it is more likely radiation induced microstructure (interstitials, voids, vacancies) accentuated strain localization and/or void formation. Another mechanism relevant to intergranular SCC in SCW is environmental assisted creep [50, 52, 59, 61]. Arioka and coworkers investigated a serious Type 316 steels (including cold worked, solution annealed and sensitized) and observed intergranular cracking at temperatures of 500-550 ºC [61]. They attributed the intergranular cracking to grain boundary sliding and proposed the activation energy of creep behavior in 380-500 ºC is about 100 kJ/mol [61], which is consistent with the activation energy of 304 (105 kJ/mol) and 316L (85 kJ/mol) in 400-550 ºC SCW measured by Teysseyre and Was [50]. It should be noted that Teysseyre and Was [50] observed creep cracking of 304 in 500 ºC argon environment and much higher intergranular cracking propensity in SCW environments. Zhang et al. [52] reported similar crack growth rate of alloy 690 during creep and SCW SCC tests at temperature range 400-550 ºC. All these findings suggest environmental assisted creep played an important role in intergranular SCC of austenitic steels in SCW environments.

The SCC susceptibility of candidate fuel cladding materials in SCW is expected to be affected by many factors including mechanical loading conditions (such as strain rate), alloy composition, microstructure (including surface finish, cold work and instability induced from prolonged exposure to both high temperature and radiation), and SCW chemistry. A number of candidate SCWR alloys have been evaluated for SCC susceptibility in SCW, primarily in the mill-annealed condition and without and pre-treatments (cold-working, thermal ageing of irradiation damage) Austenitic stainless steels such as Type 304, Type 316/316L, Type 347 (Fe-18Cr-11Ni) and alloy 625 (Ni-23Cr-10Mo-5Fe) have been found to experience some degree of SCC, with the majority of SCC being intergranular in nature [13, 40, 50, 90, 91].

Strain rate is a critically important factor in the SCC evaluation of alloys in SCW. When the strain is applied at a higher rate than a critical value, protective film formation is not fast enough to repair rupture film caused by mechanical straining, and the test sample fails by ductile rupture [50, 90, 91]. If the strain rate is below the critical value, protective film formation is too fast at repairing the ruptured film, and thus the cracking is reduced or avoided in SCW environments [91]. This is the reason why some alloys do not exhibit SCC under static loading, whereas cracks readily form in identical environments when tested in a dynamic loading test using the constant strain rate approach: constant extension rate tensile (CERT) testing or slow strain rate tensile (SSRT) testing.

Different types of austenitic stainless steels have shown distinctly different SCC modes. For example, Type 304 stainless steel exhibits an intergranular SCC (intergranular SCC) susceptibility, whereas Type 316L stainless steel exhibits a mixed-mode SCC susceptibility (both transgranular SCC (TGSCC) and intergranular SCC) when exposed in SCW [50]. It has also been shown that a transition from intergranular SCC to transgranular SCC is possible during the SCC testing of austenitic stainless steel in SCW [91]. The SCC test conditions for various alloys are summarized in Table 2.2. Intergranular SCC susceptibility tend to increase with temperature, radiation damage, oxygen content, decreasing strain rate, increasing stress intensity. Almost all austenitic stainless steels exhibited a certain degree of cracking during SCC tests in SCW environments. This research is focusing on investigating the primary factor controlling the occurrence of intergranular SCC in Canadian-SCWR environments. The possible cracking mechanism of Type 310S stainless steel in SCW was proposed to help better predict and control intergranular SCC susceptibility and improve material performance.

Table 2.2 Summary of SCC tests surveyed in the open literature.

alloy	temperature (°C)	pressure (MPa)	dissolve oxygen	test method	strain rate/stress intensity	crack mode	reference
690	450, 550	25	10 ppb	CT	25 MPa√m	IG	[52]
310S	500	25		capsule		IG	[92]
316,625,C276,Ni-45Cr-1Mo	400	25	8 ppm	SSRT	2.8 x 10^{-6} s^{-1}	mix	[43]
HCM12,304,316L,310S,H2,T6F,600,625,690,Ti-15Mo-5Zr-3Al	290 - 550	25	8 ppm	SSRT	4 x 10^{-7} s^{-1}	IG	[93]
316L,304L,310S	290 - 550	25	8 ppm	SSRT	4 x 10^{-7} s^{-1}	IG	[18]
304, 316L	290 - 550	25	8 ppm	SSRT	4 x 10^{-7} s^{-1}	IG	[45]
304, 316L, 600	290 - 550	25	8 ppm	SSRT	4 x 10^{-7} s^{-1}	IG	[46]
316	360, 400	25,60	8 ppm	SSRT	2.8 x 10^{-6} s^{-1}	IG	[47]
316L	550	25	5-900 ppb	SSRT	1-6.7 x 10^{-7} s^{-1}	mix	[91]
316L,304,625,690	400, 500, 550	25	10 ppb	CERT	3 x 10^{-7} s^{-1}	mix	[50]
304L,316L,625,690	500	25	10 ppb 8ppm	CERT	3 x 10^{-7} s^{-1}	IG	[94]
316L,690	400, 500	25	10 ppb	CERT	3 x 10^{-7} s^{-1}	IG	[49]
316	400, 500	24, 27.6	10 ppb	CERT	3 x 10^{-7} s^{-1}	IG	[51]
316	288-500	25	10 ppb, 2 ppm	CT	25.3-27.5 MPa√m	mix	[95]
T91, HCM12A,HT9	400-600	25	100, 300 ppb	CERT	3 x 10^{-7} s^{-1}	IG	[96]
316L,D9,690,800H	400, 500	24	10 ppb	CERT	3 x 10^{-7} s^{-1}	IG	[48]
15Cr-4Al-2W	500	25	8 ppm	SSRT	1 x 10^{-3} s^{-1} 1 x 10^{-6} s^{-1} 5 x 10^{-7} s^{-1}	No SCC	[97]
F82H	290-550	23.5	200 ppb	SSRT	3.3 x 10^{-7} s^{-1}	No SCC	[44]

2.4 References:

[1] D. Guzonas, Materials and chemistry for a supercritical water-cooled reactor–progress and challenges, in: Proc. 5th Int. Sym. SCWR (ISSCWR-5), Vancouver, British Columbia, Canada, 2011.

[2] P. Kritzer, Corrosion in high-temperature and supercritical water and aqueous solutions: a review, The Journal of Supercritical Fluids, 29 (2004) 1-29.

[3] W.G. Cook, R.P. Olive, Prediction of crud deposition in a CANDU-SCWR core through corrosion product solubility and transport modelling, in: The 5th Int. Sym. SCWR (ISSCWR-5), Vancouver, British Columbia, Canada, 2011.

[4] D.A. Guzonas, W.G. Cook, Cycle chemistry and its effect on materials in a supercritical water-cooled reactor: a synthesis of current understanding, Corrosion Science, 65 (2012) 48-66.

[5] D. Guzonas, R. Novotny, Supercritical water-cooled reactor materials – Summary of research and open issues, Progress in Nuclear Energy, 77 (2014) 361-372.

[6] H. Thind, S. Gupta, I. Pioro, G. Harvel, Heat-transfer analysis of SCW to SCW double-pipe heat exchanger for indirect-cycle SCW NPPS, in: Proceedings of the 5th Int. Sym. SCWR (ISSCWR-5）, Vancouver, British Columbia, Canada, 2011, pp. 84.

[7] X. Guan, D.D. Macdonald, Determination of corrosion mechanisms and estimation of electrochemical kinetics of metal corrosion in high subcritical and supercritical aqueous systems, Corrosion, 65 (2009) 376-387.

[8] Y. Chen, K. Sridharan, T. Allen, Corrosion behavior of NF616 and D9 as candidate alloys for supercritical water reactors, in: Corrosion 2005, NACE International, 2005.

[9] G. Was, T. Allen, Time, temperature, and dissolved oxygen dependence of oxidation of austenitic and ferritic–martensitic alloys in supercritical water, in:

Proceedings of ICAPP, 2005, pp. 15-19.

[10] G. Was, P. Ampornrat, G. Gupta, S. Teysseyre, E. West, T. Allen, K. Sridharan, L. Tan, Y. Chen, X. Ren, Corrosion and stress corrosion cracking in supercritical water, Journal of Nuclear Materials, 371 (2007) 176-201.

[11] A. Fry, S. Osgerby, M. Wright, Oxidation of alloys in steam environments: a review, (2002).

[12] G.S. Was, S. Teysseyre, Z. Jiao, Corrosion of austenitic alloys in supercritical water, Corrosion, 62 (2006) 989-1005.

[13] G.S. Was, P. Ampornrat, G. Gupta, S. Teysseyre, E.A. West, T.R. Allen, K. Sridharan, L. Tan, Y. Chen, X. Ren, C. Pister, Corrosion and stress corrosion cracking in supercritical water, Journal of Nuclear Materials, 371 (2007) 176-201.

[14] S. Mahboubi, Effect of Cr Content on Corrosion Resistance of Fe-Cr-Ni Alloys Exposed in Supercritical Water (SCW), Master Thesis, McMaster University, Department of Materials Science and Engineering (2014).

[15] I.G. Wright, R.B. Dooley, A review of the oxidation behaviour of structural alloys in steam, International Materials Reviews, 55 (2010) 129-167.

[16] M. Li, S.J. Zinkle, R.J.M. Konings (2012). Comprehensive Nuclear Materials. Amsterdam, 4, 667-690.

[17] S. Mahboubi, G.A. Botton, J.R. Kish, On the Oxidation Resistance of Alloy 800HT Exposed in Supercritical Water (SCW), Corrosion 71 (2015) 992-1002.

[18] Y. Tsuchiya, F. Kano, N. Saito, M. Ookawa, J. Kaneda, N. Hara, Corrosion and SCC properties of fine grain stainless steel in subcritical and supercritical pure water, in: Corrosion 2007, March 11, 2007 - March 15, 2007, National Assoc. of Corrosion Engineers International, Nashville, TN, United states, 2007, pp. 074151-0741513.

[19] R. Rapp, The transition from internal to external oxidation and the formation of interruption bands in silver-indium alloys, Acta Metallurgica, 9 (1961) 730-741.

[20] D. Guzonas, S. Penttilä, W. Cook, W. Zheng, R. Novotny, A. Sáez-Maderuelo, J. Kaneda, The reproducibility of corrosion testing in supercritical water—Results of an international interlaboratory comparison exercise, Corrosion Science, 106 (2016) 147-156.

[21] N. Otsuka, Y. Shida, H. Fujikawa, Internal-external transition for the oxidation of Fe-Cr-Ni austenitic stainless steels in steam, Oxidation of Metals, 32 (1989) 13-45.

[22] L.B. Kriksunov, D.D. Macdonald, Corrosion in supercritical water oxidation systems: a phenomenological analysis, Journal of the Electrochemical Society, 142 (1995) 4069-4073.

[23] S. Mahboubi, Y. Jiao, W. Cook, W. Zheng, D.A. Guzonas, G.A. Botton, J.R. Kish, Stability of Chromia (Cr_2O_3)-Based Scales Formed During Corrosion of Austenitic Fe-Cr-Ni Alloys in Flowing Oxygenated Supercritical Water, Corrosion, 72 (2016) 1170-1180.

[24] D.J. Young, B.A. Pint, Chromium volatilization rates from Cr2O3 scales into

flowing gases containing water vapor, Oxidation of Metals, 66 (2006) 137-153.

[25] E. Essuman, G.H. Meier, J. Zurek, M. Hansel, W.J. Quadakkers, The effect of water vapor on selective oxidation of Fe-Cr alloys, Oxidation of Metals, 69 (2008) 143-162.

[26] M. Halvarsson, J.E. Tang, H. Asteman, J.E. Svensson, L.G. Johansson, Microstructural investigation of the breakdown of the protective oxide scale on a 304 steel in the presence of oxygen and water vapour at 600 °C, Corrosion Science, 48 (2006) 2014-2035.

[27] T.R. Allen, Y. Chen, X. Ren, K. Sridharan, L. Tan, G.S. Was, E. West, D. Guzonas, 5.12 - Material Performance in Supercritical Water, in: R.J.M. Konings (Ed.) Comprehensive Nuclear Materials, Elsevier, Oxford, 2012, 279-326.

[28] X. Ru, R.W. Staehle, Historical experience providing bases for predicting corrosion and stress corrosion in emerging supercritical water nuclear technology-part 2: Review, Corrosion, 69 (2013) 319-334.

[29] Y. Jiao, W. Zheng, D.A. Guzonas, W.G. Cook, J.R. Kish, Effect of thermal treatment on the corrosion resistance of Type 316L stainless steel exposed in supercritical water, Journal of Nuclear Materials, 464 (2015) 356-364.

[30] J. Castle, H. Masterson, The role of diffusion in the oxidation of mild steel in high temperature aqueous solutions, Corrosion Science, 6 (1966) 93-104.

[31] D. Lister, R. Davidson, E. McAlpine, The mechanism and kinetics of corrosion

product release from stainless steel in lithiated high temperature water, Corrosion Science, 27 (1987) 113-140.

[32] J. Robertson, The mechanism of high temperature aqueous corrosion of stainless steels, Corrosion Science, 32 (1991) 443-465.

[33] B. Stellwag, The mechanism of oxide film formation on austenitic stainless steels in high temperature water, Corrosion Science, 40 (1998) 337-370.

[34] X. Ru, R.W. Staehle, Historical experience providing bases for predicting corrosion and stress corrosion in emerging supercritical water nuclear technology: Part 1 - Review, Corrosion, 69 (2013) 211-229.

[35] C. Sun, R. Hui, W. Qu, S. Yick, Progress in corrosion resistant materials for supercritical water reactors, Corrosion Science, 51 (2009) 2508-2523.

[36] X. Gao, X. Wu, Z. Zhang, H. Guan, E.-h. Han, Characterization of oxide films grown on 316L stainless steel exposed to H_2O_2-containing supercritical water, Journal of Supercritical Fluids, 42 (2007) 157-163.

[37] A. Crouch, J. Robertson, Creep and oxygen diffusion in magnetite, Acta metallurgica et materialia, 38 (1990) 2567-2572.

[38] D. Guzonas, M. Edwards, W. Zheng, Assessment of candidate fuel cladding alloys for the Canadian supercritical water-cooled reactor concept, Journal of Nuclear Engineering and Radiation Science, 2 (2016) 011016.

[39] Y. Zeng, D. Guzonas, Corrosion Assessment of Candidate Materials for Fuel

Cladding in Canadian SCWR, JOM, 68 (2016) 475-479.

[40] W. Zheng, D. Guzonas, K.P. Boyle, J. Li, S. Xu, Materials Assessment for the Canadian SCWR Core Concept, JOM, 68 (2016) 456-462.

[41] G.S. Was, Y. Ashida, P.L. Andresen, Irradiation-assisted stress corrosion cracking, Corrosion Reviews, 29 (2011) 7-49.

[42] S.J. Zinkle, G.S. Was, Materials challenges in nuclear energy, Acta Materialia, 61 (2013) 735-758.

[43] R. Fujisawa, K. Nishimura, T. Nishida, M. Sakaihara, Y. Kurata, Y. Watanabe, Cracking susceptibility of Ni base alloys and 316 stainless steel in less oxidizing or reducing SCW, in: Corrosion 2005, NACE International, 2005.

[44] T. Hirose, K. Shiba, M. Enoeda, M. Akiba, Corrosion and stress corrosion cracking of ferritic/martensitic steel in super critical pressurized water, Journal of Nuclear Materials, 367 (2007) 1185-1189.

[45] Y. Tsuchiya, F. Kano, N. Saito, A. Shioiri, S. Kasahara, K. Moriya, H. Takahashi, SCC and irradiation properties of metals under supercritical-water cooled power reactor conditions, GENES4/ANP2003, Kyoto, Japan, Paper, 1096 (2003) 15-19.

[46] Y. Tsuchiya, N. Saito, A. Shioiri, S. Kasahara, K. Moriya, SCC Properties of Metals Under Supercritical Water Cooled Power Reactor Conditions, in: Corrosion 2004, NACE International, 2004.

[47] Y. Watanabe, H. Abe, Y. Daigo, R. Fujisawa, M. Sakaihara, Effect of physical

property and chemistry of water on cracking of stainless steels in sub-critical and supercritical water, in: Key engineering materials, Trans Tech Publ, 2004, pp. 1031-1036.

[48] R. Zhou, E.A. West, Z. Jiao, G.S. Was, Irradiation-assisted stress corrosion cracking of austenitic alloys in supercritical water, Journal of Nuclear Materials, 395 (2009) 11-22.

[49] S. Teysseyre, Z. Jiao, E. West, G. Was, Effect of irradiation on stress corrosion cracking in supercritical water, Journal of Nuclear Materials, 371 (2007) 107-117.

[50] S. Teysseyre, G.S. Was, Stress corrosion cracking of austenitic alloys in supercritical water, Corrosion, 62 (2006) 1100-1116.

[51] S. Teysseyre, G.S. Was, Stress corrosion cracking of neutron-irradiated stainless steel in supercritical water, in: 13th International Conference on Environmental Degradation of Materials in Nuclear Power Systems 2007, April 19, 2007 - April 23, 2007, Canadian Nuclear Society, Whistler, BC, Canada, 2007, pp. 540-552.

[52] L. Zhang, K. Chen, D. Du, W. Gao, P.L. Andresen, X. Guo, Characterizing the effect of creep on stress corrosion cracking of cold worked Alloy 690 in supercritical water environment, Journal of Nuclear Materials, 492 (2017) 32-40.

[53] M.C. Hash, J.T. Busby, G.S. Was, The effect of hardening source in proton irradiation-assisted stress corrosion cracking of cold worked type 304 stainless steel, in: Effects of Radiation on Materials: 21st International Symposium, June 18, 2002 -

June 20, 2002, ASTM International, Tucson, AZ, United states, 2004, pp. 92-104.

[54] J.T. Busby, M.C. Hash, G.S. Was, The relationship between hardness and yield stress in irradiated austenitic and ferritic steels, Journal of Nuclear Materials, 336 (2005) 267-278.

[55] J.T. Busby, G.S. Was, E.A. Kenik, Isolating the effect of radiation-induced segregation in irradiation-assisted stress corrosion cracking of austenitic stainless steels, Journal of Nuclear Materials, 302 (2002) 20-40.

[56] Z. Jiao, J.T. Busby, G.S. Was, Deformation microstructure of proton-irradiated stainless steels, Journal of Nuclear Materials, 361 (2007) 218-227.

[57] Z. Jiao, G.S. Was, Localized deformation and IASCC initiation in austenitic stainless steels, Journal of Nuclear Materials, 382 (2008) 203-209.

[58] Z. Jiao, G.S. Was, Impact of localized deformation on IASCC in austenitic stainless steels, Journal of Nuclear Materials, 408 (2011) 246-256.

[59] K. Arioka, T. Yamada, T. Terachi, G. Chiba, Influence of Carbide Precipitation and Rolling Direction on Intergranular Stress Corrosion Cracking of Austenitic Stainless Steels in Hydrogenated High-Temperature Water, Corrosion, 62 (2006) 568-575.

[60] K. Arioka, T. Yamada, T. Terachi, G. Chiba, Cold Work and Temperature Dependence of Stress Corrosion Crack Growth of Austenitic Stainless Steels in Hydrogenated and Oxygenated High-Temperature Water, Corrosion, 63 (2007)

1114-1123.

[61] K. Arioka, T. Yamada, T. Terachi, R.W. Staehle, Intergranular Stress Corrosion Cracking Behavior of Austenitic Stainless Steels in Hydrogenated High-Temperature Water, Corrosion, 62 (2006) 74-83.

[62] X. Ru, R.W. Staehle, Historical experience providing bases for predicting corrosion and stress corrosion in emerging supercritical water nuclear technology: Part 3-review, Corrosion, 69 (2013) 423-447.

[63] K. Arioka, 2014 Whitney Award Lecture: Change in Bonding Strength at Grain Boundaries before Long Term SCC Initiation, in: Corrosion, 2014, pp. 403-419.

[64] F.P. Ford, P.L. Andresen, Corrosion in nuclear systems: environmentally assisted cracking in light water reactors, P. Marcus and J. Ouder, Marcel Dekker, (1994) 501-546.

[65] S.M. Bruemmer, G.S. Was, Microstructural and microchemical mechanisms controlling intergranular stress corrosion cracking in light-water-reactor systems, Journal of Nuclear Materials, 216 (1994) 348-363.

[66] M.O. Speidel, R. Magdowski, Stress corrosion cracking of stabilized austenitic stainless steels in various types of nuclear power plants, in: Ninth International Symposium on Environmental Degradation of Materials in Nuclear Power Systems-Water Reactors, Wiley Online Library, 1999, pp. 325-329.

[67] E.A. Kenik, J.T. Busby, Radiation-induced degradation of stainless steel light

water reactor internals, Materials Science and Engineering R: Reports, 73 (2012) 67-83.

[68] S.M. Bruemmer, E.P. Simonen, P.M. Scott, P.L. Andresen, G.S. Was, J.L. Nelson, Radiation-induced material changes and susceptibility to intergranular failure of light-water-reactor core internals, Journal of Nuclear Materials, 274 (1999) 299-314.

[69] P.L. Andresen, Similarity of cold work and radiation hardening in enhancing yield strength and SCC growth of stainless steel in hot water, in: Corrosion 2002, NACE International, 2002.

[70] O. Chopra, A. Rao, A review of irradiation effects on LWR core internal materials–IASCC susceptibility and crack growth rates of austenitic stainless steels, Journal of Nuclear Materials, 409 (2011) 235-256.

[71] B. Cui, J. Kacher, M. McMurtrey, G. Was, I.M. Robertson, Influence of irradiation damage on slip transfer across grain boundaries, Acta Materialia, 65 (2014) 150-160.

[72] J.W. Kim, T.S. Byun, Analysis of tensile deformation and failure in austenitic stainless steels: Part I – Temperature dependence, Journal of Nuclear Materials, 396 (2010) 1-9.

[73] J.W. Kim, T.S. Byun, Analysis of tensile deformation and failure in austenitic stainless steels: Part II – Irradiation dose dependence, Journal of Nuclear Materials, 396 (2010) 10-19.

[74] J.P. Robertson, I. Ioka, A.F. Rowcliffe, M.L. Grossbeck, S. Jitsukawa, Temperature dependence of the deformation behavior of type 316 stainless steel after low temperature neutron irradiation, in: Proceedings of the 1996 18th International Symposium: Effects of Radiation on Materials, June 25, 1996 - June 27, 1996, ASTM, Hyannis, MA, USA, 1999, 671-688.

[75] K. Arioka, T. Yamada, T. Terachi, T. Miyamoto, Dependence of Stress Corrosion Cracking for Cold-Worked Stainless Steel on Temperature and Potential, and Role of Diffusion of Vacancies at Crack Tips, Corrosion, 64 (2008) 691-706.

[76] J.T. Busby*, M. Sowa, G.S. Was, E.P. Simonen, Post-irradiation annealing of small defect clusters, Philosophical Magazine, 85 (2005) 609-617.

[77] Z. Jiao, J. Busby, R. Obata, G. Was, Influence of localized deformation on irradiation-assisted stress corrosion cracking of proton-irradiated austenitic alloys, in: 12th International conference on environmental degradation of materials in nuclear pPower systems—water reactors. Salt Lake City, Utah, 2005.

[78] P. Ahmedabadi, V. Kain, K. Arora, I. Samajdar, S.C. Sharma, S. Ravindra, P. Bhagwat, Radiation-induced segregation in austenitic stainless steel type 304: Effect of high fraction of twin boundaries, Materials Science and Engineering: A, 528 (2011) 7541-7551.

[79] P.M. Ahmedabadi, V. Kain, I. Samajdar, M. Gupta, S. Sharma, P. Bhagwat, Effect of prior cold-work on radiation-induced segregation in proton-irradiated austenitic

stainless steel, Corrosion Science, 60 (2012) 153-164.

[80] K. Arioka, T. Miyamoto, T. Yamada, M. Aoki, Role of Cavity Formation in Crack Initiation of Cold-Worked Carbon Steel in High-Temperature Water, Corrosion, 69 (2013) 487-496.

[81] K. Arioka, T. Miyamoto, T. Yamada, T. Terachi, Formation of Cavities Prior to Crack Initiation and Growth on Cold-Worked Carbon Steel in High-Temperature Water, Corrosion, 66 (2010) 015008-015008-015014.

[82] K. Arioka, T. Yamada, T. Miyamoto, M. Aoki, Intergranular Stress Corrosion Cracking Growth Behavior of Ni-Cr-Fe Alloys in Pressurized Water Reactor Primary Water, Corrosion, 70 (2014) 695-707.

[83] K. Arioka, T. Yamada, T. Miyamoto, T. Terachi, Dependence of Stress Corrosion Cracking of Alloy 690 on Temperature, Cold Work, and Carbide Precipitation—Role of Diffusion of Vacancies at Crack Tips, Corrosion, 67 (2011) 035006-1.

[84] P.L. Andresen, M.M. Morra, Effect of rising and falling K profiles on SCC growth rates in high-temperature water, Journal of pressure vessel technology, 129 (2007) 488-506.

[85] G.E. Dieter, D.J. Bacon, Mechanical metallurgy, 3rd Edition, New York: McGraw-hill, 1986.

[86] J. Cadek, Creep in metallic materials, New York: Elsevier, 1988.

[87] T.H. Courtney, Mechanical behavior of materials, Boston: McGraw-Hill, 2000.

[88] S.D. Antolovich, R.W. Armstrong, Plastic strain localization in metals: origins and consequences, Progress in Materials Science, 59 (2014) 1-160.

[89] B.F. Dyson, Continuous cavity nucleation and creep fracture, Scripta Metallurgica, 17 (1983) 31-37.

[90] W. Zheng, J. Luo, M. Li, D. Guzonas, W. Cook, Stress corrosion cracking of SCWR candidate alloys: A review of published results, in: The 5th International Symposium on Supercritical-Water-Cooled Reactors (ISSCWR-5), Vancouver, BC, Canada, March, 2011, 13-16.

[91] R. Novotny, P. Hahner, J. Siegl, P. Hausild, S. Ripplinger, S. Penttila, A. Toivonen, Stress corrosion cracking susceptibility of austenitic stainless steels in supercritical water conditions, Journal of Nuclear Materials, 409 (2011) 117-123.

[92] Y. Behnamian, A. Mostafaei, A. Kohandehghan, B.S. Amirkhiz, J. Li, R. Zahiri, E. Aghaie, W. Zheng, D. Guzonas, M. Chmielus, Internal oxidation and crack susceptibility of alloy 310S stainless steel after long term exposure to supercritical water at 500° C, The Journal of Supercritical Fluids, 120 (2017) 161-172.

[93] J. Kaneda, S. Kasahara, F. Kano, N. Saito, T. Shikama, H. Matsui, Material development for supercritical water-cooled reactor, Proc. ISSCWR-5, Vancouver, Canada, March 13 (2011) 2011.

[94] G.S. Was, S. Teysseyre, J. McKinley, Corrosion and Stress Corrosion Cracking of Iron and Nickel-base Austenitic Alloys in Supercritical Water, in: Corrosion 2004,

NACE International, 2004.

[95] Q. Peng, S. Teysseyre, P. Andresen, G. Was, Stress corrosion crack growth in type 316 stainless steel in supercritical water, Corrosion, 63 (2007) 1033-1041.

[96] P. Ampornrat, G. Gupta, G.S. Was, Tensile and stress corrosion cracking behavior of ferritic–martensitic steels in supercritical water, Journal of Nuclear Materials, 395 (2009) 30-36.

[97] H. Je, A. Kimura, Stress corrosion cracking susceptibility of oxide dispersion strengthened ferritic steel in supercritical pressurized water dissolved with different hydrogen and oxygen contents, Corrosion Science, 78 (2014) 193-199.

3. Microstructure Instability of Candidate Fuel Cladding Alloys: Corrosion and Stress Corrosion Cracking Implications

Y. Jiao, W. Zheng, D. Guzonas and J. Kish. Microstructure instability of candidate fuel cladding alloys: corrosion and stress corrosion cracking implications. JOM, 68 (2016) 485-489.

3.1 Introduction

This chapter reproduces an invited published article that provides a concise literature review of the microstructure instability expected from prolonged exposure of the fuel cladding to both high temperature (thermal ageing) and radiation (irradiation damage) and the associated corrosion and SCC implications for the Canadian SCWR design concept. The article was invited to be part of a special issue dedicated to the status (at the time of publication) of materials selection for the Canadian SCWR design concept. The implications section in this article provides the rationale underpinning research described in this thesis (next four Chapters).

Prof. Kish at McMaster University and Prof. Zheng at CanmetMATERIALS are my supervisors; Dr. Guzonas was my committee member before his retirement. They were giving me guidance, instruction and edit manuscript. I was responsible for conceiving the research questions, collecting and analyzing the data, and writing the manuscripts. The study was approved by the McMaster Research Ethics Board at

McMaster University (Hamilton, Ontario).

3.2 Selection of Fuel Cladding Materials

The selection of a suitable corrosion-resistant fuel cladding material for the Canadian supercritical water-cooled reactor (SCWR) concept has received considerable attention [1, 2]. The extreme nature of the predicted in-service environment includes a range of supercritical water (SCW) coolant temperatures (350-625 °C), high pressure (25 MPa) and dose of neutron irradiation (up 9.5 dpa) [1]. From a corrosion resistance perspective, key attributes include an acceptable level of resistance to both general corrosion (oxidation) and stress corrosion cracking damage. Austenitic Fe-Cr-Ni alloys were identified as promising candidates early on in development of the Canadian SCWR concept [2] and the results of plethora of corrosion resistance assessment testing conducted by all the Generation IV International Forum partners support their continued consideration [1]. In large part, the corrosion resistance assessment testing has been conducted using as-received (typically mill-annealed) material in as-machined condition, without much consideration of the microstructure instability that is expected to occur from simultaneous exposure to both high temperature and radiation during the in-service life (~30,000 h) of the fuel cladding. While the effect of irradiation damage on the corrosion and stress corrosion cracking (SCC) resistance has been given some consideration [3-5], the effect of thermal ageing damage has only been recently been recognized as a possible key factor affecting the corrosion resistance [6, 7]. The purpose of this paper is to introduce major aspects of microstructure instability expected to occur within an austenitic Fe-Cr-Ni alloy fuel cladding from both high temperature (thermal ageing) and radiation exposure and discuss possible ways in which it could impact the general corrosion and SCC resistance in the SCW coolant. Given the high temperature requirement for microstructure instability, focus has been placed on the corrosion and SCC resistance of the fuel cladding under the conditions expected at core outlet: maximum coolant temperature of 625 °C and 800 °C for the cladding. Various radiation induced precipitates may form at this temperature range as a result of radiation induced segregation (RIS) at defect sinks [8]. For example, some of the slowly diffusing elements (Ni), which move inside the metals by interstitial mechanism can become enriched at sinks such as grain boundaries whereas the faster-moving elements such as Cr and Mn, as well as Mo, can be depleted with irradiation at or near sinks like grain boundaries. Irradiation temperature, the dose, and the dose rate are the primary variables that can affect the degree of RIS.

3.3 Microstructure Instability

Comprehensive reviews of the microstructure instability of austenitic Fe-Cr-Ni alloys resulting from high temperature [9, 10] and radiation exposure (within the context of light water reactors) [8, 11, 12] are available in the literature: only a concise overview of each is provided below.

3.3.1 High Temperature Exposure

The microstructure instability predominantly includes the temperature/time-dependent nucleation and growth of secondary phases: typically first on the grain boundaries and then within the grains. The sequence is typically captured in a time-temperature precipitation type of diagram, which is alloy-specific. In general, short-term exposure is well known to "sensitize" the microstructure, in which Cr-rich carbides (such as $M_{23}C_6$) form. These carbides can decompose with prolonged exposure to form M_6C carbides: a phase with a variable composition and stability strongly linked to other constituents. Intended preferential formation of Ti, Nb or Zr carbides, in strong competition with Cr-rich carbides can take place when Ti, Nb or Zr is added as a minor alloying element to "stabilize" the microstructure against intergranular corrosion and enhance creep resistance. More complex intermetallic phases enriched with the solute alloying elements (Cr, Ni and Mo) such as chi (χ), laves (η) and sigma (σ) require a longer time to form. The χ and η phases contain Mo, and, therefore are of more concern to Mo-containing austenitic Fe-Cr-Ni alloys. The χ phase requires the shortest amount of time to form, whereas the σ phase requires the longest. At 700 °C, for instance, χ phase was reported to formed after about 5 hours in solution annealed Type 316L whereas σ phase precipitation takes more than 100 hours [10]. Formation of the σ phase is usually associated with dissolution of carbides, but it can also form independently. The η phase forms predominantly within the grains and only occasionally on grain boundaries in competition with χ phase and σ phases [10].

3.3.2 Radiation Exposure

The microstructure instability predominantly includes radiation-induced segregation (RIS), defect formation (vacancies, interstitials and dislocation loops and channels), hydrogen/helium gas bubble generation and secondary phase precipitation. The extent of this damage depends on the irradiation dose, flux, irradiation spectrum, and the temperature. At low temperatures, vacancy migration and emission are slow, resulting in high probability of recombination of the point defects; thus RIS is unlikely to occur. At high temperatures the RIS is also not possible because of the high mobility of the defects due to recombination by back diffusion. RIS reaches a maximum at intermediate temperatures. The damage structure when irradiated below 300 °C generally consists of dislocation loops ("black spots" and "Frank loops"), without any visible formation of cavities or second phase precipitates or detectable RIS. The damage structure when irradiated above 350 °C (up to 600 °C) generally consists of cavities (induced by both vacancy coalescence and gas bubble growth), large Frank loops, RIS and secondary phase precipitates [8, 12]. RIS involves the depletion of Cr and the concomitant enrichment of Ni and possibly other alloying element (such as Si and P) at defects sinks (such as grain boundaries or cavities). Secondary phase precipitation requires a high dose (above 30 dpa) in addition to high temperature. The precipitates are generally classified as either [8]: (i) radiation-enhanced/ impeded (ii) radiation-modified or (iii) radiation-induced. The first two types involve precipitates common with high temperature exposure alone, with radiation affecting the nucleation and growth rate as well as the chemistry. The third type involves precipitates not common to high temperature exposure alone. Hydrogen/helium gas bubble formation is insensitive to compositional variation within austenitic Fe-Cr-Ni alloys. Helium is generated by the transmutation of ^{10}B (n, α) reaction or alloyed ^{58}Ni. Under a high thermal neutron flux, helium is generated via the sequential ^{58}Ni(n,γ) ^{59}Ni(n,α)^{56}Fe reaction. As the accumulation of ^{59}Ni takes time to occur with continuing bombardment, significant amount of He production is seen after certain irradiation fluence. Fast energy (n, p) reactions can also produce significant amounts of hydrogen during irradiation with the alloyed ^{58}Ni as well. The helium/hydrogen generated during irradiation can coalesce and form bubbles, which in turn can coalesce into cavities. Helium can also segregate at the grain boundaries at high temperatures, causing a loss of ductility.

3.4 Corrosion and Stress Corrosion Cracking Implications

3.4.1 Corrosion Implications

The corrosion resistance of austenitic Fe-Cr-Ni alloys exposed in SCW relies on the formation of a protective external Cr-rich oxide layer on the surface of the alloy for acceptable protection [1, 2]. The formation and stability of the protective Cr-rich oxide in turn relies on the enhanced diffusion of Cr on active short circuit diffusion paths, such as dislocation and twin and grain boundaries [7]. Thus, any microstructure instability that either depletes or binds Cr at or on these active short circuit diffusion paths is of some concern, as it may adversely affect Cr diffusion. An example of such microstructure instability in Type 310S stainless steel from high temperature exposure is shown in Figure 3.1. The sensitized treatment (S: 100 h at 650 °C for 100 h) caused the discontinuous formation of Cr-rich $M_{23}C_6$ carbides on the grain boundaries with an associated Cr-depleted zone in the matrix adjacent to the grain boundary. In contrast, the thermal treatment (TT: 1000 h at 800 °C) caused the discontinuous formation of σ phase on the grain boundaries without an associated Cr depleted matrix zone adjacent to the grain boundaries.

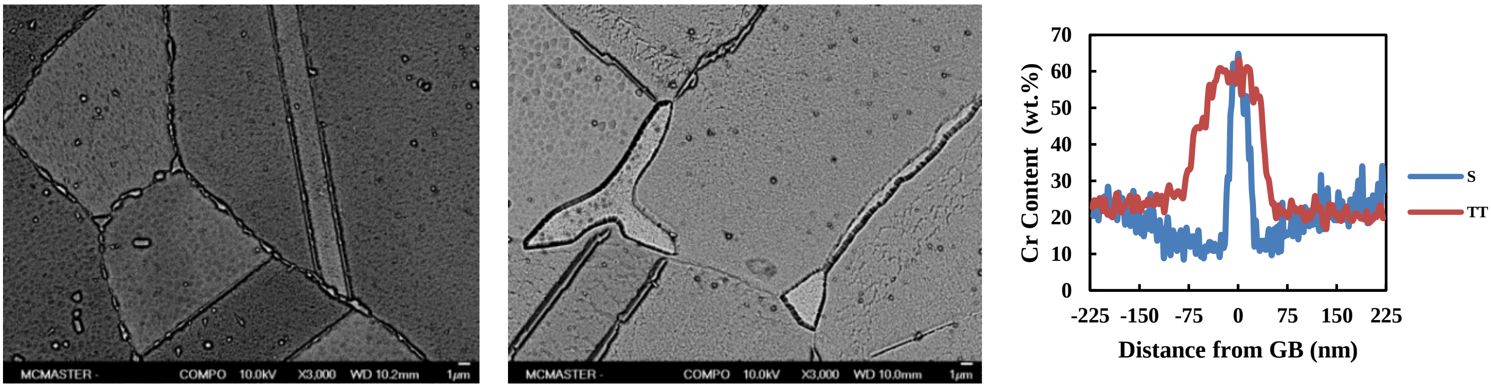
(a) Type 310S-S (b) Type 310S-TT (c) TEM-EDS Line Profile

Figure 3.1 SEM cross-section image showing the typical features of the grain boundary region in Type 310S after high temperature exposure: (a) S material and (b) TT material. (c) TEM-EDS line profiles showing the elemental composition variation across the grain boundary region.

The effect of such microstructure instability on the corrosion resistance in SCW is shown in Figure 3.2 for testing conducted using a static autoclave (stagnant deaerated condition) and a flow loop autoclave (flowing aerated (8 ppm dissolved oxygen gas) condition). The comparison indicates that the microstructure instability resulting from high temperature had little influence on the weight gain relative to the solution annealed material (SA: 1 h at 1050 °C), albeit after only relatively short exposure times. It is possible that a detrimental effect may occur if a continuous network of intermetallic phase precipitates formed on the short-circuit grain boundary diffusion paths. However, such formation is unlikely over the in-service life of the fuel cladding (about 30,000 h) based on published predictions of intermetallic phase precipitate volume fractions formed in Type 316L stainless steel after prolonged exposure times (up to 100,000 h at 700 °C) [13]. Figure 3.2 also indicates that any microstructure instability effect pales in comparison to the combined effect of flow and dissolved oxygen content.

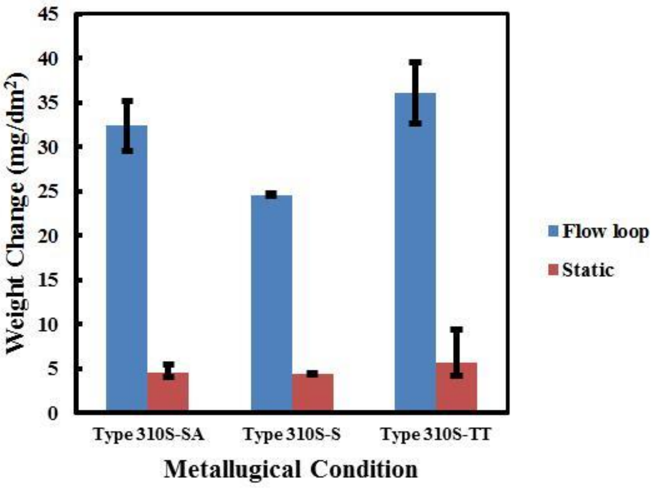

Figure 3.2 Weight change data for pre-treated Type 310S stainless steel after exposure

in 25 MPa SCW at 550 °C.

3.4.2 Stress Corrosion Cracking Implications

The SCC resistance of austenitic Fe-Cr-Ni alloys in SCW is influenced by its microstructure and metallurgical factors such as grain size, degree of cold work and irradiation damage [3-5, 12]. Grain boundary chemistry is also well known to affect the susceptibility to intergranular SCC as is the case with sensitized stainless steels. In terms of microstructure instability, pre-exposure to high temperature proton irradiation has been found to significantly increase the intergranular SCC severity relative to the non-irradiated case, regardless of the irradiation dose or temperature [5, 14]. In this case, the increased intergranular cracking severity correlated with both the contaminant-increased hardening and RIS (i.e., decreased grain boundary Cr content). Given the expected intergranular cracking mode, grain boundary precipitation from exposure to high temperature and radiation and the associated embrittlement is also a key concern.

The effect of thermal ageing pre-treatments on the SCC susceptibility is shown in Figure 3.3. All three pre-treated samples strained to 5% in SCW (25 MPa at 500 °C with 8 ppm dissolved oxygen) showed no evidence of SCC. Note that only 1.5% total deformation over the lifetime of the fuel cladding is expected in the Canadian SCWR concept. Therefore, the slow strain rate testing was terminated far in advance of attaining the ultimate tensile strength. At first glance the results seem promising, but a more detailed investigation is required to better understand the risks associated with second phase grain boundary precipitate formation, which could take much longer time to exhibit its effects. One rather significant finding from this preliminary work was the internal micro-cracking that was observed within the σ phase of the TT material. It is unclear at the moment how this will affect the mechanical integrity over the lifetime of the fuel cladding as this micro-cracking is found embedded inside the small isolated σ phase.

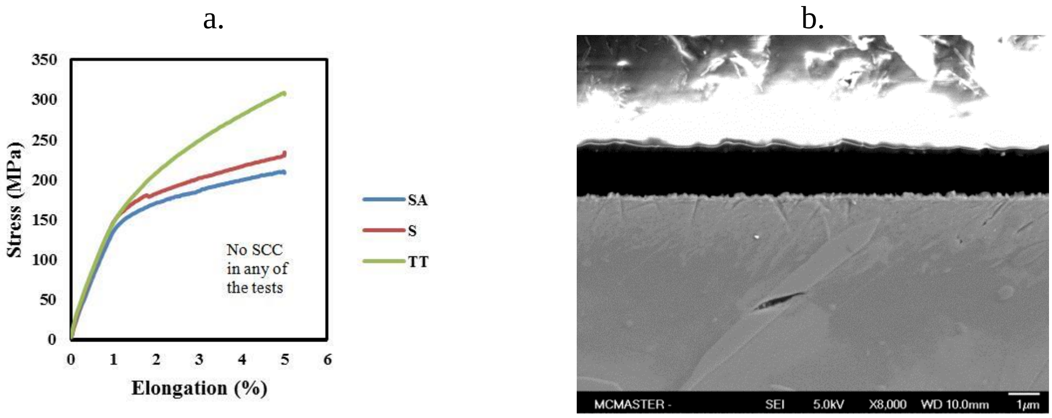

Figure 3.3 Results of slow strain rate testing of pre-treated Type 310S stainless steel in 25 MPa SCW at 500 °C with 8 ppm dissolved oxygen using a flow-loop autoclave.

The correlation between increased intergranular cracking severity with both increased hardness and degree of RIS [5, 14] raises an important question about which factor, chemical (i.e., sensitization) or mechanical (grain boundary strength and its substructures), plays a more important role in the intergranular cracking mechanism. Any attempt to control the fuel cladding microstructure to optimize SCC resistance requires a good understanding of the critical determining factors. Thus, an effort to differentiate between the critical chemical and mechanical factors is of significant merit in this regard. While it is understood that the roles of each factor, and the possible interactions between them in terms of cracking, can be complex, the first attempt in this effort is a general classification of the variables (as being weak or strong) into the “chemistry” or the “microstructure” group. An example of such an approach currently being pursued is shown in Figure 3.4, in which an intergranular SCC susceptibility map has been sub-divided into four quadrants within chemical and mechanical signature space. The chemical signature is a measure of the degree of chemical inhomogeneity (such as sensitization and segregation) across the grain boundary, whereas the mechanical signature is the strength of the grain interior and the grain boundaries which is indicative of the underlying microstructural characteristics associated with deformation and defect accumulation. Pre-treated microstructures using a combination of thermal ageing, proton irradiation and cold working are being assessed to populate this 2-D property map. Targeted microstructures (different pre-treatment combinations) will be selected for subsequent slow strain rate testing in SCW to assess the intergranular SCC resistance using parameters such as the number of cracks per unit area for crack initiation and/or total crack length per unit area, depth of penetration or longest crack length for propagation. The most suitable parameter will be added as the third axis to yield a 3-D property space.

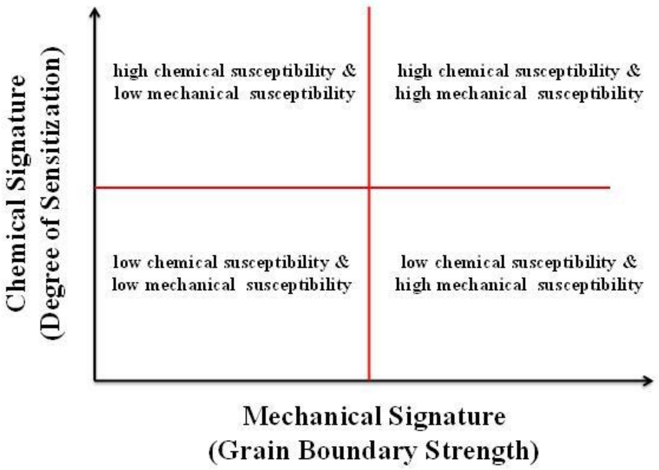

Figure 3.4 Intergranular stress corrosion cracking susceptibility property space.

A key part of this effort is also related to the issues of irradiation-induced microstructures and their role in SCC. For example, the formation of deformation channels is well established in irradiated metals and alloys such as austenitic stainless steels [12, 15, 16]. As the formation of such microstructural features are associated with the occurrence of SCC [12, 15], it makes one wonder what roles of such irradiation-induced physical metallurgical features play in the initiation and the propagations of the cracks. It is probable that the intersecting of such concentrated deformation bands at the grain boundaries causes a disruption (or a breakage) of the oxide formed at the grain boundary, leading to crack initiation or propagation. It remains to be known at which macroscopic deformation level (in terms of strains) SCC will occur in a well-defined cold-worked or irradiated microstructure. If the localization of deformation in the microstructure is the prerequisite for SCC initiation, de-localization of the plasticity along the grain boundaries can be an approach through which SCC sensitivity of alloys is mitigated. In this regard, the effects of grain-refining should be systematically investigated.

One beneficial effect of exposure to high temperature (>600 °C), as far as SCC is concerned, is that thermal recovery in the microstructure can anneal out some of the deformation sub-structures in the grain interior and along the grain boundary. At the high end of the temperature range expected for the Canadian SCWR, recovery can be so fast that any pre-cold working dislocation structures will disappear well in advance of the irradiation damage reaching a significant level; damages due to irradiation in the candidate cladding alloys are expected to be in the range of 2~3 dpa per year. Of course, grain boundary failure due to creep cracking can then be a concern for these very high temperatures if there is sufficient stress, either axial or circumferential, sustained in the cladding wall.

3.5 Summary and Conclusions

Microstructure instability of an austenitic Fe-Cr-Ni alloy fuel cladding from exposure to both high temperature and radiation is inevitable within the Canadian SCWR concept given the predicted maximum fuel cladding temperature of 800 °C for some locations in the core. The instability will be manifested over various length scales, ranging from point defects to second phase precipitates depending on irradiation dose and temperature and exposure time. Corrosion testing, albeit at short exposure times, suggests that microstructural instability will not have a significant impact on the corrosion resistance of austenitic Fe-Cr-Ni alloys at temperatures approaching those at the coolant core outlet. In contrast, SCC testing suggests a non-negligible role of thermal ageing: that microstructural instability could have a significant impact on the internal micro-cracking of austenitic Fe-Cr-Ni alloys at temperatures approaching those found at the core outlet. This is particularly associated with the formation of sigma phase in the microstructure. Preliminary findings of micro-cracking along the interfaces of the sigma and the austenite phases as well as inside the sigma phase in the thermally aged samples warrant further investigation, as this brittle phase can also be formed by radiation. As there are several types of precipitates in alloys of relevant composition forming in the cladding temperature range, as a thermal process or as a result of irradiation, effort is needed to examine their influence on a base by case basis. A research effort towards the development of a susceptibility map to differentiate between the key chemical and mechanical factors has been undertaken to achieve this goal.

3.6 References

[1] D. Guzonas, R. Novotny, Supercritical water-cooled reactor materials – Summary of research and open issues, Progress in Nuclear Energy, 77 (2014) 361-372.

[2] D.A. Guzonas, W.G. Cook, Cycle chemistry and its effect on materials in a supercritical water-cooled reactor: a synthesis of current understanding, Corrosion Science, 65 (2012) 48-66.

[3] Y. Tsuchiya, F. Kano, N. Saito, A. Shioiri, S. Kasahara, K. Moriya, H. Takahashi, SCC and irradiation properties of metals under supercritical-water cooled power reactor conditions, GENES4/ANP2003, Kyoto, Japan, Paper, 1096 (2003) 15-19.

[4] S. Teysseyre, G.S. Was, Stress corrosion cracking of neutron-irradiated stainless steel in supercritical water, in: 13th International Conference on Environmental Degradation of Materials in Nuclear Power Systems 2007, April 19, 2007 - April 23, 2007, Canadian Nuclear Society, Whistler, BC, Canada, 2007, pp. 540-552.

[5] R. Zhou, E.A. West, Z. Jiao, G.S. Was, Irradiation-assisted stress corrosion cracking of austenitic alloys in supercritical water, Journal of Nuclear Materials, 395 (2009) 11-22.

[6] Y. Jiao, W. Zheng, D.A. Guzonas, W.G. Cook, J.R. Kish, Effect of thermal treatment on the corrosion resistance of Type 316L stainless steel exposed in supercritical water, Journal of Nuclear Materials, 464 (2015) 356-364.

[7] J. Li, W. Zheng, S. Penttilä, P. Liu, O.T. Woo, D. Guzonas, Microstructure stability of candidate stainless steels for Gen-IV SCWR fuel cladding application, Journal of Nuclear Materials, 454 (2014) 7-11.

[8] P.J. Maziasz, Overview of microstructural evolution in neutron-irradiated austenitic stainless steels, Journal of Nuclear Materials, 205 (1993) 118-145.

[9] T. Sourmail, Precipitation in creep resistant austenitic stainless steels, Materials science and technology, 17 (2001) 1-14.

[10] B. Weiss, R. Stickler, Phase instabilities during high temperature exposure of 316 austenitic stainless steel, Metallurgical Transactions, 3 (1972) 851-866.

[11] E.A. Kenik, J.T. Busby, Radiation-induced degradation of stainless steel light water reactor internals, Materials Science and Engineering R: Reports, 73 (2012) 67-83.

[12] G.S. Was, Y. Ashida, P.L. Andresen, Irradiation-assisted stress corrosion cracking, Corrosion Reviews, 29 (2011) 7-49.

[13] T. Sourmail, H. Bhadeshia, Modelling simultaneous precipitation reactions in austenitic stainless steels, Calphad, 27 (2003) 169-175.

[14] S. Teysseyre, Z. Jiao, E. West, G. Was, Effect of irradiation on stress corrosion cracking in supercritical water, Journal of Nuclear Materials, 371 (2007) 107-117.

[15] Z. Jiao, G.S. Was, Localized deformation and IASCC initiation in austenitic stainless steels, Journal of Nuclear Materials, 382 (2008) 203-209.

[16] Z. Jiao, G.S. Was, Impact of localized deformation on IASCC in austenitic stainless steels, Journal of Nuclear Materials, 408 (2011) 246-256.

4. Effect of Thermal Pre-treatment on the Corrosion of Stainless Steel in Flowing Supercritical Water

Y. Jiao, J. Kish, G. Steeves, W. Cook, W. Zheng and D. Guzonas. Effect of Thermal Pretreatment on the Corrosion of Stainless Steel in Flowing Supercritical Water, Journal of Nuclear Engineering and Radiation Science, 2 (2016) 011015.

4.1 Introduction

This chapter reproduces another published article, which documents the research conducted to elucidate the effect of thermal ageing on the corrosion behaviour of Type 310S in SCW. The Results and Discussion sections in the article (chapter) specifically address the corrosion implications of a long-term thermally-aged microstructure in SCW described in Section 1.2 above and in the Corrosion Implications Section in Chapter 3.

Prof. Kish at McMaster University and Prof. Zheng at CanmetMaterials are my supervisors; Dr. Guzonas was my committee member before his retirement. They were giving me guidance, instruction and edit manuscript. Prof. Cook at University of New Brunswick is our collaborator and gave us suggestions and comments for SCW oxidation tests. Mr. Steeves was a Master student of Prof. Cook and conducted the SCW oxidation tests for us. I was responsible for conceiving the research questions, collecting and analyzing the data, and writing the manuscripts. The study was approved by the McMaster Research Ethics Board at McMaster University (Hamilton, Ontario).

4.2 Oxidation of Stainless Steels in SCW

There has been a significant corrosion research effort dedicated to screening candidate materials for use as a fuel cladding for supercritical water-cooled reactor (SCWR) concepts [1-5]. Austenitic stainless steels have received significant attention due to their relatively good corrosion resistance in supercritical water (SCW). Despite the current state of knowledge, a key gap exists: the effect on the corrosion resistance of the slow microstructural evolution due to thermal ageing. For the most part, studies reporting the corrosion resistance of austenitic stainless steels exposed in SCW have been conducted using as-received (typically mill-annealed) material, without much consideration of the microstructural changes that have occurred during testing at high temperatures. This is of particular significant to the Canadian SCWR concept, because of the higher core outlet temperature; the peak cladding temperature may be as high as 800 °C and the in-service life of the cladding is roughly 30,000 h.

Short term thermal ageing or treatment is well known to “sensitize” the microstructure of 300 series stainless steels in which Cr-rich carbide (such as $M_{23}C_6$) precipitates form on the grain boundaries, rendering the grain boundary region more susceptible [6, 7]. Other intermetallic precipitates such as the chi (χ), laves (η) and sigma (σ) phases take longer times to form [8-11]. Only very recently have thermal ageing effects on the corrosion and stress corrosion cracking resistance of austenitic stainless steels in SCW been given consideration [12-14]. We reported on the effect of thermal ageing on the short-term (500 h) corrosion resistance of Type 316L stainless steel in 25 MPa SCW at 550 °C using a static autoclave with no attempt to maintain the initial 8 ppm dissolved oxygen content [12]. It was found that although relatively large intermetallic precipitates located at the scale/alloy interface locally affected oxide scale formation, their discontinuous formation did not affect the short-term overall apparent corrosion resistance.

The current study was conducted to evaluate the effect of prior thermal treatment on the short-term (500 h) corrosion resistance of Type 316L and Type 310S stainless steel exposed in 25 MPa SCW at 550 °C using a closed flow loop autoclave testing facility to maintain the dissolved oxygen concentration at 8 ppm. This was achieved by comparing the weight gain and oxide scale structure and composition formed on exposed mill-annealed/solution-annealed material and on thermally-treated material: the latter designed to precipitate the expected intermetallic phases in each alloy. The intermetallic phases formed in each alloy were characterized using transmission electron microscopy (TEM) and associated techniques. The mode and extent of corrosion that occurred was characterized using scanning electron microscopy (SEM) coupled with X-ray energy dispersive spectroscopy (EDS).

4.3 SCW Oxidation Test

Rectangular (20 × 10 × 1 mm) samples were prepared from commercial Type 316L and Type 310S stainless steel rod product provided in the mill-annealed condition. The chemical composition was analyzed using ICP-OES (Varian Spectrometer) and combustion analysis (LECO CS230). The results are shown in Table 4.1. A small (2 mm diameter) hole was drilled into each sample near the top to facilitate mounting on a coupon tree. Type 316L samples were exposed in the mill-annealed (MA) state and a thermally-treated (TT) state. The MA state was evaluated to permit a comparison with our prior test results using a static autoclave [12]. The TT state was achieved by thermal ageing at 815 °C in nitrogen for 1000 h followed by air-cooling to room temperature to precipitate all of the expected intermetallic $M_{23}C_6$, χ, η and σ phases [15]. In contrast, Type 310S samples were exposed in a solution-annealed (SA) state along with a TT state. The SA state was achieved by thermal treating samples at 1050 °C for 1 h followed by water-quenching to room temperature. The TT state was achieved by thermal treating samples at 800 °C for 1000 h followed by air-cooling to room temperature to precipitate the expected intermetallic $M_{23}C_6$ and σ phases [16]. The treatment temperature was selected to be as close as possible to the maximum fuel cladding temperature of 800 °C expected in the Canadian SCWR concept [17], while still allowing for the sequential formation of each major intermetallic precipitate type. All heat treatments were conducted by sealing the samples in a quartz tube that was purged with high purity nitrogen gas.

Upon removal from the furnace, samples were cooled to room temperature while sealed in the nitrogen gas-purged quartz tube. A set of four samples in each state were mechanically abraded to a 800 grit surface finish using SiC abrasive papers and water as a lubricant, rinsed in acetone in an ultrasonic bath, dried using absorbent wipes and weighed prior to testing.

Table 4.1 Chemical composition (wt.%) of the commercial stainless steels studied

Alloy	Cr	Ni	Mo	Mn	Si	P	S	C	Fe
316L	16.3	10.2	2.1	1.6	0.24	0.04	0.03	0.02	Bal.
310S	24.3	19.6	0.3	1.0	0.76	0.04	0.03	0.06	Bal.

The closed flow loop autoclave testing facility available at the University of New Brunswick was used to expose the samples in SCW. Specific details regarding the design of this facility are published elsewhere [4]. Testing was conducted in flowing (200 mL/min.) 25 MPa SCW with a 8 ppm dissolved oxygen concentration at 550 °C for 500 h. The sample sets (four samples of each material) were suspended on a coupon tree that was placed inside the autoclave. The flow loop testing was interrupted at the 100 h and 250 h exposure times so that samples could be removed from the autoclave and weighed. One sample was kept for characterization during each interruption. The relatively short exposure time of 500 h was selected to prevent additional intermetallic precipitates from forming in-situ in the Type 316L-MA and Type 310S-SA materials.

The microstructure of the starting material was examined in cross-section using light optical microscopy, SEM, and TEM; the latter two techniques were coupled with

EDS. Samples were cold-mounted in cross-section using standard metallographic techniques and polished to a 1 μm surface finish. Chemical etching was conducted by contacting the polished surfaces with an acetic acid-glycerine mixture for 40 s. The SEM examination was performed using a JEOL JSM-7000F microscope equipped with a Schottky field emission gun (FEG) filament and an integrated Oxford Synergy system with INCA EDS X-ray micro-analysis using an accelerating voltage of 10 kV and a working distance of 10 mm. The TEM examination was performed using a JEOL 2010F TEM/STEM equipped with an Oxford Instruments EDS analyser using an accelerating voltage of 200 kV. TEM samples were prepared by mechanically-abrading samples to a thickness of 80 μm using SiC paper and water as a lubricant. Small foils were then punched out of the thinned samples and subsequently electrochemically polished in a perchloric acid (10%)-methanol (90%) solution at −50 °C to create a small hole in the thin foil. Randomly selected intermetallic precipitates were identified by comparing the elemental composition determined by EDS in both SEM and TEM mode with those published using the same techniques [9-11]. Selected area diffraction (SAD) in TEM mode was used on those phases that were large enough to minimize the diffraction from the austenite matrix. X-ray diffraction (XRD) after a bulk extraction was also used to help identify the intermetallic precipitates that were present after thermal treating. The bulk extraction was carried out in a hydrochloric acid (10%)-methanol (90%) solution. X-ray diffraction patterns of the extracted powder were collected using an X-ray powder diffractometer (Bruker 8D Advanced) operated with a Cu $k_{\alpha1}$ radiation source.

After the 500 h exposure, the sample sets were photographed and then re-weighed. One sample from each set was selected for a more detailed examination using SEM-EDS of the oxide scale formed. A plan-view examination of the oxide scale was conducted first using SEM (JEOL JSM-7000F) operated with an accelerating voltage of 10 kV and a working distance of 10 mm. The sample was subsequently cold-mounted in cross-section using standard metallographic techniques and polished to a 1 μm finish. SEM-EDS (JEOL JSM-7000F) operated with an accelerating voltage of 10 kV and a working distance of 10 mm was then used again to examine the oxide scale in cross-section.

4.4 Results

Figure 4.1 shows the starting microstructures as revealed using light optical microscopy. The Type 316L-MA material (Figure 4.1a) exhibited a coarse-grained structure with some twinning and MnS inclusions (verified by SEM-EDS). The Type 316L-TT material (Figure 4.1b) exhibited similar features as the MA material, but with significant intermetallic precipitation both within the grains and on the grain boundaries. The precipitation was discontinuous in both cases. The Type 310S-SA material (Figure 4.1c) exhibited a coarse-grained structure with twinning. The most striking feature was the $M_{23}C_6$ grain boundary precipitation (verified by TEM-SAD) that remained after applying the SA treatment. The Type 310S-TT material (Figure 4.1d) exhibited similar features as the SA material, but with significant intermetallic phase precipitation within the grains and on the grain boundaries to an increased extent. No surprise that majority grain boundary carbides were dissolved after 1000 h thermal treatment as a result of nucleation of intermetallic precipitates [9]. The precipitation was discontinuous in both cases. The average grain size of each material was measured using the commercial software NIS-Elements D with ASTM E1382 procedure. The Type 316L material and Type 310S material had similar grain sizes: 9.0 and 9.5 for the Type 316L MA and TT material respectively, and 7.2 and 7.0 for the Type 310S SA and TT material respectively. Thus, the prolonged thermal treatment did not induce any significant grain growth.

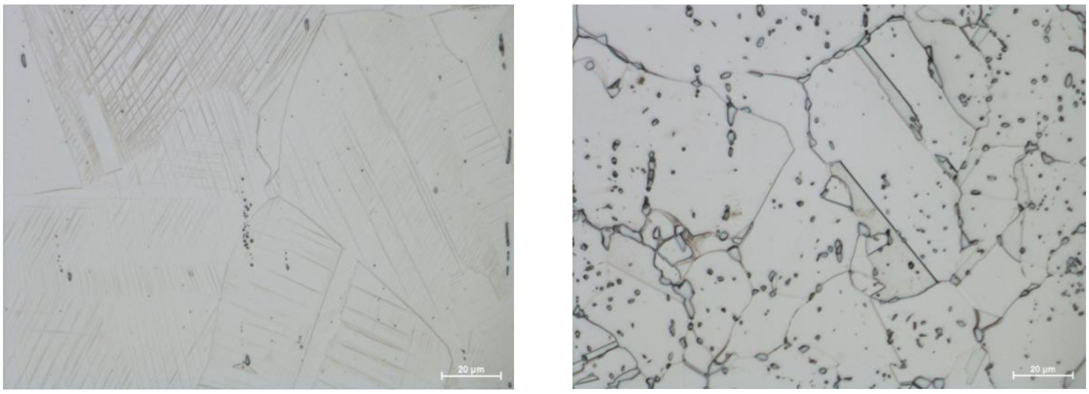
a. Type 316L-MA b. Type 316L-TT

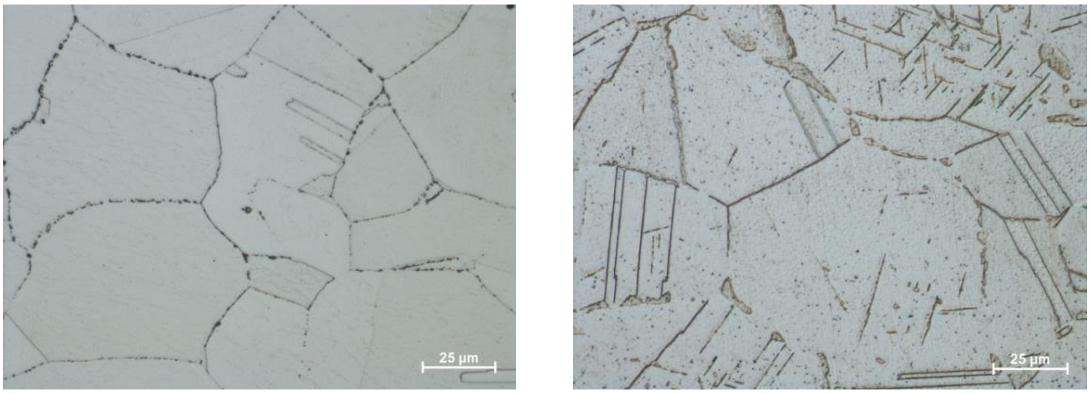
c. Type 310S-SA d. Type 310S-TT

Figure 4.1 Light optical image of the thermally pre-treated material

Figure 4.2 shows a typical result of the intermetallic phase precipitate characterization conducted using TEM-EDS. Cr-depletion was not detected in any of the intermetallic phase precipitates analyzed in either TT material. This finding implied that the extent of Cr diffusion during the prolonged exposure time (1000 h) at the high temperature (800-815 ºC) was sufficient to replenish any depletion that occurred during the nucleation and initial growth of the Cr-rich intermetallic phase precipitates.

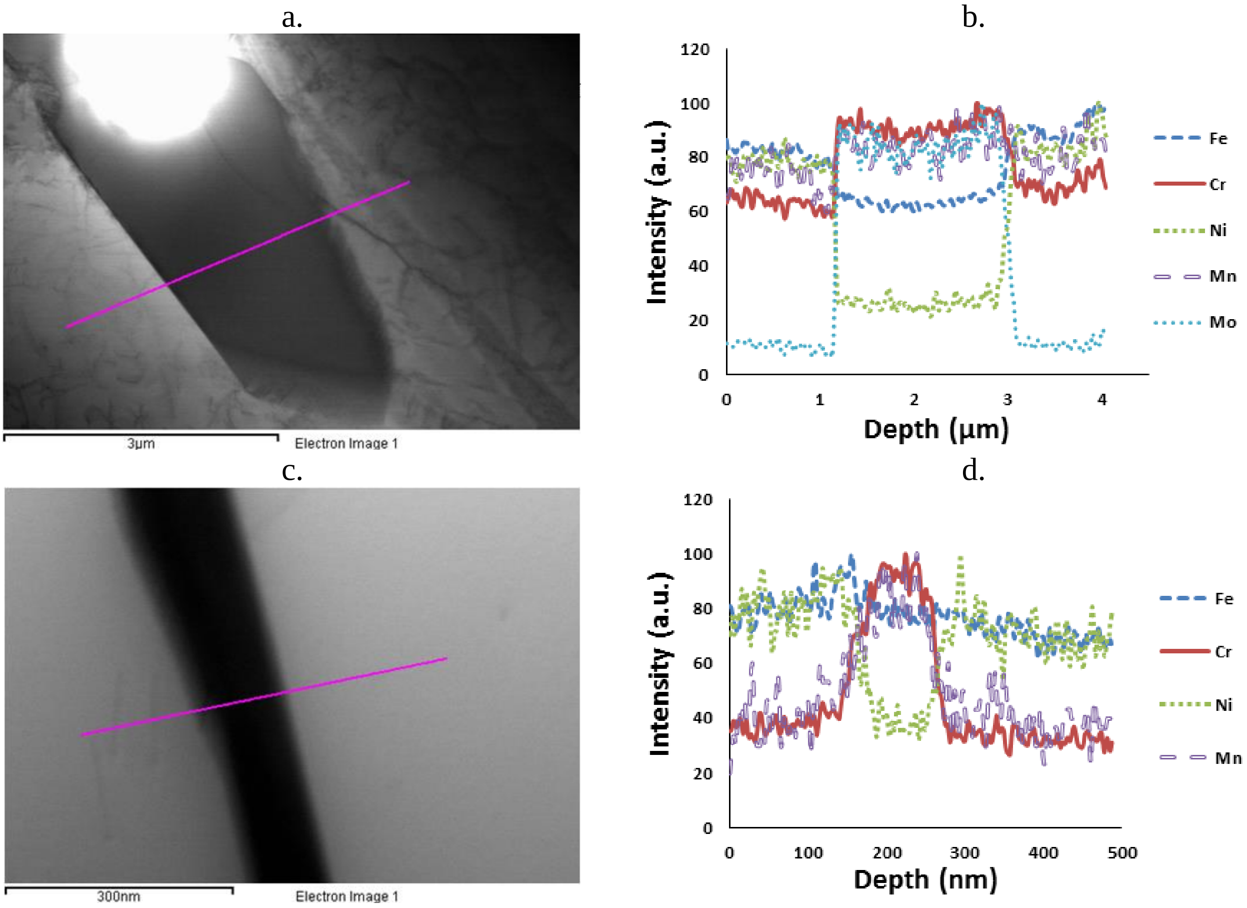

Figure 4.2 STEM bright-field image and corresponding EDS line analysis of an intermetallic precipitates present in the thermally pre-treated material

A summary of the intermetallic precipitates identified within the MA and TT material using TEM-SAD, STEM-EDS and XRD techniques is provided in Table 4.2. A relatively low population of $M_{23}C_6$ type carbides was observed within the grains and on grain boundaries in both the Type 316L-MA and Type 310S-SA material using TEM/STEM. The thermal treatment applied resulted in the precipitation of the χ and σ phases and the σ phase within the grains and on the grain boundaries of Type 316L and Type 310S respectively. Interestingly, $M_{23}C_6$ type carbide precipitates were no longer detected either within the grains or on the grain boundaries of the Type

316L-TT material and on the grain boundaries in the Type 310S-TT material. This indicates that significant dissolution of these precipitates occurred. The detection of this phase by XRD in both TT materials indicates that complete dissolution did not occur. In summary, the thermal treatment was successful in precipitating the expected phases for both alloys: $M_{23}C_6 + \chi + \eta + \sigma$ for Type 316L [15] and $M_{23}C_6 + \sigma$ for Type 310S [16].

Table 4.2 Summary of precipitates detected

Material	TEM-SAD and STEM-EDS Grain	Boundary	XRD
Type 316L-MA	$M_{23}C_6$	$M_{23}C_6$	Not Analysed
Type 316L-TT	$\chi + \sigma$	$\chi + \sigma$	$M_{23}C_6 + \chi + \eta + \sigma$
Type 310S-SA	$M_{23}C_6$	$M_{23}C_6$	Not Analysed
Type 310S-TT	$M_{23}C_6 + \sigma$	σ	$M_{23}C_6 + \sigma$

The XRD diffraction patterns of bulk extracted intermetallic phase precipitates acquired from each TT material are shown in Figure 4.3. Distinct peaks of the $M_{23}C_6$, χ, η and σ were observed in Type 316L-TT material (Figure 4.3 a), and distinct peaks of $M_{23}C_6$ and σ were observed in the Type 310S-TT material (Figure 4.3 b). The peak at 46° for the Type 316L-TT material is inherent to both the η and σ phases. The peak at 47° is inherent to the σ phase only. There were no peaks inherent to any other phases within the range of 2θ range plotted. If the entire bulk extracted particles mass was the σ phase, then the intensity of the 47° peak would be higher than the intensity of the 46° peak. However, Figure 4.3 shows that these two peaks (46° and 47°) had similar intensities. The higher than expected intensity of the 46° indicated that the η phase was likely included in bulk extracted precipitate mass. Similarly, the peaks at

37.5° and 50.5° are mainly contributed by $M_{23}C_6$ carbides due to low intensity of χ phase and η phase. However, the location of the η phase (within grains and/or on grain boundaries) was not known.

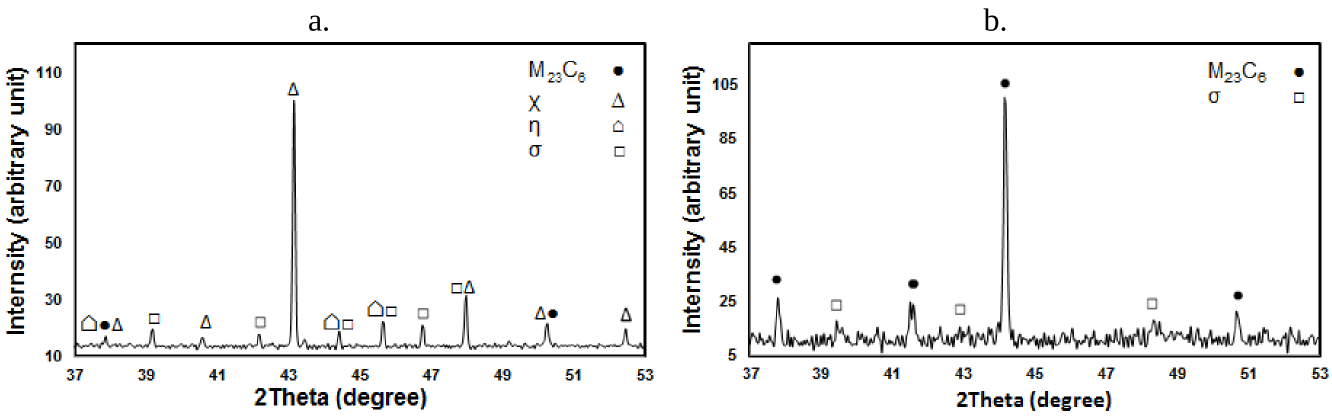

Figure 4.3 Powder XRD pattern of intermetallic precipitates of intermetallic precipitates present in the thermally pre-treated materials

Figure 4.4 compares the average weight change exhibited by each sample set after exposure in flowing 25 MPa SCW at 550 °C with 8 ppm dissolved oxygen for 500 h. The bars superimposed onto the chart mark the highest and lowest values recorded for each sample set, indicating the spread in the data. All four weight average change values were positive: indicating a significant portion of the oxide scale formed remained intact upon removal from the autoclave. The average weight gain exhibited by the TT material was higher than that of the MA material for Type 316L and the SA material for Type 310S. The difference was outside of the spread of the data for Type 316L, but was within the spread of the data for Type 310S. It was clear that alloy composition had a more significant effect than thermal treatment on the short-term corrosion resistance as shown by weight change measurements.

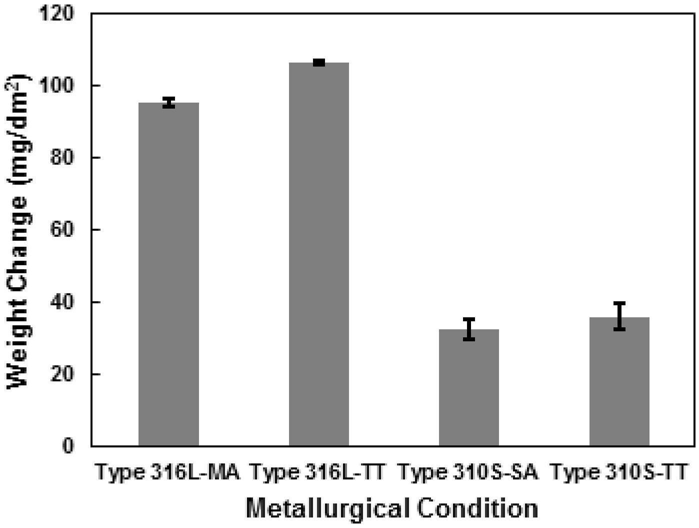

Figure 4.4 Bar chart comparing weight change data of the exposed sample sets

Figure 4.5 shows a secondary electron image (plan-view) at relatively low magnification of the oxide scale formed on each material. Both Type 316L surfaces exhibited a compact scale morphology that was randomly decorated with circular regions resembling localized exfoliated regions. There was no obvious difference between the MA and TT surfaces. Similar localized exfoliated regions were not observed on either of the Type 310S (SA and TT) surfaces.

a. Type 316L-MA b. Type 316L-TT

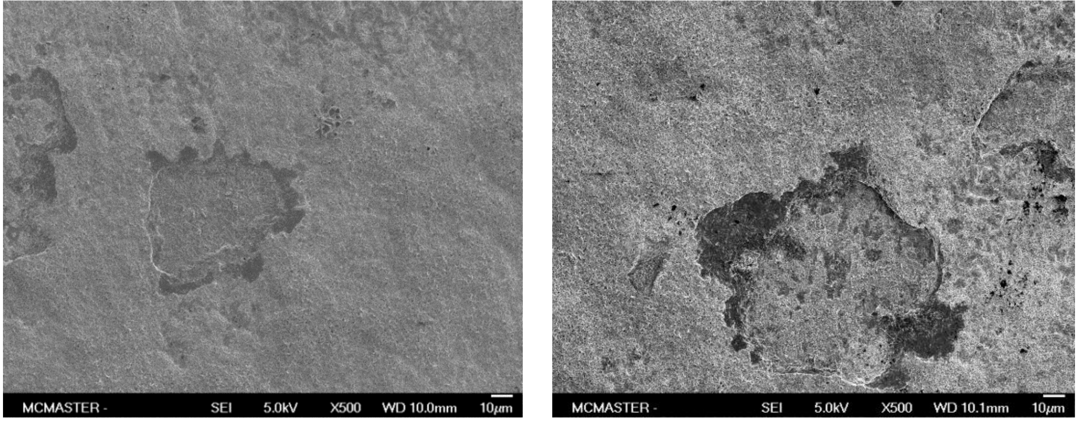

c. Type 310S-SA d. Type 310S-TT

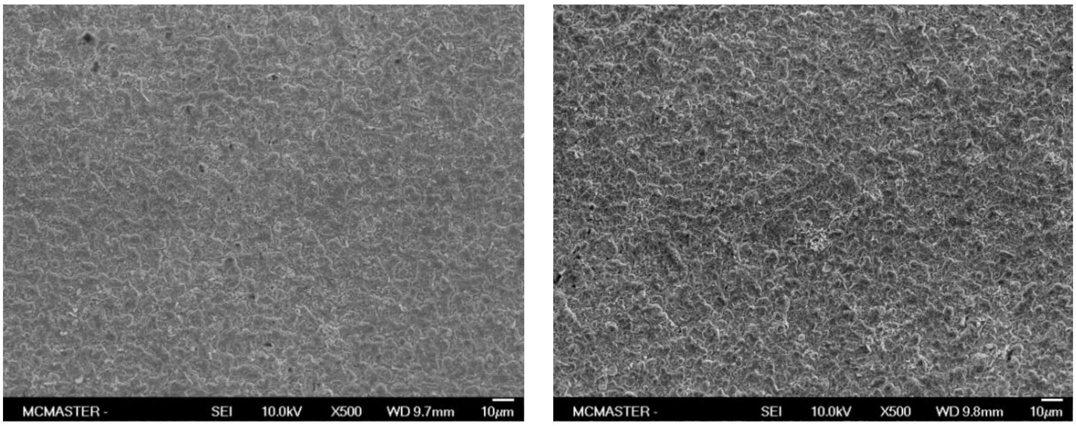

Figure 4.5 Secondary electron image (plan-view) at lower magnification of the oxide scale morphology formed on the thermally pre-treated material after exposure in SCW

Figure 4.6 shows a secondary electron image (plan-view) at higher magnification of the oxide scale formed on each material. The intact surface (non-exfoliated region) of both Type 316L materials exhibited a similar morphology, consisting of an adherent interconnecting network of fine platelets. The surface of both Type 310S materials also exhibited a similar morphology, consisting of an adherent discontinuous network of coarse nodules residing on top of a more compact inner layer. No evidence of any significant cracking or spallation was found.

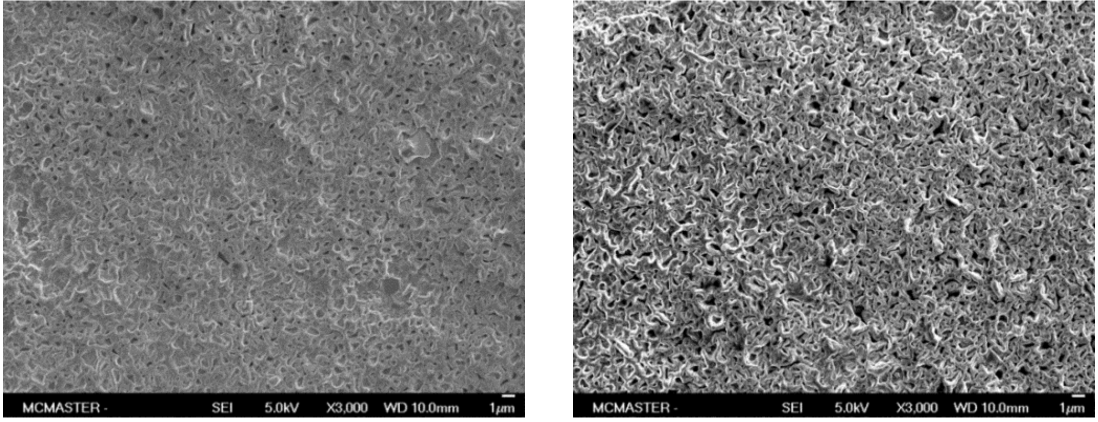
a. Type 316L-MA

b. Type 316L-TT

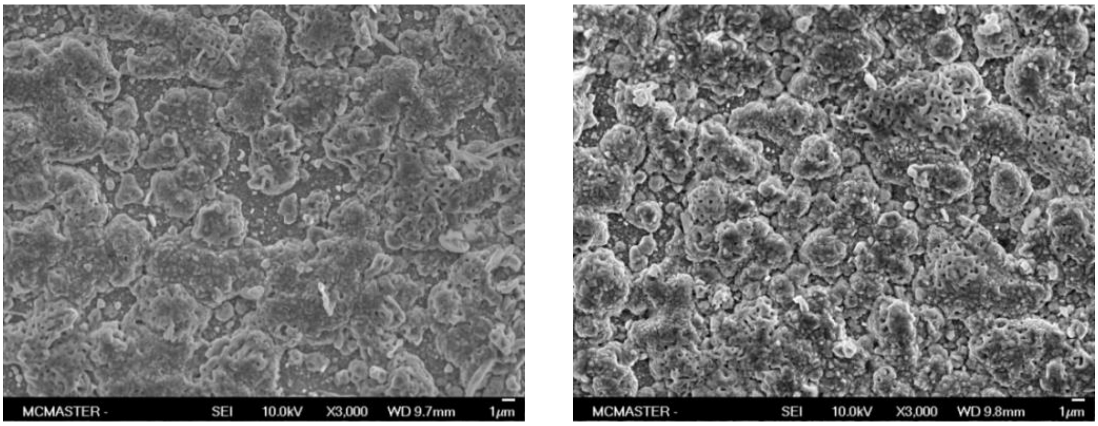
c. Type 310S-SA

d. Type 310S-TT

Figure 4.6 Secondary electron image (plan-view) at higher magnification of the oxide scale morphology formed on the thermally pre-treated material after exposure in SCW

Figure 4.7 shows a backscattered electron image (cross-section) of the oxide scale formed on both Type 316L materials along with an elemental composition profile measured using EDS across the alloy/scale interface. The horizontal line superimposed on each backscattered electron image identifies the location of the EDS line profile, whereas the vertical lines identify the location of the interfaces between distinct phases as deduced from the EDS line profile. The oxide scale formed on both the MA and TT material consisted of three distinct oxidized layers: a Cr-rich inner layer, a Fe-rich middle layer and a mixed Cr-Fe outer layer. The discontinuous morphology of the inner layer was consistent with internal oxidation, whereas the more continuous morphology of the middle layer was consistent with external oxidation. Porosity was observed both at the inner layer/middle layer interface and within the outer layer. The EDS line scan were conducted on representative regions and the average thickness of oxide have no significant difference.

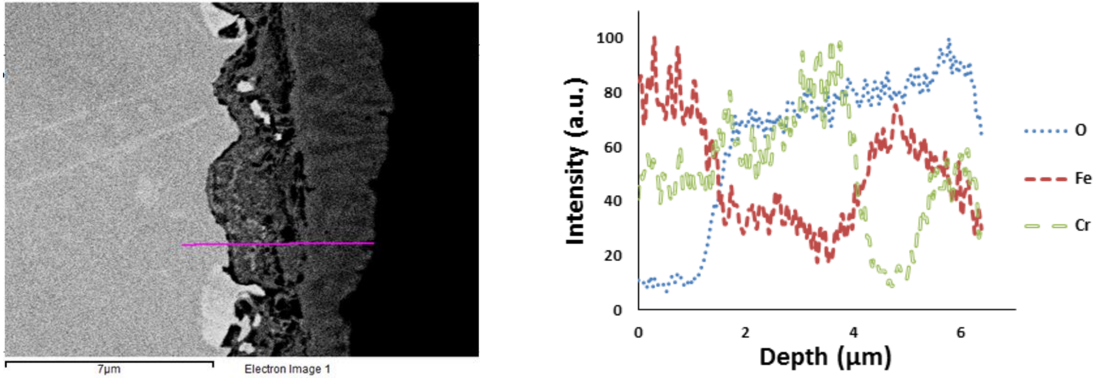
a. Type 316L-MA (BSE Image)

b. Type 316L-MA (EDS)

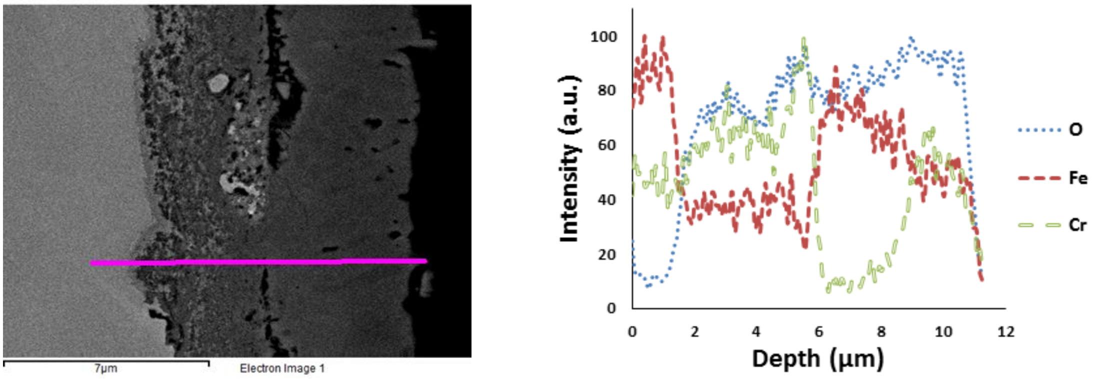
c. Type 316L-TT (BSE Image)

d. Type 316L-TT (EDS)

Figure 4.7 Backscattered electron image (cross-section) and corresponding EDS line analysis of the scale formed on the thermally pre-treated Type 316L material after exposure in SCW

Figure 4.8 shows a backscattered electron image (cross-section) of the oxide scale formed on both Type 310S materials along with an elemental composition profile measured using EDS across the alloy/scale interface. Although two distinct oxidized layers were observed on both materials, they appeared to have a different composition. The oxidized scale on the MA material consisted of a Cr-rich inner layer underneath a Fe-rich outer layer, whereas it consisted of a Cr-rich inner layer underneath a mixed Cr-Fe outer layer on the TT material. The discontinuous morphology of the inner layer was consistent with internal oxidation. Porosity was also observed at the inner layer/outer layer interface, but to a lesser extent than observed on the Type 316L material.

a. Type 310S-MA (BSE Image) b. Type 310S-MA (EDS)

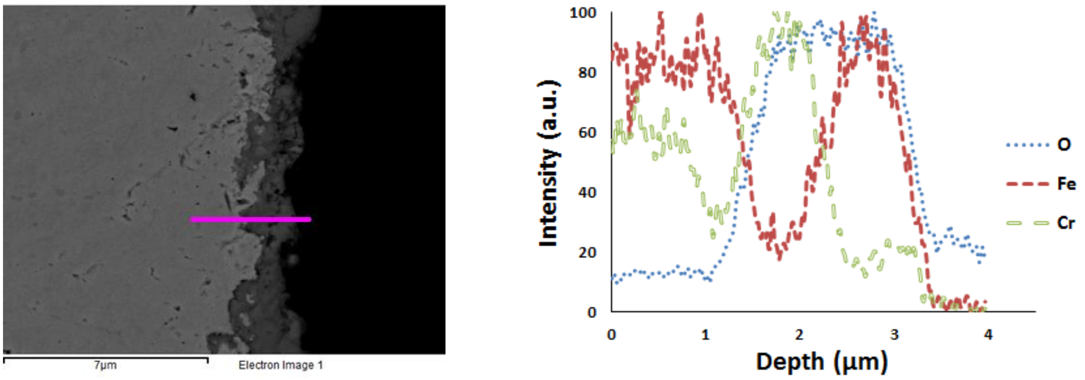

c. Type 310S-TT (BSE Image) d. Type 310S-TT (EDS)

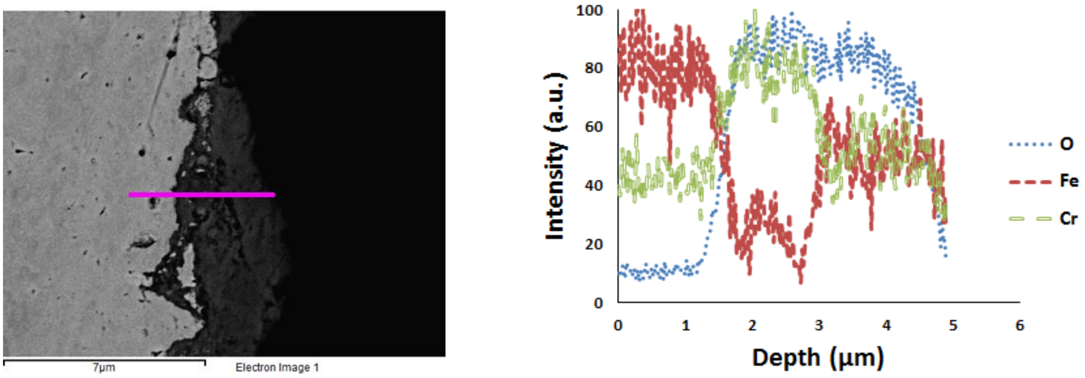

Figure 4.8 Backscattered electron image (cross-section) and corresponding EDS line analysis of the scale formed on the thermally pre-treated Type 310S material after exposure in SCW

4.5 Discussion

The effect of thermal treatment on the corrosion resistance was found to be different for the two stainless steels. The TT material exhibited a statistically higher weight change than the MA material for Type 316L stainless steel, whereas there was no statistically significant difference in the weight changes for the TT and SA Type 310S stainless steel. The difference in the oxide scale thickness was consistent with this finding, being thicker on the TT material than on the MA material for Type 316L, but having similar thicknesses on the TT and SA material for Type 310S. However, as discussed in more detail later, comparing the Type 316L weight change data with published data for a similar exposure suggests that if there was an effect of intermetallic phase precipitates on the apparent (surface area normalized) corrosion resistance, then it was minor at best. The discontinuous network of Cr-binding intermetallic phase precipitates both within the grains and on the grain boundaries is believed to be responsible for the absence of any apparent major effect. The corrosion resistance relies on the formation of a protective oxide scale, which has been reported to be comprised of a combination of a less-protective magnetite (Fe_3O_4) layer residing on top of a more-protective inner Fe-Cr spinel-structure oxide [$(Fe,Cr)_3O_4$] layer for Type 316L stainless steel [18-23] and of a chromia (Cr_2O_3) layer for Type 310 stainless steel [13, 24]. Modifying the near surface grain structure through cold working, as first reported many years ago [25], has a significant beneficial influence on the corrosion resistance of stainless steel in SCW [4, 22, 26]. This is believed to result from enhanced Cr diffusion to the alloy/scale interface along the increased density of grain boundaries and dislocations promoting the formation of a more-protective, continuous inner oxide layer enriched in Cr (relative to that formed on a stress-relieved grain structure). Thus, the formation of intermetallic phase precipitates during thermal treatment has the potential to dramatically affect scale formation in two ways: (i) binding alloyed Cr and (ii) physically blocking diffusion along the short-circuit grain boundary paths. It seems plausible that a detrimental effect can only be realized if there is a continuous network of intermetallic phase precipitates formed on the short-circuit grain boundary diffusion paths. As shown in the set of images presented, this clearly was not the case in the current study. The formation of a continuous network with stainless steel is also unlikely over the in service life of the fuel cladding (about 30,000 h) based on published predictions of intermetallic phase precipitate volume fractions formed in Type 316L stainless steel after prolonged exposure times (up to 100,000 h at 700 ºC) [8]. A parallel study on the effects of Cr-rich precipitates [27], in the TT samples, at the grain boundaries on the SCC susceptibility is being conducted. Although the Cr-rich precipitates did not show significant effects on general corrosion, their effects on SCC could be very different.

The oxide scale formed on both stainless steels exposed in the closed flow loop autoclave exhibited a different structure relative to what has been published in the literature [1, 2, 15]. The major difference is the presence of the Cr rich outer layer: forming a tri-layer oxide scale on Type 316L and a bi-layer oxide scale on Type 310S. The inner layers on both alloys were most likely formed by solid state diffusion [1-5, 17-23, 28], whereas the mixed Cr-Fe oxide outer layer on both alloys was most likely formed by precipitation from a supersaturated SCW layer adjacent to the scale/SCW interface [4, 29]. The combined effect of flow and the constant high dissolved oxygen content likely resulted in the uptake of dissolved metal ions released from the corrosion of upstream loop components in the hot sub-critical water. These loop corrosion products plus those produced by the dissolution of the sparingly soluble oxide corrosion products in SCW [4] produce a supersaturated SCW layer adjacent to the oxide/SCW interface. Both Cr and/or Fe corrosion products have been found to deposit onto/incorporate into the protective oxide formed on metallic coupons exposed in SCW [29]. It is unclear at this time to what extent the precipitation of the mixed Cr-Fe outer layer had on the impeding the oxidation process. Regardless, the effect would have been consistent for each material tested and thus, relative comparisons in weight gain are meaningful.

Figure 4.9 compares weight gain data for Type 316L materials exposed in the closed flow loop autoclave (reported herein) and a static autoclave (reported elsewhere [12]). Also included in the plot is the weight gain value reported by Was et al. [18] for electropolished Type 316L-SA material exposed in deaerated 25 MPa

SCW at 550 °C for 500 h in a closed flow loop autoclave (10-50 mL/min.). Electropolished surfaces have been found to result in reduced corrosion resistance compare to abraded surfaces [4], due to the higher dislocation density in the latter [30]. Two observations were extracted from the comparison presented. First, the average weight gain of the MA and TT material from our testing was higher in the closed flow loop autoclave relative to the static autoclave. However, the apparent increased weight change of the MA material was within the spread of the data set (error bars). Second, the weight gain or our entire set of samples (MA and TT in both autoclave tests) was lower than that reported by Was et al. [18] for SA material. These surface finish effects may account for the slightly higher corrosion resistance observed in the current work compared with the corrosion results reported by Was et al.. Both observations suggest that thermal treatment has a minor second-order effect on the short-term corrosion resistance of stainless steel in SCW. Testing of thermally-aged stainless steel material at both longer exposure times and higher temperature is in progress to validate this initial claim.

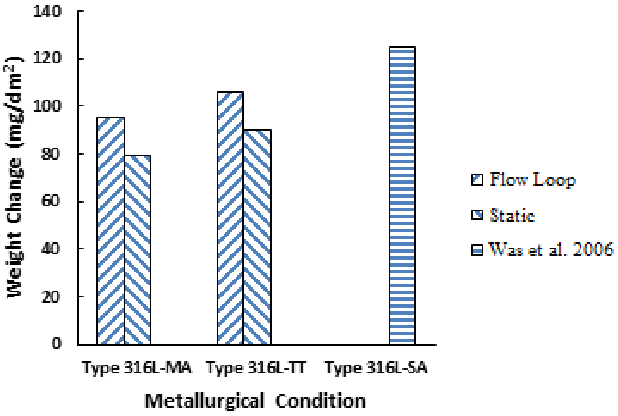

Figure 4.9 Weight change data for Type 316L exposed in 25 MPa SCW at 550 °C for 500 h

4.6 Conclusion

The effect of high temperature microstructure degradation (thermal ageing) on the short-term corrosion resistance of Types 316L and Type 310S austenitic stainless steel exposed in SCW was evaluated in this study. It was concluded that the formation of intermetallic phase precipitates during exposure to high temperatures for prolonged times (thermal ageing) did not have a major effect on the corrosion resistance. The likely reason for this was the discontinuous nature of the precipitates observed within the grains and on the grain boundaries. Of the test parameters under study, alloying was found to have the more pronounced effect on the corrosion resistance than the combined effect of dissolved oxygen and flow. The higher corrosion resistance of 310S, in comparison with 316L, is associated with the presence of a more protective chromia inner layer in the oxide film.

4.7 References

[1] Was, G.S., Ampornrat, P., Gupta, G., Teysseyre, S., West, E.A., Allen, T.R., Sridharan, K., Tan, L., Chen, Y., Ren, X., and Pister, C., 2011, “Corrosion and Stress Corrosion Cracking in Supercritical Water,” J. Nucl. Mater., 371, PP. 176-201.

[2] Kaneda, J., Kasahara, S., Kano, F., Saito, N., Shikama, T., and Matsui, H., 2011, “Material Development for Supercritical Water-Cooled Reactor,” 5th International Symposium on Supercritical Water-Cooled Reactors, Vancouver, BC, Canada, pp. 13-16.

[3] Allen, T.R., Chen, Y., Ren, X., Sridharan, K., Tan, L., Was, G.S., West, E., and Guzonas, D., 2012 “Material Performance in Supercritical Water,” Comprehensive Nuclear Materials: Material Performance and Corrosion/Waste Materials, R.J.M. Konings, ed., Elsevier, Amsterdam, The Netherlands, 5, pp. 279-326.

[4] Guzonas, D.A. and Cook, W.G., 2012, “Cycle Chemistry and its Effect on Materials in a Supercritical Water-Cooled Reactor: A Synthesis of Current Understanding,” Corros. Sci., 65, pp. 48-66.

[5] Penttila, S., Toivonen, A., Rissanen, L., and Heikinheimo, L., 2010, “Generation IV Material Issues – Case SCWR,” J. Disaster Res., 5, pp. 469-477.

[6] Guzonas, D. and Novotny, R., 2014, “Supercritical Water-Cooled Reactor Materials – Summary of Research and Open Issues,” Prog. Nucl. Energy, 77, pp. 361-372.

[7] Mulford, R.A., Hall, E.L. and Briant, C.L., 1983, “Sensitization of Austenitic Stainless Steels □Commercial Purity Alloys,” Corrosion, 39, pp. 132-143.

[8] Tavares, S.S.M., Moura, V., Costa, V.C. da, Ferreira, M.L.R., and Pardal, J.M., 2009, “Microstructural Changes and Corrosion Resistance of AISI 310S Steel Exposed to 600-800 °C,” Mater. Charact., 60, pp. 573-578.

[9] Sourmail, T. and Bhadeshia, H.K.D.H., 2003, “Modelling Simultaneous Precipitation Reactions in Austenitic Stainless Steels,” Calphad, 27, pp. 169-175.

[10] Weiss, B. and Stickler, R., 1972, “Phase Instabilities during High Temperature Exposure of 316 Austenitic Stainless Steel,” Metall. Trans., 3 pp. 851-866.

[11] Spruiell, J.E., Scott, J.A., Ary, C.S., and Hardin, R.L., 1973, “Microstructural Stability of Thermal-Mechanically Pretreated Type 316 Austenitic Stainless Steel,” Metall. Trans., 4, pp. 1533-1544.

[12] Lai, J.K.L., 1983, “A Review of Precipitation Behavior in AISI Type 316 Stainless Steel,” Mater. Sci. Eng., 58, pp. 195-209.

[13] Sourmail, T., 2001, “Precipitation in Creep Resistant Austenitic Stainless Steels,” Mater. Sci. Technol., 17, pp. 1-14.

[14] Mahboubi, S., Botton, G.A., and Kish, J.R., 2014, “Oxide Scales Formed on Austenitic Fe-Cr-Ni Alloys Exposed to Supercritical Water (SCW): Role of Alloying Elements,” 19th Pacific Basin Nuclear Conference, Vancouver, BC, Canada, Paper No. 286.

[15] Li, J., Zheng, W., Penttilä, S., Liu, P., Woo, O.T., and Guzonas, D., 2014, “Microstructure Stability of Candidate Stainless Steels for Gen- IV SCWR Fuel Cladding Application,” J. Nucl. Mater., 454, pp. 7-11.

[16] Jiao, Y., Kish, J., Zheng, W., Guzonas, D., and Cook, W., 2014, “Effect of Thermal Ageing on the Corrosion Resistance of Stainless Steel Type 316L Exposed in Supercritical Water,” Canada-China Conference on Advanced Reactor Development, Niagara Falls, ON, Canada, Paper No. 27.

[17] Kriaa, C A., Hamdi, N., and Sidhom, H., 2008, “Assessment of Intergranular Corrosion of Heat Treated Austenitic Stainless Steel (AISI 316L Grade) by Electron Microscopy and Electrochemical Tests," Prot. Met., 44, pp. 506-513.

[18] White, W.E., and May, I. Le, 1970, “Metallographic Observations on the Formation and Occurrence of Ferrite, Sigma Phase, and Carbides in Austenitic Stainless Steels: Part I: Studies of AISI Type 310 Stainless Steel,” Metallography, 3, pp. 35-50.

[19] Was, G.S., Teysseyre, S., and Jiao, Z., 2006, “Corrosion of Austenitic Alloys in Supercritical Water,” Corrosion, 62, pp. 989-1005.

[20] Gao, X., Wu, X., Zhang, Z., Guan, H., and Han, E.H., 2007, “Characterization of Oxide Films Grown on 316L Stainless Steel Exposed to H2O2-Containing Supercritical Water,” J. Supercrit. Fluids, 42, pp. 157-163.

[21] Luo, X., Tang, R., Long, C., Miao, Z., Peng, Q., and Li, C., 2008, “Corrosion Behavior of Austenitic and Ferritic Steels in Supercritical Water,” Nucl. Eng. Technol., 40, pp. 147-154.

[22] Sun, M., Wu, X., Zhang, Z., and Han, E.H., 2009, “Progress in Corrosion Resistant Materials for Supercritical Water Reactors,” Corros. Sci., 51, pp. 1069-1072.

[23] Fulger, M., Mihalache, M., Ohai, D., Fulger, S., and Valeca, S.C., 2011, “Analyses of Oxide Films Grown on AISI 304L Stainless Steel and Incoloy 800HT Exposed to Supercritical Water Environment,” J. Nucl. Mater., 415, pp. 147-157.

[24] Svishchev, I.M., Carvajal-Ortiz, R.A., Choudhry, K.I., and Guzonas, D.A., “Corrosion Behavior of Stainless Steel 316 in Sub- and Supercritical Aqueous Environments: Effect of LiOH Additions, Corros. Sci., 72, pp. 20-25.

[25] Sun, M., Wu, X., Han, E.H., and Rao, J., 2009, “Microstructural Characteristics of Oxide Scales Grown on Stainless Steel Exposed to Supercritical Water,” Scripta Mater., 61, pp. 996-999.

[26] Penttilä, S., Toivonen, A., Li, J., Zheng, W., and Novotny, R., 2013, “Effect of Surface Modification on the Corrosion Resistance of Austenitic Stainless Steel 316L in Supercritical Water Conditions,” J. Supercrit. Fluids, 81, pp. 157-163.

[27] Abe, H., Hong, S.M., and Watanabe, Y., 2014, “Oxidation Behavior of Austenitic Stainless Steels as Fuel Cladding Candidate Materials for SCWR in Superheated Steam,” Nucl. Eng. Design, 280, pp. 652–660.

[28] Ruther, W.E., Schlueter, R.R., Lee, R.H., and Hart, R.K., 1966, "Corrosion Behavior of Steels and Nickel Alloys in Superheated Steam, Corrosion, 22, pp. 147-155.

[29] Tsuchiya, Y., Kano, F., Saito, N., Ookawa, M., Kaneda, J., and Hara, N., 2007, "Corrosion and SCC Properties of Fine Grain Stainless Steel in Subcritical and Supercritical Pure Water," Corrosion/07, NACE International, Houston, TX, Paper No. 07415.

[30] Daigo, Y., Watanabe Y., and Sue. K., 2007, "Effect of Chromium Ion from Autoclave Material on Corrosion Behavior of Nickel-Based Alloys in Supercritical Water," Corrosion, 63, pp. 277-284.

[31] Persuad, S.Y., Korinek, A., Huang, J., Botton, G.A., and Newman, R.C., 2014, "Internal Oxidation of Alloy 600 Exposed to Hydrogenated Steam and the Beneficial Effects of Thermal Treatment," Corros. Sci., 86, pp. 108-122.

[32] Maekawa,T., Kagawa, M., and Nakajima, N., 1968, "Corrosion Behaviors of Stainless Steel in High-Temperature Water and Superheated Steam," Trans. Jpn. I. Met., 9, pp. 130-136.

5. Effect of Thermal Ageing on the Intergranular Stress Corrosion Cracking Susceptibility of Type 310S Stainless Steel

Y. Jiao, J. Mahmood, W. Zheng, P. Singh and J. Kish. Effect of thermal ageing on the intergranular stress corrosion cracking susceptibility of Type 310S stainless steel, accepted for publication in Corrosion, November 2017.

5.1 Introduction

This chapter reproduces a submitted article, which documents the research conducted to isolate and assess the intergranular SCC susceptibility of the two limiting thermally-aged Type 310S stainless steel conditions relative to the baseline in terms of the contributing chemical factors only (degree of grain boundary sensitization in particular). This article is the first of three that, as a set, specifically address the SCC implications of both short-term and long-term thermally-aged microstructures in SCW described in Section 1.2 above and in the Stress Corrosion Cracking Implications Section in Chapter 3. The relative intergranular SCC susceptibility of the thermally-aged materials was evaluated in terms of the degree of sensitization (chemical factor) determined using the double loop electrochemical potentiokinetic reactivation (DL-EPR) technique and validated through slow strain rate testing (SSRT) technique using a pressurized hot alkaline solution. The latter solution is known to promote intergranular SCC in stainless steel that is driven predominantly by chemical factors (preferential anodic dissolution of the Cr-depleted zones).

Prof. Kish at McMaster University and Prof. Zheng at CanmetMATERIALS are my supervisors. They were giving me guidance, instruction and edit manuscript. Prof. Singh at Georgia Institute of Technology is our collaborator and gave us suggestions and comments for SSRT tests. Mr. Mahmood was a student of Prof. Singh and conducted the SSRT tests for us. I was responsible for conceiving the research questions, collecting and analyzing the data, and writing the manuscripts. The study was approved by the McMaster Research Ethics Board at McMaster University (Hamilton, Ontario).

5.2 SCC Susceptibility Consideration

Type 310S (UNS S31008) austenitic stainless steels has been short-listed as a candidate for the fuel cladding in the Canadian supercritical water-cooled reactor (SCWR) design concept currently being developed as part of the Generation IV International Forum (GIF) initiative [1-4]. The predicted in-service environment for the Canadian SCWR includes a range of supercritical water (SCW) coolant temperatures (350-625 °C), high pressure (25 MPa) and dose of neutron irradiation (up 9.5 dpa) [3,4]. The effect of microstructure instability of the fuel cladding resulting from exposure to both high temperature and radiation on the stress corrosion cracking resistance (SCC) is of particular concern considering the collapsible design, dynamic exposure conditions and expected in-service life (~30,000 h) of the fuel cladding [1,3].

The effect of microstructure instability on the SCC susceptibility of stainless steels exposed in SCW has been considered [5-8]. Pre-exposure to high temperature proton irradiation (to simulate neutron radiation damage at the surface) was found by slow strain rate testing (SSRT) to significantly increase the intergranular SCC (IGSCC) susceptibility of Types 304L (UNS S30403) and 316L (UNS S31603) stainless steel relative to the non-irradiated material in de-oxygenated (< 10 ppb) 25 MPa SCW over the temperature range of 400 °C to 550 °C, regardless of the radiation dose or temperature [6,7]. The increased IGSCC susceptibility of the proton irradiated material correlated with both an increased hardening and degree of radiation induced segregation (RIS), which included Cr-depleted zone formation adjacent to grain boundaries. In contrast, SSRT of sensitized Type 304L stainless steel (thermally-aged to form Cr-rich $M_{23}C_6$ particles on the grain boundaries and associated adjacent Cr-depleted zones) revealed an upper limit temperature for IGSCC susceptibility of 400 °C, above which IGSCC did not occur in oxygenated (8 ppm) 25 MPa SCW [5]. Even without the complicating effects of microstructure instability (either thermally-induced or radiation-induced), extracting general conclusions about the in-service SCC susceptibility of stainless steels exposed in SCW is difficult given the variation in testing conditions (temperature, pressure, strain rate and SCW chemistry) [9-11]. For example, some degree of IGSCC susceptibility of mill-annealed Types

304L and 316L stainless steel was found by SSRT in de-oxygenated (< 10 ppb) 25 MPa SCW over the temperature range from 400 °C to 550 °C, with Type 304L stainless steel being more susceptible than Type 316L stainless steel [12]. Yet in other reports, only a transgranular SCC (TGSCC) was found by SSRT for Types 316L [13] and 316Ti (UNS 31635) [14] stainless steels in 25 MPa SCW with controlled oxygen levels over a temperature range from 380 °C to 650 °C. Regarding Type 310S stainless steel specifically, a recent study has revealed an IGSCC susceptibility after long term (20,000 h) capsule testing in de-oxygenated 25 MPa SCW at 500 °C [8], which indicates that a comprised grain boundary regions can develop after prolonged exposure to high temperature.

The predicted temperature range (375 °C-800 °C) of the fuel cladding in the Canadian SCWR concept is expected to promote the formation of precipitates on the grain boundaries and within the grains of Type 310S stainless steel [15-17] if selected as the preferred material of construction. Carbides ($M_{23}C_6$-type) and sigma (σ) phase precipitates are expected to form after exposure at high temperatures [18-21]. Formation of carbide ($M_{23}C_6$) precipitates on grain boundaries can be accompanied adjacent Cr-depleted zone formation [20,21] and possibly C-enriched zone formation [21], depending on exposure time and temperature, serving to 'sensitize' the microstructure by increasing the intergranular corrosion susceptibility. The phase precipitates are brittle and significantly harder relative to the austenite matrix phase

[22,23]. The formation of σ phase precipitates on grain boundaries can be accompanied by Cr-depleted zone formation, depending on exposure time and temperature, serving to sensitize the microstructure by increasing the intergranular corrosion susceptibility [20,24].

The correlation between increased IGSCC susceptibility and both increased hardness and degree of RIS [6,7] raises an important question about which grain boundary factor, chemical (i.e., sensitization) or mechanical (embrittlement) controls the IGSCC process. While it is understood that the contribution of each factor, and possible interactions between them, can be complex, a “first approximation” attempt to isolate and assess the potential contribution of each factor to the IGSCC susceptibility in SCW is warranted. The purpose of this study was to isolate and assess the relative potential contribution of the chemical (sensitization) factor to IGSCC susceptibility of thermally-aged Type 310S stainless steel in support of developing the SCWR concept. A similar study conducted to isolate and assess the relative potential contribution of the mechanical (embrittlement factor) to IGSCC susceptibility will be reported in a future publication. Samples were thermally-aged to two limiting extents and compared relative to a solution-annealed condition, which represented an ideal starting microstructure baseline. The limiting extents consisted of a short-term thermal aging treatment to sensitize the microstructure by forming Cr-rich $M_{23}C_6$ precipitates on the grain boundaries and adjacent Cr-depleted zones and a long-term thermal ageing treatment to embrittle the microstructure by forming σ phase precipitates on the grain boundaries. The degree of sensitization was evaluated using the double loop electrochemical potentiokinetic reactivation (DL-EPR) technique and the associated IGSCC susceptibility was evaluated using SSRT in a hot alkaline solution known the cause IGSCC in stainless steels with the chemical (sensitization) factor controlling relative susceptibility [25,26].

5.3 Experimental

5.3.1 Materials

Test samples were prepared from commercial Type 310S stainless steel rod product (25.6 mm diameter) provided in the mill-annealed (MA) condition. The chemical composition as specified in the Mill Test Report is listed in Table 1. Sub-sections of the rod product were solution-annealed (SA), sensitized (S) or thermally-treated (TT) prior to preparing test samples. The SA treatment was conducted at 1050 °C for 1 h, followed by water-quenching to yield an ideal microstructure that would exhibit a low degree of sensitization (formation of Cr-depleted zones adjacent to grain boundaries). The S treatment was conducted at 650 °C for 100 h, followed by air-cooling to yield a classic sensitized microstructure with significant $M_{23}C_6$ carbide precipitation on the grain boundaries concomitant with the adjacent Cr-depleted zone formation [18-21]. This treatment was intended to represent a short-term exposure of the fuel cladding in service sufficient to sensitize the microstructure. The TT treatment was conducted at 800 °C for 1000 h, followed by air-cooling to yield a degraded microstructure with significant σ phase precipitation on the grain boundaries and within the grains [18-21]. This treatment was intended to represent a long-term exposure of the fuel cladding at the maximum cladding temperature expected in the Canadian SCWR design concept (800 °C) [1]. All rod sub-sections were sealed in a nitrogen-purged quartz tube during the heat treatments to prevent excessive oxidation.

Table 5.1 Chemical composition (wt.%) of the Type 310S rod.

Cr	Ni	Mo	Mn	Si	P	S	C	Fe
24.3	19.56	0.29	0.96	0.76	0.004	0.004	0.06	Bal.

5.3.2 Microstructure Characterization

The microstructure of the SA, S and TT material was examined in cross-section using scanning electron microscopy (SEM), and transmission electron microscopy (TEM); both of which coupled with X-ray energy dispersive spectroscopy (EDS). Samples for SEM examination were prepared from the heat-treated rod sub-sections and cold-mounted in epoxy with the plane parallel to the longitudinal axis of the rod product exposed for examination. Surfaces were mechanically-abraded and polished to a 1 μm finish using standard metallographic techniques. Chemical etching was conducted by contacting the polished surfaces with an acetic acid-glycerine mixture for 40 s. SEM imaging was performed using a JEOL JSM-7000F microscope equipped with a Schottky Field Emission Gun (FEG) filament and an integrated

Oxford Synergy system with INCA EDS X-ray micro-analysis. Images were acquired using an accelerating voltage of 10 kV and a working distance of 10 mm.

The TEM examination was performed using JEOL 2010F TEM/STEM equipped with an Oxford Instruments EDS analyser. Images and elemental line scans were acquired using an accelerating voltage of 200 kV with a point-to-point resolution of 0.23 nm. Thin foils were prepared by mechanically abrading samples from the SA, S and TT material to a thickness of 80 µm using SiC paper and water as the lubricant. A small section was then punched out of each mechanically-abraded sample and subsequently electrochemically polished in a perchlorate acid (10%)-methanol (90%) solution at −50ºC to create a small hole.

Randomly selected grain boundary precipitates were identified by comparing the elemental atomic composition ratios determined using EDS (both spot analyses and line scans) in both SEM and scanning TEM (STEM) mode with those elemental atomic composition ratios published in the literature using the same techniques [19,27-29]. Given the inaccuracies associated with the larger working volume in combination with relatively small grain boundary particles, only the STEM-EDS line scan results are reported herein to confirm the intended precipitates were formed in each case. For reproducibility purposes, six such line scans were acquired across grain boundaries in the SA material, sixteen such line scans in the S material and four line scans in the TT material. Selected area diffraction (SAD) patterns in TEM mode were acquired from grain boundary precipitates (three precipitates in each of the SA, S and TT material) and from the unaffected matrix (two sites in each of the SA, S and TT material). Acquired SAD patterns were compared to those of expected precipitate phases ($M_{23}C_6$ and σ phase) that were created using the JEMS software [30] and published reference diffraction patterns [31].

5.3.3 Degree of Sensitization Assessment

The degree of sensitization of the SA, S and TT material was evaluated by both the width of the Cr depletion zone (less than 13 wt.% Cr) across the grain boundary [32-34] and the double loop potentiokinetic reactivation (DL-EPR) test method. The width of Cr depletion zones across grain boundaries were determined using the STEM-EDS line scans. For the DL-EPR testing, a set of triplicate cubic samples were prepared from the SA, S and TT material and cold-mounted in epoxy with the plane parallel to the longitudinal axis of the rod product exposed as the working surface (about 1 cm^2). Working surfaces were mechanically-abraded to a 600 grit finish using SiC paper and water as lubricant, rinsed with acetone and dried in air prior to immersion. Electrical contact was made by attaching an insulated Cu wire to the buried face opposite to the working surface using adhesive tape prior to cold mounting The test solution was 2 M H_2SO_4 + 0.01 M KSCN, which was prepared using reagent grade chemicals and distilled water. A standard three electrode electrochemical cell was used to make the DL-EPR measurements at room temperature using a graphite rod as the counter electrode and a saturated calomel electrode (SCE) as the reference electrode. The open-circuit potential (OCP) was recorded for 5-minute period prior to initiating the DL-EPR measurement. Then the applied potential was swept in the forward (anodic) direction at a 1 mV/s rate until a value of +0.3 VSCE was obtained, after which the applied potential was swept in reverse (cathodic) direction until the starting OCP value was attained. The degree of sensitization is defined by the current density ratio i_r/i_a, where i_a is the activation peak current density measured during the forward (anodic) scan and i_r is the reactivation peak current density measured during the reverse (cathodic) scan. One sample from each set was selected for plan-view and cross-sectional view imaging of the corroded surface using SEM. Cross-sections were prepared in the manner described above.

5.3.4 IGSCC Susceptibility Assessment by SSRT

SSRT samples were machined from SA, S and TT material with the longitudinal axis oriented along the longitudinal direction of the rod product. The gauge length of each cylindrical sample was 25.4 mm (1 inch) and the gauge diameter was 3.175 mm (0.125 inches). Figure 5.1 shows a dimensioned drawing of a typical sample. The gauge length was mechanically-abraded to a 1000 grit finish using SiC paper and water as a lubricant. The final finish was applied along the longitudinal direction. The samples were then rinsed with distilled water, ultrasonically rinsed in acetone and allowed to dry prior to each test. All tests were conducted at an initial strain rate of 1 ×

10^{-6} /s. Duplicate samples of each heat-treated material were tested in a 3.75 M NaOH + 0.64 M Na_2S ("white liquor") at 170°C and a third sample of each was tested in dry sand heated to 170 °C. The test solution was prepared from reagent-grade chemicals. All tests were carried out in an autoclave equipped with a rigid slow strain rate rig. The samples were mounted in a fixture using ceramic washers to prevent galvanic effects with the autoclave. All of the tests were carried out at the OCP. Each sample was pre-loaded to 15 kg to minimize system compliance (reduction gear, grips, etc.). The load was measured with a load cell, and the % elongation was calculated based on the displacement rate of the crosshead times the duration of each test. One half of the fractured SSRT samples was cold-mounted in cross-section, mechanically-abraded and polished using standard metallographic procedures and examined using light optical microscopy. The other half of the fractured SSRT samples was used for fractography, in which the fracture surfaces were rinsed in acetone, air-dried and imaged using SEM (JEOL JSM-7000F microscope).

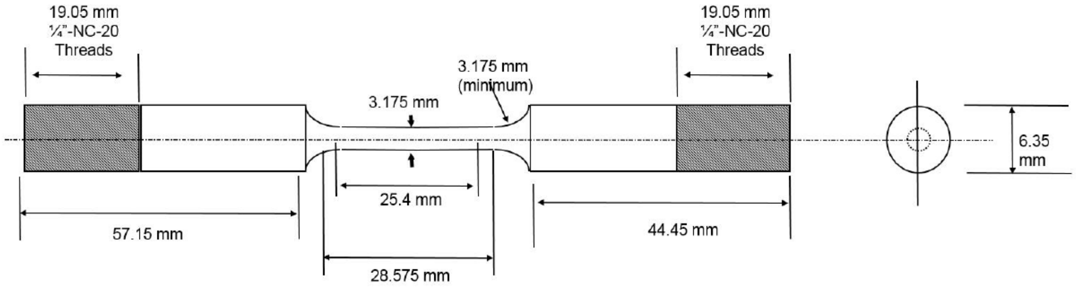

Figure 5.1 Drawing of the cylindrical SSRT samples.

5.4 Results

5.4.1 Microstructure Characterization

Figure 5.2 shows SEM images of the etched SA, S and TT material in cross-section (at both low and high magnification). Precipitates decorated the grain boundaries of all three materials. The extent of this decoration was lower in the SA material than in either the S or TT material. Precipitates were also observed with the matrix of the S and TT material. The matrix precipitates in the S material were smaller than those formed in the TT material. All three materials had a similar average grain size number (linear intercept method of ASTM E1382): 7.2 for the SA material, 7.5 for S material and 7.0 for TT material. The image of the S material (Figure 5.2b) shows a clustering of small grains. This is not typical of the general microstructure, which is similar to that shown in the image of the SA material (Figure 5.2a), but was included for illustrative purposes to show the extent of grain boundary precipitation. Although not reported herein, SEM-EDS analysis identified all grain boundary precipitates examined in each material as being enriched in Cr relative to the unaffected matrix.

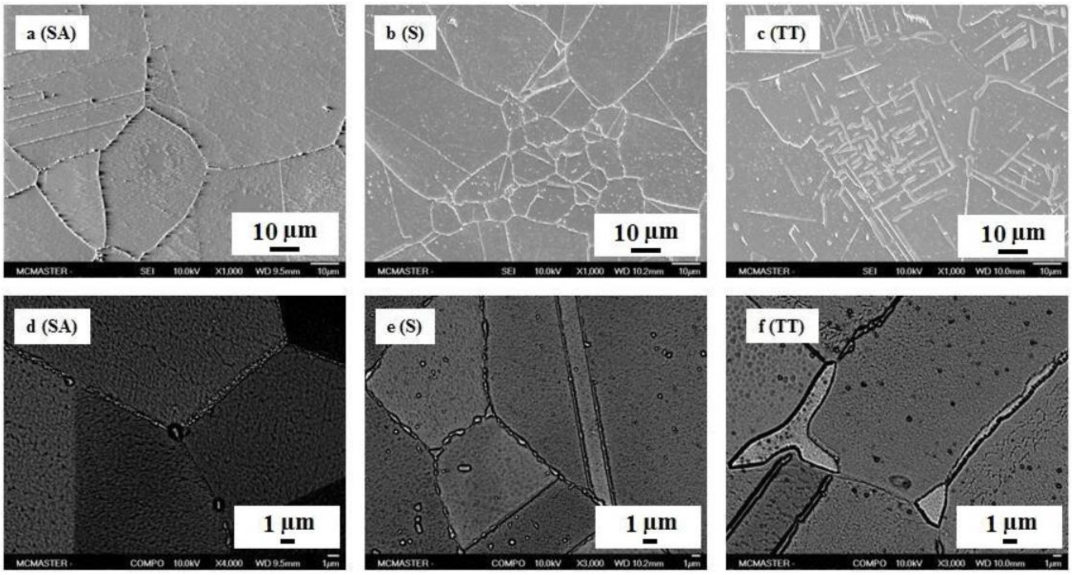

Figure 5.2 Secondary electron image showing the typical appearance of the heat-treated microstructure: (a) SA material, (b) S material and (c) TT material. Higher magnification back scattered images showing typical appearance of the heat-treated microstructure: (d) SA material, (e) S material and (f) TT material.

A set of TEM images focussing on the grain boundary region in each material are shown in Figure 5.3 along with the set of associated STEM-EDS sum spectra for the for the grain boundary precipitates (relative to the unaffected matrix) identified on each image. The grain boundary precipitates in both the SA and S material were enriched in Cr and C and depleted in Ni and Fe relative to matrix. The grain boundary precipitates in the TT material were enriched in just Cr and depleted Ni and Fe relative to the matrix. The similarity between the enrichment/depletion of the major alloying elements within the grain boundary precipitates relative to the unaffected matrix as identified by the STEM-EDS differential sum spectra agrees well the elemental atomic composition ratio data for thermally-induced precipitates in stainless steel published in the literature using the same technique [19,27-29].

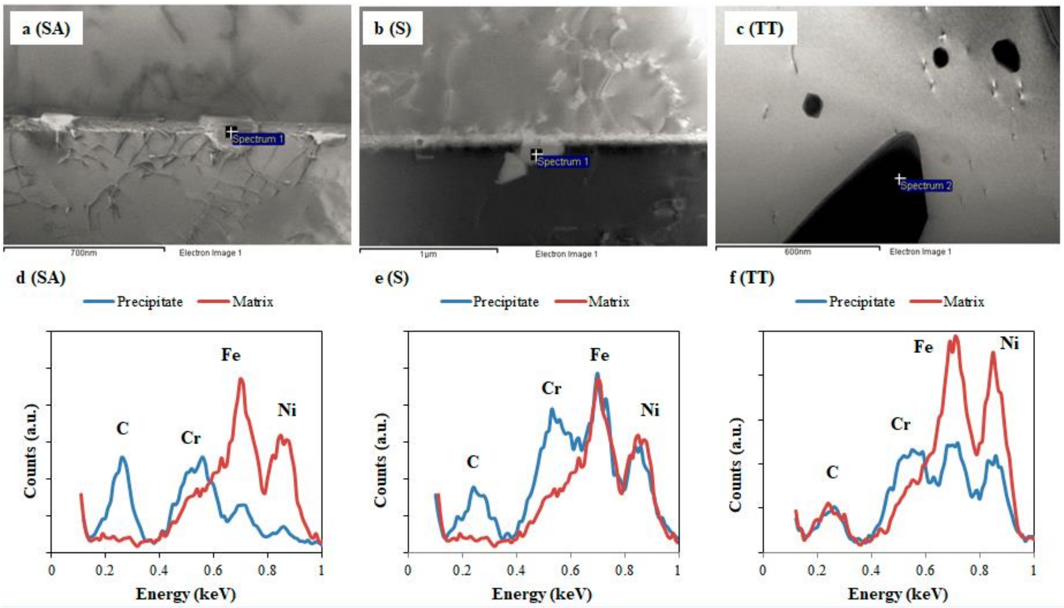

Figure 5.3 Backscattered electron image showing the appearance of the grain boundary precipitates of the heat-treated microstructure selected for spot EDS analysis: (a) SA material, (b) S material and (c) TT material. EDS analysis of grain boundary precipitate relative to matrix: (d) SA material, (e) S material and (f) TT material.

The identity of the grain boundaries precipitates was further analysed using SAD. All three SAD patterns acquired from the grain boundary precipitates in the SA and S material were indexed as Cr-rich $M_{23}C_6$. An example of an SAD pattern acquired from a grain boundary precipitate in the SA and S material is shown in Figure 5.4a and 5.4b respectively. In contrast, all three SAD patterns acquired from grain boundary precipitates in the TT material were indexed as σ phase. An example of such a pattern is shown in Figure 5.4c. $M_{23}C_6$ precipitates were identified in TT material, but only within the austenite matrix phase along with σ phase precipitates.

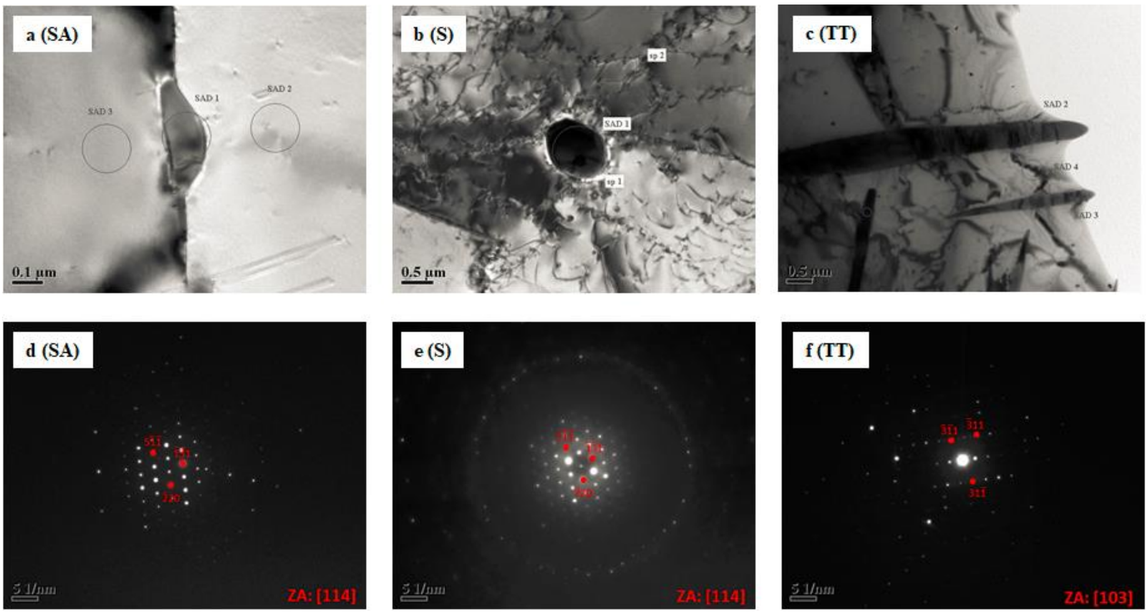

Figure 5.4 Bright field electron image showing the appearance of the grain boundary precipitate of the heat-treated microstructure selected for spot EDS analysis: (a) SA material, (b) S material and (c) TT material. EDS analysis of grain boundary precipitate relative to matrix: (d) SA material, (e) S material and (f) TT material.

5.4.2 Degree of Sensitization Assessment

Figure 5.5 shows a superimposed set of STEM-EDS line scans conducted across grain boundary precipitates in the SA, S and TT material. All three Cr concentration profiles plotted show a significant enrichment within the grain boundary precipitate itself relative to the matrix. A Cr-depleted zone in the matrix associated with this significant enrichment in the grain boundary precipitate was observed only in the S material. Thus, the degree of sensitization based on the width of Cr-depletion zone across grain boundaries only applied to the S material, for which the corresponding value was 136 ± 18 nm. This width is consistent with that reported in for Type 310S stainless steel reported in the literature [20]. The absence of a Cr-depleted zone accompanying the σ phase grain boundary precipitates in the TT material indicates that the treatment time of a 1000 h was sufficient to "self-heal" the Cr-depleted zone, which was expected to have formed during the early stages of the treatment at 800 °C [20]. Self-healing in this case likely occurs by recovery of Cr within the depleted zone by back diffusion of Cr with increased thermal aging time.

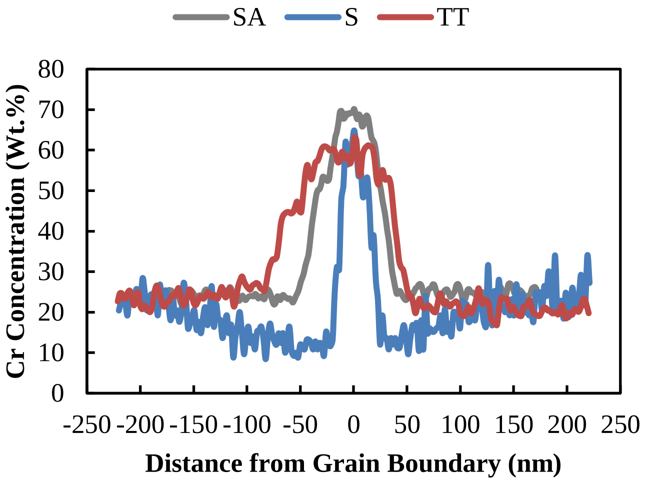

Figure 5.5 Plot comparing the Cr concentration across grain boundary region in each of the three heat-treated materials, as measured using TEM-EDS line scans.

Figure 5.6 shows a typical DL-EPR response measured for each material. The arrows represent the scanning directions. It is evident that the S material (Figure 5.6b) exhibited a significantly larger anodic peak during the reverse scan than either the SA (Figure 5.6a) or TT (Figure 5.6c) material. Both the SA and TT material exhibited polarity reversals (cathodic loops) in the reverse scan, which indicates that passive films formed on those materials are sufficiently protective to reduce the anodic kinetics to a value lower than the prevailing cathode kinetics at potentials while the passive film remains stable [35]. The associated set of i_r/i_a, ratios is compared in Figure 5.6d. The error bars demark the highest and lowest value recorded for each set of four samples; indicating the spread in the data. The magnitude of i_r/i_a, ratios shows that the S material was significantly more sensitized than either the SA or TT material. Interesting, the TT material exhibited a larger i_r/i_a ratio than the SA material, indicating that anodic dissolution in the TT material occurred to a greater extent. It is possible that the appreciable cathodic kinetics (as revealed by the cathodic loop in the SA and TT material curves) may have counterbalanced the anodic kinetics observed ($i_{total} = i_a - i_c$) in the reactivation loop to some extent, thereby under predicting the i_r value. However, the post exposure plan view and cross-sectional images show no evidence in support of intergranular corrosion, consistent with the low i_r/i_a ratio for SA and TT material.

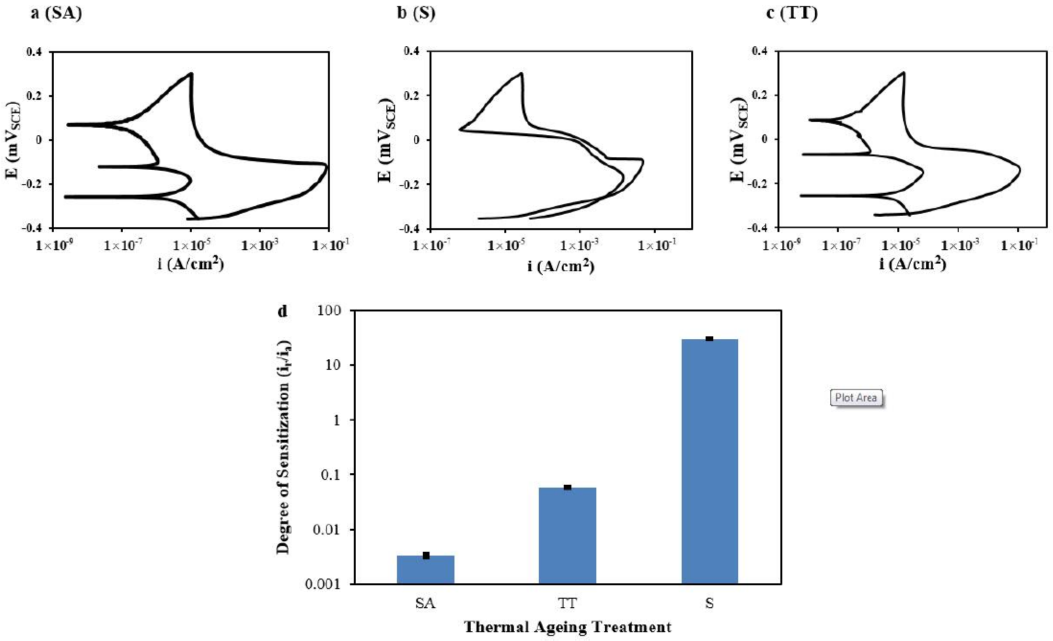

Figure 5.6 Typical DL-EPR measurement of the (a) SA material, (b) S material and (c) TT material. (d) Plot comparing the degree of sensitization, as measured using the corresponding ir/ia ratio.

Plan view and cross-sectional view images of the cyclic polarized surfaces are shown in Figure 5.7. The SA material surface revealed a slight etching of the grain boundaries in plan view (Figure 5.7a). The attack was incipient as it was not well-developed when viewed in cross-section (Figure 5.7d). Significant attack of the grain boundaries was evident in both views of the S material surface (Figure 5.7b and 5.7e). The TT material surface revealed a distinctly different morphology, with the matrix selectively dissolved (in low relief) around the presumably intact grain boundary precipitates (in high relief). The cross-sectional view (Figure 7f) confirmed this as it revealed a discontinuous surface region: consisting of matrix the matrix selectively dissolved (in low relief) around the presumably intact grain boundary precipitates (in high relief).

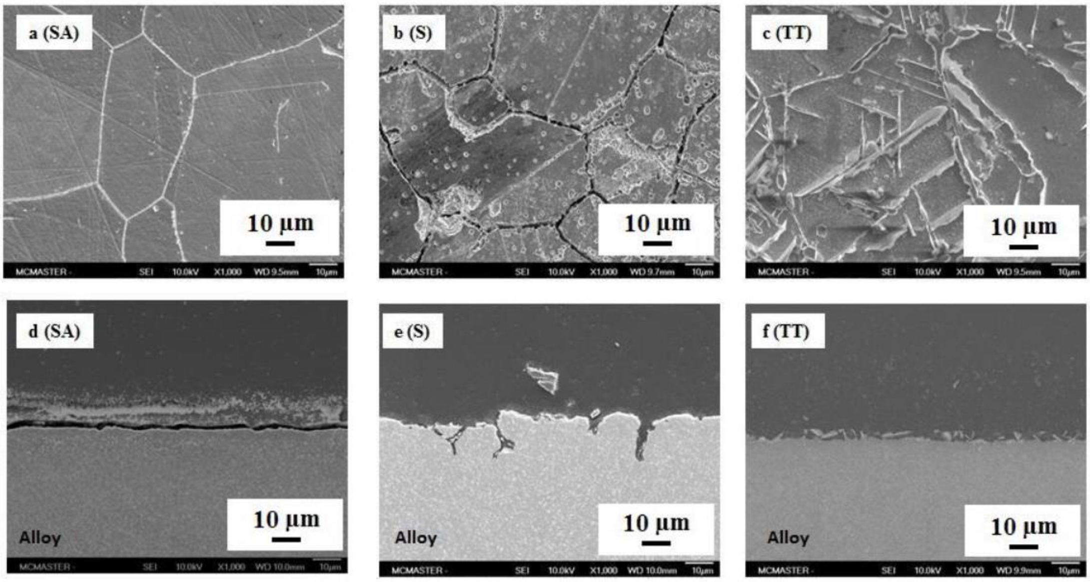

Figure 5.7 Secondary electron image of the post-polarized surface of in plan view: (a) SA material, (b) S material and (c) TT material. Corresponding view in cross-section: (d) SA material, (e) S material and (f) TT material.

5.4.3 IGSCC Susceptibility Assessment by SSRT

Figure 5.8 shows the stress-strain curve of the SA, SA and TT material measured in both the hot alkaline solution and hot dry sand (baseline). Each material exhibited a distinctly different response in the hot alkaline solution relative to the hot dry sand baseline. The SA material exhibited a similar yield stress and ultimate tensile stress, but a distinctly lower fracture strain when tested in the hot alkaline solution relative to the hot dry sand baseline. In stark contrast, the S material exhibited a distinct reduction in the yield strength, ultimate tensile strength and fracture strain when tested in the hot alkaline solution relative to the hot dry sand baseline. The TT material exhibited a similar yield stress and ultimate tensile stress, but a distinctly higher fracture strain when tested in the hot alkaline solution relative to the hot dry sand baseline. A duplicate set of SSRT measurements in the hot alkaline solution yielded a similar response relative to the hot dry sand for each material. The elastic portions of these curves did not match perfectly due to test-to-test differences in the initial slack in the load-displacement inside the autoclave.

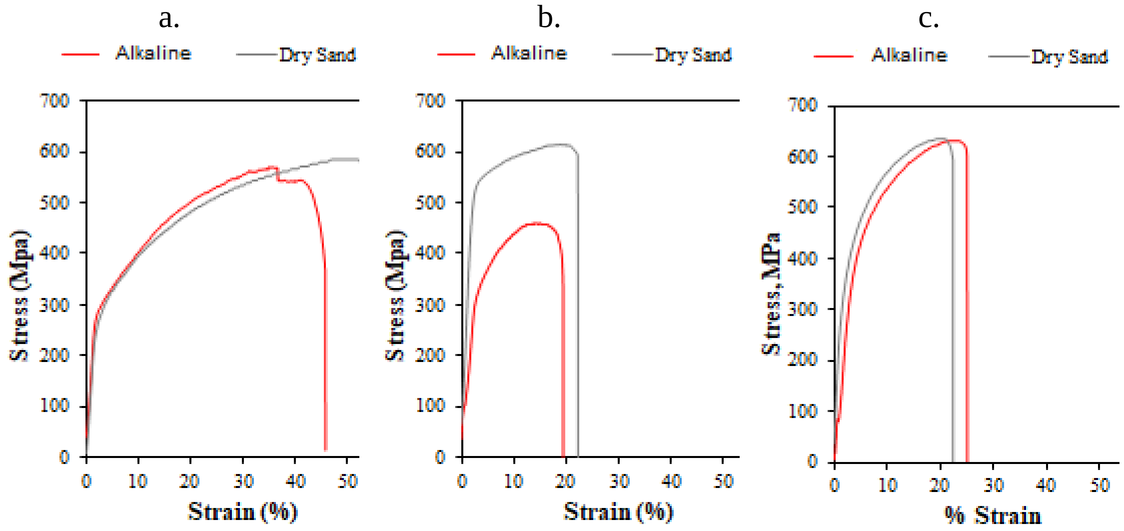

Figure 5.8 Engineering stress-strain plot of heat-treated SSRT samples measured in hot alkaline solution relative to hot dry sand: (a) SA material, (b) S material and (c) TT material.

It is clear from the stress-strain curves presented in Figure 5.8 that both thermal ageing treatments applied significantly embrittlled (based on fracture strain) Type 310S stainless steel relative to SA (baseline) condition. It is also clear from the stress-strain curves presented in Figure 5.8b for the S material that there is a significant SCC susceptibility in the hot alkaline solution (depending on the heat treatment applied). Keeping in line with the purpose of this study, the analysis of the SSRT data is restricted to relative potential contribution chemical (sensitization) has on the IGSCC susceptibility of thermally-aged Type 310S stainless steel. An analysis of the effect thermal ageing has on the mechanical properties and the potential contribution of grain boundary embrittlement on the IGSCC susceptibility of thermally-aged Type 310S stainless steel will be reported in a future publication.

Low magnification SEM images of the SSRT sample shanks and associated fracture surfaces after exposure in the hot alkaline solution are shown in Figure 5.9. Significant secondary crack-like indications were found on the shanks of the S (Figure 5.9b) and TT material (Figure 5.9c). Similar indications were not observed on the shanks of the S and TT material SSRT samples exposed in the hot dry sand baseline when imaged at a similar magnification. The SA material shank (Figure 5.10a) revealed significant localized deformation (necking) occurred prior to the onset of fracture. Secondary crack-like indications were not observed on this shank. The fracture surfaces of the SA and S material exhibited a variable morphology, consisting of an outer ring (edge) region surrounding a central core region, whereas the fracture surface of the TT material exhibited a uniform morphology over the entire area. Higher magnification SEM images of the edge and centre regions of the fracture surfaces are shown in Figure 5.10. Despite showing a variable morphology, the fracture mode of the SA and S material was distinctly different: transgranular fracture for the SA material and intergranular fracture for the S material. Both the edge (Figure 5.10a) and centre region (Figure 5.10a) of the SA material exhibited classic ductile tearing features via void (primary and secondary) growth and coalescence. Both the edge (Figure 5.10b) and centre (Figure 5.10e) regions of the S material exhibited classic intergranular fracture features. However, the centre region exhibited some evidence of secondary micro-voids at the opening of grain boundaries and occasional cleavage facets. The dominant cracking mode of the TT material was also transgranular, but significantly more mixed-mode (cleavage + ductile tearing) than the SA material, with both the edge (Figure 5.10c) and centre (Figure 5.10f) regions exhibiting similar morphology.

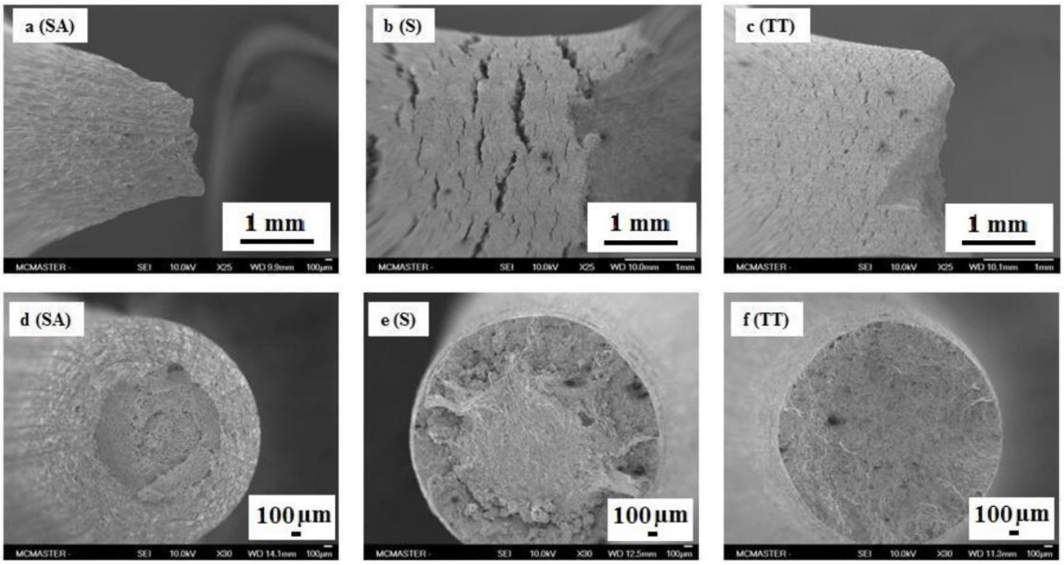

Figure 5.9 Secondary electron images showing the typical appearance of the fractured SSRT sample shank in plan view: (a) SA material, (b) S material and (c) TT material. Corresponding image of the fracture surface: (d) SA material, (e) S material and (f) TT material.

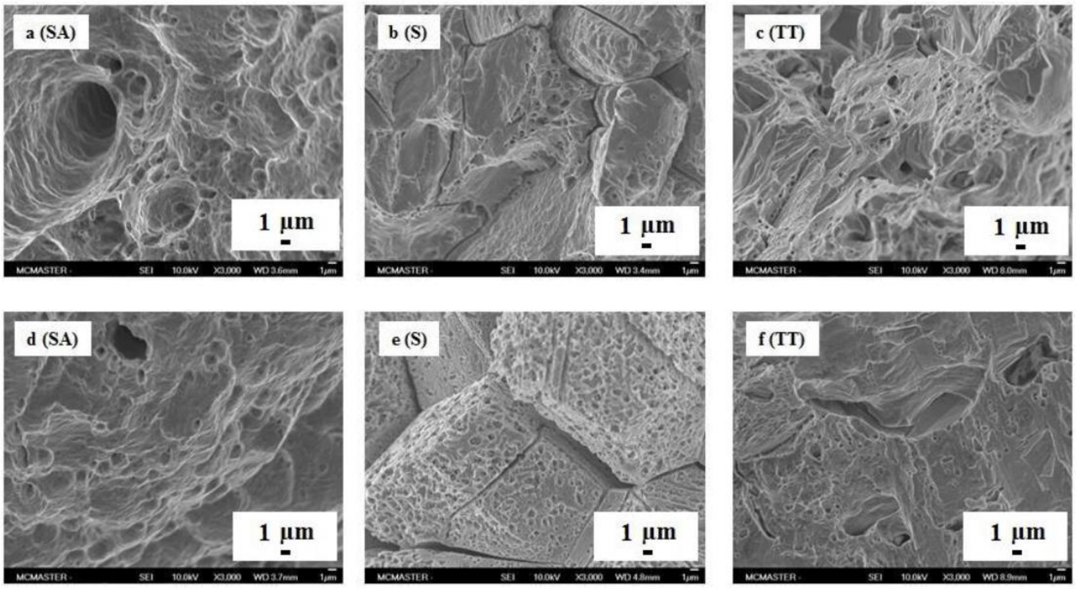

Figure 5.10 Secondary electron images showing the typical appearance of the fracture surface edge region: (a) SA material, (b) S material and (c) TT material. Corresponding image of the fracture surface centre region: (d) SA material, (e) S material and (f) TT material.

A set of SEM images showing the SSRT sample shanks (immersed in the hot alkaline solution) in cross-section are shown in Figure 5.11. A few well-developed secondary cracks were readily observed in the S material shank (Figure 5.11b). A higher magnification image of one of these secondary cracks (Figure 5.11e) shows the intergranular nature. A relatively high number of crack-like indications were observed on the TT material shank (Figure 5.11c). A higher magnification image of one such indication (Figure 5.11f) shows incipient grain boundary cracking through a fractured σ phase particle located at the surface. In contrast, no secondary crack-like indications were observed on the SA material shank (Figure 5.11a and 5.11e).

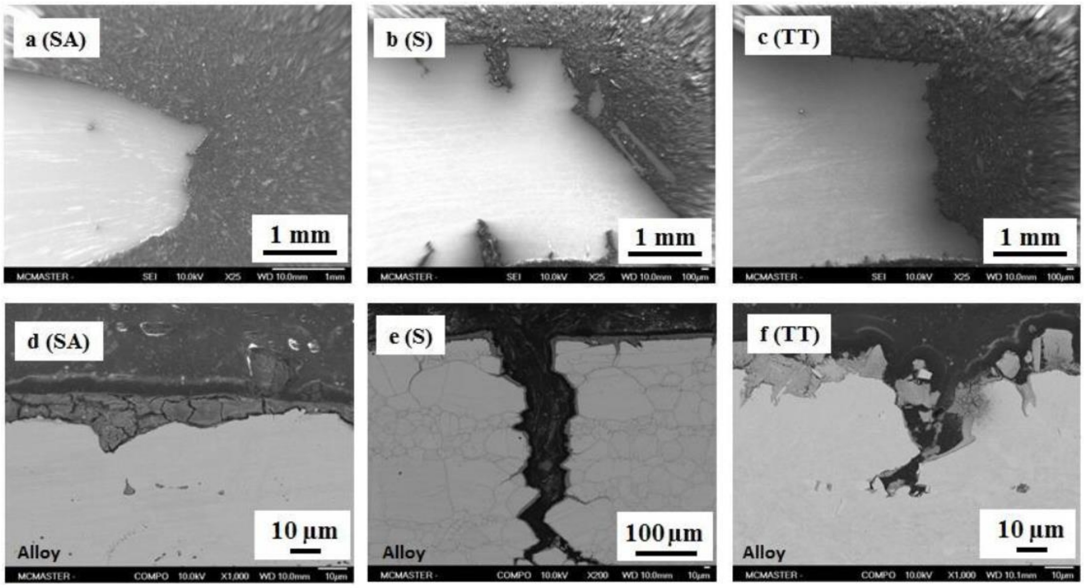

Figure 5.11 Secondary electron images showing the typical appearance of the fractured SSRT sample shank in cross-sectional view: (a) SA material, (b) S material and (c) TT material. Corresponding image of the fracture surface: (d) SA material, (e) S material and (f) TT material.

The SCC information extracted from the SSRT tests is summarized in Table 5.2, which lists the results for the duplicate testing conducted in the hot alkaline solution and the singular testing conducted in the hot dry sand. The SSRT ratio was determined using both true strain value at fracture (alkaline solution/dry sand) and the % reduction in area (% RA) value at fracture (alkaline solution/dry sand). The % RA value at fracture was determined by comparing the change in cross-sectional area at fracture relative to the original cross-sectional area. The SCC susceptibility was determined from the plan view and cross-sectional imaging of the fractured samples. Overall, the S material was significantly more susceptible to SCC (IGSCC in this case) than either the SA (TGSCC) or TT material (no SCC). The SSRT results of the duplicate TT samples exposed in the hot alkaline solution are very similar in terms of both the true strain values and % RA values at fracture. The true strain values at fracture are higher than the value recorded during exposure in hot dry sand, whereas the % RA values are lower. Despite these differences, the curves presented in Figure 5.8c are similar enough to indicate essentially no SCC susceptibility of the TT material as evaluated by SSRT. The post exposure metallographic examination is consistent with this interpretation as no significant difference in fracture mode between the edge and centre region of the fracture surface was observed. The SSRT results of the duplicate SA samples exposed in the hot alkaline solution are also very similar in terms of from both the true strain values and % RA values at fracture. Although the true strain values at fracture are lower than the value recorded during exposure in hot dry sand, the % RA values are higher – the reverse of the TT material case. The curves presented in Figure 5.8a are dissimilar enough to indicate a mild SCC susceptibility as evaluated by SSRT. Here too, the post exposure metallographic examination is consistent with this interpretation as a significant difference in fracture mode between the edge and centre region of the fracture surface was observed.

Table 5.2 SCC data for the heat-treated Type 310S material in the hot alkaline solution.

Material	Solution	SCC Susceptibility	Fracture True Strain	SSRT Ratio	% RA	SSRT Ratio
SA	Dry Sand	No SCC	0.44	---	68	---
	Alkaline	TGSCC	0.38	0.86	71	1.04
	Alkaline	TGSCC	0.42	0.95	71	1.04
S	Dry Sand	No SCC	0.20	---	62	---
	Alkaline	IGSCC	0.17	0.85	9	0.14
	Alkaline	IGSCC	0.18	0.90	14	0.22
TT	Dry Sand	No SCC	0.20	---	25	---
	Alkaline	No SCC	0.21	1.05	18	0.72
	Alkaline	No SCC	0.22	1.10	19	0.76

5.5 Discussion

Table 5.3 summarizes the major type of microstructure instabilities that were confirmed by STEM-EDS and TEM-SAD. Both thermal ageing treatments were successful in producing the intended microstructure instability: Cr-rich $M_{23}C_6$ precipitate formation on the grain boundaries with development of adjacent Cr-depleted zones in the S material and phase precipitate formation on the grain boundaries and within the grains in the TT material. Cr-rich $M_{23}C_6$ grain boundary precipitates were also observed in the SA material, albeit to a significantly reduced extent relative to the S material. They were present without the adjacent Cr-depleted zones. It is unclear if the $M_{23}C_6$ grain boundary precipitates in the SA material were pre-existing and simply not dissolved during the heat treatment or were formed during water quenching as these meta-stable precipitates are always found in the early stages of precipitation because they nucleate very easily [19]. Regardless, this finding is considered inconsequential since the SA material exhibited a low degree of sensitization and low susceptibility to IGSCC (in hot alkaline solution), as originally anticipated for comparative purposes.

Table 5.3 Microstructure instability observed in heat-treated Type 310S material by electron microscopy.

Material	Grain	Cr-Depleted Zone	Grain Boundary
SA	Not Detected	No	$M_{23}C_6$
S	$M_{23}C_6$	Yes	$M_{23}C_6$
TT	$M_{23}C_6$ + σ Phase	No	σ Phase

The degree of sensitization was assessed in two ways: using the i_r/i_a ratio from DL-EPR testing and the width of the Cr-depleted zone from STEM-EDS line scans. A high degree of correlation is well known to exist between these two metrics [32]. Figure 5.12 plots the width of the Cr-depleted zone against the i_r/i_a ratio of the three heat-treated materials tested. Superimposed onto the plot is the generally accepted transition between a sensitized and a non-sensitized microstructure [36]. The S material was the only one of the three that was sensitized according to this material parameter space. There is no differentiation between the non-sensitized SA and TT material on the Cr-depleted zone width scale, yet there is differentiation between the two on the i_r/i_a ratio scale: TT material ratio being larger than the SA material ratio. The post-polarized surface of the TT material revealed the σ phase in high relief (Figure 5.7f). This observation is consistent with results of DL-EPR testing of σ-phase containing stainless steels reported in the literature [24,37-38]. The proposed explanation involves the formation of a more protective oxide film on the σ phase particles relative to the adjacent matrix during the passivation process at higher applied potentials due to the much higher Cr content of the σ phase particles. The matrix adjacent to the σ phase particles preferentially dissolves despite the absence of adjacent Cr-depleted zones development during thermal treatment [37,38]. The protective oxide film prevents the σ phase particles from being dissolved to the solution during the reactivation process [37]. The higher ratio of the TT material (relative to the SA material) in the research reported herein suggests that the matrix was dissolved to a larger extent the reverse scan.

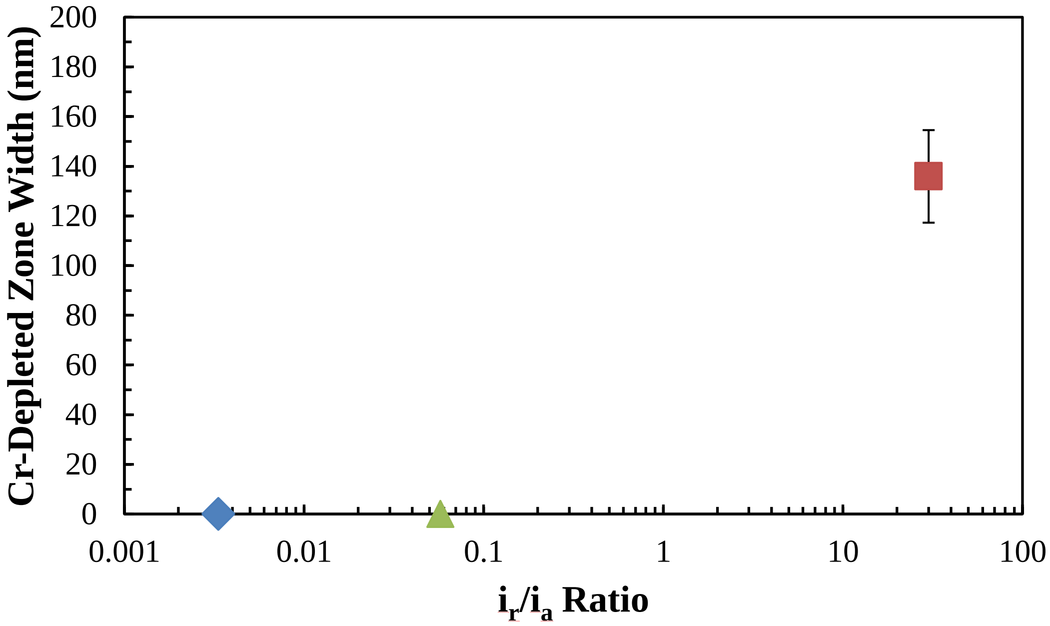

Figure 5.12 Plot of Cr-depleted zone (measured using TEM-EDS) versus the degree of sensitization (measured using ir/ia ratio).

SSRT tests were conducted in a hot alkaline solution to evaluate the effect of the limiting thermal ageing cases under study on the IGSCC susceptibility of Type 310S stainless steel, the S material was only one of the three heat-treated materials that was sensitized (as shown in Figure 5.13) that exhibited IGSCC in the hot alkaline solution. It is generally accepted that, in the absence of irradiation damage, the Cr-depleted zones are the dominant factor that controls IGSCC when the cracking process is electrochemical in nature largely due to a reduced thermodynamic stability region for protective oxide film formation and increased anodic dissolution kinetics [33,34,39]. SCC of stainless steels in hot alkaline solutions is presumed to be electrochemical in nature since anodic protection can mitigate the susceptibility [26]. Cr-depleted zones selectively dissolve in hot NaOH solutions promoting the formation of a brittle Fe-Ni-enriched oxide [40-42]. It is expected that the presence of Na_2S in addition to NaOH in the hot alkaline solution used for the SSRT herein served to further exacerbate this tendency. The addition of Na_2S to hot NaOH solutions significantly alter the electrochemical behavior of stainless steel by destabilizing the oxide film via sulfide-compound incorporation, which reduces the polarization resistance and, thus increases anodic dissolution kinetics [43,44]. The effect is akin to the effect adsorbed sulphur has on the anodic dissolution process of Fe, Ni and Cr elucidated by Marcus et al. [45]. The combined effect serves to increase the SCC susceptibility of stainless steels in Na_2S-NaOH solutions relative NaOH solutions [25,41,46,47].

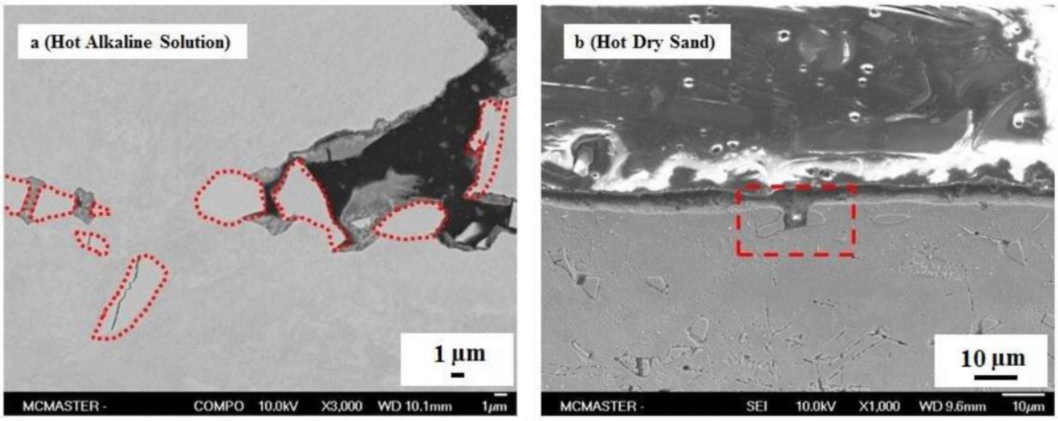

Figure 5.13 (a) Backscattered electron image of a cracked intergranular σ phase particle located at the surface of the TT material after SSRT conducted in the hot alkaline solution (fractured σ phase grain boundary particles outlined with hatched line). (b) Secondary electron image of a cracked σ phase particle located at the surface of the TT material after SSRT conducted in the hot dry sand.

SEM examination of the fractured S material SSRT sample in cross-section revealed that the crack surfaces were covered with a relatively thick film. This film was also observed on selected grain boundaries adjacent to crack indications that were preferentially attacked. These finding suggest that a tarnish/brittle film rupture mechanism [48,49] is likely responsible for the IGSCC exhibited by the S material. Preferential corrosion would initiate on the surface of a Cr-depleted zone and propagate through the zone resulting in the formation of a brittle mixed oxide-sulphide film. Under an applied stress, the brittle film would then fracture once it reaches a critical depth. The ensuring crack would enter into the substrate serving to expose bare metal for further anodic dissolution and brittle film formation. This process would repeat itself leading to discontinuous crack propagation.

The secondary crack-like indications found on the shank surface of the TT samples exposed in the hot alkaline solution is also consistent with the brittle film rupture mechanism, despite the material not exhibiting well-developed IGSCC or having well-developed Cr-depleted zones adjacent to the grain boundaries. The larger brittle σ phase particles decorating the grain boundaries were clearly preferentially cracked under the externally applied stress (Figure 5.12f). This finding is consistent with σ phase embrittlement of Type 310 stainless steel [50]. We believe such preferential cracking, when located at the surface, could have served as an alternative site to Cr-depleted zones for SCC to initiate at grain boundaries. The proposed mechanism would involve the following rudimentary steps. The relatively large brittle σ phase particles located on the grain boundary at the surface would crack first under the applied stress (brittle fracture) serving to expose bare metal at the crack tips to the hot alkaline solution. However, as there are no Cr-depleted zones in the TT material, the austenite matrix itself would be directly exposed to the hot alkaline solution at the crack tips. The austenite matrix, presumably without any significant Cr depletion, would anodically dissolve slower than the Cr-depleted zones in S material in the hot alkaline solution leading to a more protective and less brittle film Cr-enriched oxide formation, akin to the protective film formation on the SA material. Slower anodic dissolution and less brittle film formation in combination with the relatively large crack volume would serve to limit the extent of further crack propagation. Figure 5.12a shows an SEM image of an incipient crack indication located at surface of the TT material shank: the features of which being consistent with this cracking mechanism. Preferential attack of the grain boundary region is clearly evident along with the formation of a relatively thick film that is partially cracked. Thus, the hot alkaline solution serves to accentuate the mechanically-induced σ phase cracking by corroding the freshly exposed austenite matrix to a limited extent. It follows then that similar mechanically-induced σ phase cracking should also have occurred at the shank surface of the TT samples exposed in the hot dry sand. This is in fact the case as shown in the secondary electron image in Figure 5.12b.

The findings will be utilized to contrast an IGSCC susceptibility map that help predict problematic microstructure instabilities arising from exposure to both high temperature and radiation during service. The envisioned map plots an appropriate chemical factor (such as the degree of sensitization measured by the DL-EPR method) against an appropriate mechanical factor (such as degree of grain boundary embrittlement) for various degraded microstructures including, but not limited to, thermal ageing. The map will also help to identify the controlling chemical (grain boundary sensitization) and/or mechanical (grain boundary embrittlement) factor that control the process through similar SSRT of specific degraded material (such as S and TT material as studied herein) in SCW. Such knowledge is essential to any attempt at identifying and testing possible microstructure ‘stablization’ strategies necessary to mitigate the risk associated with this damage mode in SCW. Thus, if the chemical factor is indeed controlling of the IGSCC process in SCW, then the risk for IGSCC would greater during short-term exposures (S material) than at longer term exposures (TT material) when considering thermal aging effects alone.

5.6 Conclusions

The purpose of this study was to isolate and assess the relative potential contribution of a sensitized microstructure to the IGSCC susceptibility of thermally-aged Type 310S stainless steel in support of developing the SCWR concept. The following conclusions were drawn:

1. Both limiting thermal ageing treatments were successful in producing the intended microstructure instability expected of a Type 310S stainless steel fuel cladding in service: Cr-rich $M_{23}C_6$ precipitate formation on the grain boundaries in the S material (short-term sensitizing exposure) and relatively large σ phase precipitate formation on the grain boundaries in the TT material (long-term embritlling exposure). TEM-EDS analysis revealed the presence of a well-developed Cr-depleted zone in the S material and the absence of such a zone in the TT material.

2. The overall ranking in terms of an increasing degree of sensitization, as determined by DL-EPR testing, of three heat treatments studied is: SA ~ TT << S. The ranking reflects the controlling role played by Cr-depleted zones, which were

only observed in the S material. The absence of a Cr-depleted zone accompanying the σ phase grain boundary precipitates in the TT material indicates that the treatment time of a 1000 h was sufficient to "self-heal" the Cr-depleted zone, which was expected to have formed during the early stages of the treatment at 800 °C.

3. SSRT conducted in a hot alkaline solution readily showed an IGSCC susceptibility of the S material, consistent with the associated sensitized microstructure (exhibiting a well-developed Cr-depleted zone formation adjacent to grain boundaries). The relatively large σ phase grain boundary particles in the TT material preferentially cracked during SSRT in both the hot dry sand and hot alkaline solution indicating that the preferential cracking was controlled by mechanical factors only. The absence of well-developed Cr-depleted zone formation adjacent to grain boundaries prevented IGSCC from developing in the hot alkaline solution. Bulk fracture of this material occurred via a transgranular mixed-mode process.

5.7 References:

[1] D. Guzonas, R. Novotny, Supercritical water-cooled reactor materials – Summary of research and open issues, Progress in Nuclear Energy, 77 (2014) 361-372.

[2] J. Li, Materials Selection for the Canadian Supercritical Water-Cooled Nuclear Reactor Concept, JOM, 68 (2016) 452-453.

[3] D. Guzonas, M. Edwards, W. Zheng, Assessment of candidate fuel cladding alloys for the Canadian supercritical water-cooled reactor concept, Journal of Nuclear Engineering and Radiation Science, 2 (2016) 011016.

[4] W. Zheng, D. Guzonas, K.P. Boyle, J. Li, S. Xu, Materials Assessment for the Canadian SCWR Core Concept, JOM, 68 (2016) 456-462.

[5] Y. Tsuchiya, F. Kano, N. Saito, A. Shioiri, S. Kasahara, K. Moriya, H. Takahashi, SCC and irradiation properties of metals under supercritical-water cooled power reactor conditions, GENES4/ANP2003, Kyoto, Japan, Paper, 1096 (2003) 15-19.

[6] S. Teysseyre, Z. Jiao, E. West, G. Was, Effect of irradiation on stress corrosion cracking in supercritical water, Journal of Nuclear Materials, 371 (2007) 107-117.

[7] R. Zhou, E.A. West, Z. Jiao, G.S. Was, Irradiation-assisted stress corrosion cracking of austenitic alloys in supercritical water, Journal of Nuclear Materials, 395 (2009) 11-22.

[8] Y. Behnamian, A. Mostafaei, A. Kohandehghan, B.S. Amirkhiz, J. Li, R. Zahiri, E. Aghaie, W. Zheng, D. Guzonas, M. Chmielus, Internal oxidation and crack susceptibility of alloy 310S stainless steel after long term exposure to supercritical water at 500° C, The Journal of Supercritical Fluids, 120 (2017) 161-172.

[9] G.S. Was, S. Teysseyre, Challenges and recent progress in corrosion and stress corosion cracking of alloys for supercritical water reactor core components, in: 12th International Conference on Environmental Degradation of Materials in Nuclear

Power Systems-Water Reactors, August 14, 2005 - August 18, 2005, Minerals, Metals and Materials Society, Salt Lake City, UT, United states, 2005, pp. 1343-1357.

[10] W. Zheng, J. Luo, M. Li, D. Guzonas, W. Cook, Stress corrosion cracking of SCWR candidate alloys: A review of published results, in: The 5th International Symposium on Supercritical-Water-Cooled Reactors (ISSCWR-5), Vancouver, BC, Canada, March, 2011, pp. 13-16.

[11] X. Ru, R.W. Staehle, Historical experience providing bases for predicting corrosion and stress corrosion in emerging supercritical water nuclear technology: Part 1 - Review, Corrosion, 69 (2013) 211-229.

[12] S. Teysseyre, G.S. Was, Stress corrosion cracking of austenitic alloys in supercritical water, Corrosion, 62 (2006) 1100-1116.

[13] R. Novotny, P. Hahner, J. Siegl, P. Hausild, S. Ripplinger, S. Penttila, A. Toivonen, Stress corrosion cracking susceptibility of austenitic stainless steels in supercritical water conditions, Journal of Nuclear Materials, 409 (2011) 117-123.

[14] Z. Shen, L. Zhang, R. Tang, Q. Zhang, SCC susceptibility of type 316Ti stainless steel in supercritical water, Journal of Nuclear Materials, 458 (2015) 206-215.

[15] J. Li, W. Zheng, S. Penttilä, P. Liu, O.T. Woo, D. Guzonas, Microstructure stability of candidate stainless steels for Gen-IV SCWR fuel cladding application, Journal of Nuclear Materials, 454 (2014) 7-11.

[16] Y. Jiao, J.R. Kish, G. Steeves, W.G. Cook, W. Zheng, D.A. Guzonas, Effect of Thermal Pretreatment on the Corrosion of Stainless Steel in Flowing Supercritical Water, Journal of Nuclear Engineering and Radiation Science, 2 (2016) 011015.

[17] Y. Jiao, W. Zheng, D. Guzonas, J. Kish, Microstructure Instability of Candidate Fuel Cladding Alloys: Corrosion and Stress Corrosion Cracking Implications, JOM, 68 (2016) 485-489.

[18] W. White, I. Le May, Metallographic observations on the formation and occurrence of ferrite, sigma phase, and carbides in austenitic stainless steels: Part I: Studies of AISI Type 310 Stainless Steel, Metallography, 3 (1970) 35-50.

[19] T. Sourmail, Precipitation in creep resistant austenitic stainless steels, Materials science and technology, 17 (2001) 1-14.

[20] S.S.M. Tavares, V. Moura, V.C. da Costa, M.L.R. Ferreira, J.M. Pardal, Microstructural changes and corrosion resistance of AISI 310S steel exposed to 600-800C, Materials Characterization, 60 (2009) 573-578.

[21] J. Qian, C. Chen, H. Yu, F. Liu, H. Yang, Z. Zhang, The influence and the mechanism of the precipitate/austenite interfacial C-enrichment on the intergranular corrosion sensitivity in 310S stainless steel, Corrosion Science, 111 (2016) 352-361.

[22] E. Hall, S. Algie, The sigma phase, Metallurgical reviews, (2013).

[23] T. Ohmura, K. Tsuzaki, K. Sawada, K. Kimura, Inhomogeneous nano-mechanical properties in the multi-phase microstructure of long-term aged type 316 stainless steel, Journal of Materials research, 21 (2006) 1229-1236.

[24] J.K. Shin, H.J. Jang, K.W. Cho, C.J. Park, Effects of sigma and chi phases on the localized corrosion resistance of SR50A super austenitic stainless steel, Corrosion, 69 (2013) 364-371.

[25] K.R. Chasse, S. Raji, P.M. Singh, Effect of Chloride Ions on Corrosion and Stress Corrosion Cracking of Duplex Stainless Steels in Hot Alkaline-Sulfide Solutions, Corrosion, 68 (2012) 932-949.

[26] P. Pohjanne, M. Vepsäläinen, T. Saario, K. Sipilä, J. Romu, T. Saukkonen, H. Hänninen, M. Heikkilä, J. Koskiniemi, C.-G. Berg, Effect of Electrochemical Potential on Stress Corrosion Cracking Susceptibility of EN 1.4301 (AISI 304) Austenitic Stainless Steels in Simulated Hot Black Liquor, Corrosion, 71 (2015) 887-894.

[27] B. Weiss, R. Stickler, Phase instabilities during high temperature exposure of 316 austenitic stainless steel, Metallurgical Transactions, 3 (1972) 851-866.

[28] J. Spruiell, J. Scott, C. Ary, R. Hardin, Microstructural stability of thermal-mechanically pretreated type 316 austenitic stainless steel, Metallurgical transactions, 4 (1973) 1533-1544.

[29] J. Lai, A review of precipitation behaviour in AISI type 316 stainless steel, Materials Science and Engineering, 61 (1983) 101-109.

[30] J. software, http://cimewww.epfl.ch/people/stadelmann/jemswebsite/jems.html

[31] F. Karlsruhe, FIZ Startseite - FIZ Karlsruhe, in.

[32] S. Bruemmer, L. Chariot, B. Arey, Sensitization development in austenitic stainless steel: Correlation between STEM-EDS and EPR measurements, Corrosion, 44 (1988) 328-333.

[33] S. Bruemmer, Quantitative modeling of sensitization development in austenitic stainless steel, Corrosion, 46 (1990) 698-709.

[34] S.M. Bruemmer, G.S. Was, Microstructural and microchemical mechanisms controlling intergranular stress corrosion cracking in light-water-reactor systems, Journal of Nuclear Materials, 216 (1994) 348-363.

[35] R. Kelly, Electrochemical thermodynamics and kinetics of relevance to corrosion, Corrosion Technology-NEW YORK and BASEL-, 18 (2003) 9-54.

[36] A.P. Majidi, M.A. Streicher, The double loop reactivation method for detecting sensitization in AISI 304 stainless steels, Corrosion, 40 (1984) 584-593.

[37] N. Lopez, M. Cid, M. Puiggali, Influence of o-phase on mechanical properties and corrosion resistance of duplex stainless steels, Corrosion Science, 41 (1999) 1615-1631.

[38] K. Lo, C. Kwok, W. Chan, Characterisation of duplex stainless steel subjected to long-term annealing in the sigma phase formation temperature range by the DLEPR test, Corrosion Science, 53 (2011) 3697-3703.

[39] G. Cragnolino, D. Macdonald, Intergranular stress corrosion cracking of austenitic stainless steel at temperatures below 100 C—a review, Corrosion, 38 (1982) 406-424.

[40] M. Yasuda, K. Fukumoto, H. Koizumi, Y. Ogata, F. Hine, On the Active Dissolution of Metals and Alloys in Hot Concentrated Caustic Soda, Corrosion, 43 (1987) 492-498.

[41] P.M. Singh, O. Ige, J. Mahmood, Stress corrosion cracking of type 304L stainless steel in sodium sulfide-containing caustic solutions, Corrosion, 59 (2003) 843-850.

[42] J. Deakin, D. Zehua, B. Lynch, R.C. Newman, De-alloying of type 316 stainless steel in hot, concentrated sodium hydroxide solution, Corrosion Science, 46 (2004) 2117-2133.

[43] A. Bhattacharya, P.M. Singh, Effect of heat treatment on corrosion and stress corrosion cracking of S32205 duplex stainless steel in caustic solution, in, Springer Boston, 101 Philip Drive, Assinippi Park, Norwell, MA 02061, United States, 2009, pp. 1388-1399.

[44] K.R. Chasse, P.M. Singh, Corrosion study of super ferritic stainless steel UNS S44660 (26Cr-3Ni-3Mo) and several other stainless steel grades (UNS S31603,

S32101, and S32205) in caustic solution containing sodium sulfide, Metallurgical and Materials Transactions A, 44 (2013) 5039-5053.

[45] P. Marcus, Sulfur-assisted corrosion mechanisms and the role of alloyed elements, Corrosion Mechanismsin Theory and Practice, (2002).

[46] P. Hazlewood, P. Singh, J. Hsieh, Effect of black liquor oxidation on the stress corrosion cracking susceptibility of selected materials, Corrosion, 62 (2006) 765-772.

[47] A. Bhattacharya, P.M. Singh, Stress corrosion cracking of welded 2205 duplex stainless steel in sulfide-containing caustic solution, Journal of Failure Analysis and Prevention, 7 (2007) 371-377.

[48] A. Forty, P. Humble, The influence of surface tarnish on the stress-corrosion of α-brass, Philosophical Magazine, 8 (1963) 247-264.

[49] A.J. McEvily, A. Bond, On the initiation and growth of stress corrosion cracks in tarnished brass, Journal of the Electrochemical Society, 112 (1965) 131-138.

[50] A. Kington, F. Noble, σ phase embrittlement of a type 310 stainless steel, Materials Science and Engineering: A, 138 (1991) 259-266.

6. Effect of Thermal Treatment on the Grain Boundary Embrittlement of Type 310S Stainless Steel

Y. Jiao, Q. Wang, W. Zheng, J. McDermid, M. Maymond and J. Kish. Manuscript to be submitted to Materials Science and Engineering A, January 2018.

6.1 Introduction

This chapter presents a draft article (not yet submitted for publication), which documents research conducted to isolate and assess the intergranular SCC susceptibility of the two limiting thermally-aged Type 310S stainless steel conditions relative to the baseline in terms of the contributing mechanical factors only (degree of grain boundary embrittlement). This article is the second of three that, as a set, specifically address the SCC implications of both short-term and long-term thermally-aged microstructures in SCW described in Section 1.2 above and in the Stress Corrosion Cracking Implications Section in Chapter 3. Micro-mechanical measurements in combination with the uniaxial tensile measurements were conducted to provide key insight into how individual thermally-aged grain boundaries (micro-scale) controlled the bulk fracture (macro-scale) in the absence of a corrosive environment.

Prof. Kish at McMaster University and Prof. Zheng at CanmetMATERIALS are my supervisors. Prof. McDermid at McMaster University is my committee member after retirement of Dr. Guzonas. They were giving me guidance, instruction and edit manuscript. Prof. Daymond at Queens University is our collaborator and gave us suggestions and comments for micro-mechanical tests. Mr. Wang is a Ph.D student of Prof. Daymond and conducted the micro-mechanical tests for us and gave me instructions about data analysis. I was responsible for conceiving the research questions, collecting and analyzing the data, and writing the manuscripts. The study was approved by the McMaster Research Ethics Board at McMaster University (Hamilton, Ontario).

6.2 SCC Susceptibility Consideration

Stress corrosion cracking (SCC) has been identified as a damage mode that is expected to affect the in-service performance of metallic materials for fuel cladding in the Generation IV supercritical water cooled reactor design concept [1-5]. An understanding of the SCC mechanism and the associated controlling factors is required to help guide the selection of suitable candidate metallic materials with acceptable SCC resistance, in addition to considerations of other key material performance requirements. Key factors that will undoubtedly affect SCC in supercritical water (SCW) include the corrosivity of the SCW environment itself along with the material micro-structure, which can evolve during prolonged exposure to high temperature and irradiation during normal operation.

There is mounting evidence in the literatures suggesting that the evolved microstructures of austenitic stainless steels resulting from corrosion [6, 7], cold working [8, 9], thermal ageing [10] and/or irradiation [11-13] are susceptible to intergranular SCC in contact with SCW. It follows that the tendency for the grain boundary to preferentially corrode/oxidize and/or mechanically harden becomes an important factor in the overall cracking mechanism. On one hand, the causative factor has been linked to the formation of Cr-rich $M_{23}C_6$ carbides on grain boundaries and the concomitant development of Cr-depleted zone from either prior thermal ageing [10] or long term immersion [6, 7] in SCW, indicated by a strong preferential corrosion/oxidation effect. On the other hand, there are also results showing that the causative factor is linked to the degree of plastic deformation from either prior cold-working [8] or acquired during straining whilst immersed in SCW [9], indicating a strong effect of localized deformation in the low-stacking fault alloys. The matter is even more complex for irradiated microstructure, as the increased intergranular SCC severity in SCW has been correlated with both an increased level of radiation-induced segregation (RIS) (corrosion effect) and strain localization effect, which accompanies the general irradiation induced hardening of microstructure [11].

While it is understood that the contribution of each factor (grain boundary corrosion/oxidation and hardening), and possibly of some interactions between them, can be complex, a ‘first glance’ attempt to isolate and assess the potential contribution of each factor to the intergranular cracking mechanism in SCW is warranted [14]. The purpose of this study was to isolate and understand the potential for grain boundary hardening induced by thermal ageing alone. Type 310S stainless steel was used for this purpose since it is short-listed as a candidate fuel cladding material in the Canadian supercritical water-cooled reactor (SCWR) design concept [4, 5, 15]. Samples were thermally-aged to two special conditions and compared relative to a solution-annealed condition, which represented an ideal starting microstructure baseline. The special conditions consisted of a short-term thermal aging treatment to 'sensitize' the microstructure by forming Cr-rich $M_{23}C_6$ precipitates on the grain boundaries and adjacent Cr-depleted zones and a long-term thermal ageing treatment to 'harden' the microstructure by forming σ phase precipitates on the grain boundaries. The relative extent of grain boundary hardening was assessed using micro-mechanical approaches including nano-indentation measurements and load-displacement measurements of individual grain boundary micro-cantilevers prepared by focused ion beam (FIB) milling. Complementary uniaxial tensile measurements were also conducted using bulk samples to help link individual grain boundary behaviour to the macroscopic bulk material behavior.

6.3 Materials and Methods

6.3.1 Materials

All test coupons were prepared from commercial Type 310S austenitic stainless steel plate product provided in the mill-annealed (MA) condition. The chemical composition, as specified in the mill certificate, is shown in Table 6.1. Sub-sections of the plate were solution-annealed (SA), sensitized (S) or thermally-treated (TT) prior to preparing test samples. The SA treatment was conducted at 1050 °C for 1 h, followed by water-quenching to yield a baseline microstructure that would exhibit a low extent of micro structure instability. The S treatment was conducted at 650 °C for 100 h, followed by air-cooling to yield a 'sensitized' microstructure with significant $M_{23}C_6$ carbide precipitation on the grain boundaries concomitant with the development of adjacent Cr-depleted zones [16-19]. The TT treatment was conducted at 800 °C for 1000 h, followed by air-cooling to yield well-developed σ-phase precipitate formation on the grain boundaries and within the grains [16, 17, 20]. All sub-sections were sealed in a nitrogen-purged quartz tube during the heat treatments to prevent excessive oxidation.

Table 6.1 Chemical composition (wt.%) of the Type 310S plate product.

Cr	Ni	Mo	Mn	Si	P	S	C	Fe
24.4	19.3	0.16	1.36	0.8	0.02	<0.001	0.06	Bal.

A detailed characterization of the SA, S and TT microstructure using electron microscopy techniques has been published elsewhere [21]. The heat treatments were successful in producing the intended microstructural changes: $M_{23}C_6$ precipitate formation on the grain boundaries with adjacent Cr-depleted zone development in the S material and σ phase precipitate formation on the grain boundaries and within the grains, both without adjacent Cr-depleted zones, in the TT material. $M_{23}C_6$ grain boundary precipitates were also observed in the SA material, albeit to a significantly reduced extent relative to the S material. They were also present without adjacent Cr-depleted zones. High magnification standard light microscopy images of the heat-treated material microstructures are shown in Figure 6.1

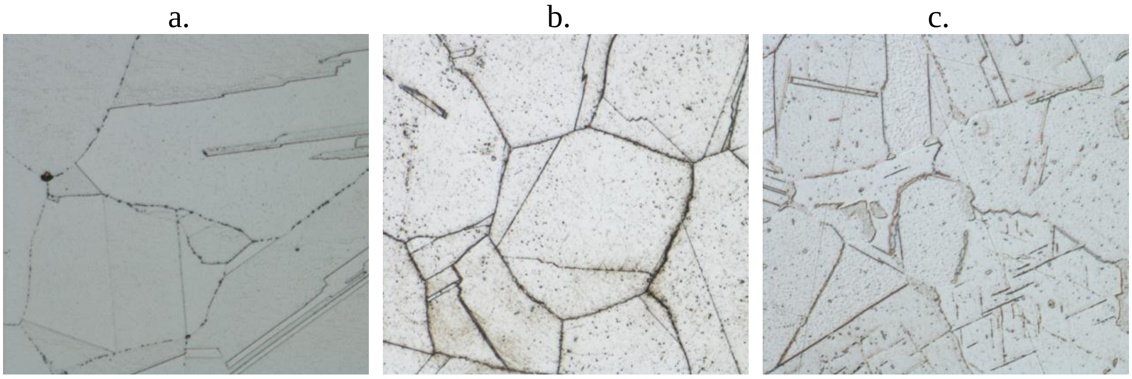

Figure 6.1 Standard light microscopy image showing the typical appearance of the heat-treated microstructure: (a) SA material, (b) S material and (c) TT material.

6.3.2 Micro-mechanical Measurements

The relative extent of grain boundary hardening was assessed using two micro-mechanical approaches including nano-indentation (hardness) on individual grain boundaries, as well as load-displacement bending measurements (loading/unloading modulus) of individual grain boundary micro-cantilevers prepared by focussed ion beam (FIB) milling. A Digital Instruments Nanoscope platform was used to perform these micro-mechanical measurements.

Starting rectangular (20 mm × 10 mm × 1.5 mm) samples were used for each measurement. Working surfaces were mechanically-abraded to a 1200 grit finish using SiC abrasive papers with water as a lubricant. Working surfaces for nano-indentation measurements were electrochemically polished at 25 V for 2 minutes in a 10%

perchloric acid, 90% methanol solution at −40°C. Working surfaces for micro-cantilever beam bending measurements were mechanically polished to a 1 μm surface finish using diamond paste suspension and then to a 0.05 μm surface finish using an alumina suspension. All polished working surfaces were ultra-sonically cleaned in acetone for 5 minutes and dried in air.

Nano-indentation measurements were made utilizing the load-displacement data acquired during a single loading/unloading cycle of the indenter [22, 23]. A Berkovich indenter [23] was used for this purpose. The associated hardness value of the indentation was calculated using the following relations [22]:

$$H \approx \frac{P}{24.5h_c^2} \tag{1}$$

$$h_a = \left(\frac{\pi - 2}{\pi}\right) h_e \tag{2}$$

$$h_{\max} = h_c + h_a \tag{3}$$

where H (P_a) is the hardness, P (N) is the maximum load applied, h_c (m) is the contact depth, h_a (m) is the depth of the contact circle measured from sample surface (m), h_e is the elastic depth of penetration for unloaded (m) and h_{max} (m) is the total indentation depth (including both elastic and plastic). Indentations were made using the constant displacing mode (h_{max} set at 1 μm) over a 10 × 10 array with a spacing of 100 μm between each measurement within the array to ensure multiple grain boundaries of each heat-treated material were included. Measurements in the array were classified as being either a grain or grain boundary measurement using light optical microscopy for the S and TT sample and scanning electron microscopy (JEOL JSM-7000F) for the SA sample.

The approach of performing micro-mechanical testing on grain boundaries samples prepared by FIB milling has been successfully utilized to investigate the effect of thermal ageing [24] and oxidation [25, 26] on grain boundary embrittlement due to oxidation. A similar approach to micro-cantilever bending experiments reported by Armstrong et al. [27, 28] was used. The FIB milling was carried out using a Zeiss NVision 40 CrossBeam Workstation. Two grain boundary micro-cantilever beams ~15 μm in length with a triangular cross-section (~3.5 μm base × ~3.5 μm height) were prepared in a single SA, S and TT sample (Figure 6.2a). The beams were prepared such that the grain boundary was located adjacent to the fixed end (location of the highest stress [28]). A secondary electron image of an as-milled grain boundary micro-cantilever beam in the SA, S and TT material is shown in Figure 6.2b-d respectively. Interrupted load-deflection curves were then recorded for the duplicate set of beams in each heat-treated material using a 0.01 mN/s loading rate (load control mode). Loading was interrupted after about 800 nm deflection to allow SEM imaging of the grain boundary region after acquiring a relative light deformation. The original intent of the second loading was to deflect the beams to fracture. However, the FIB-milled trenches were deep enough to permit deflection to fracture. Consequently, the second loading was interpreted again (final) after an about 3000 nm additional deflection (about 4000 nm total deflection) to allow SEM imaging of the grain boundary region after acquiring a relative heavy deformation.

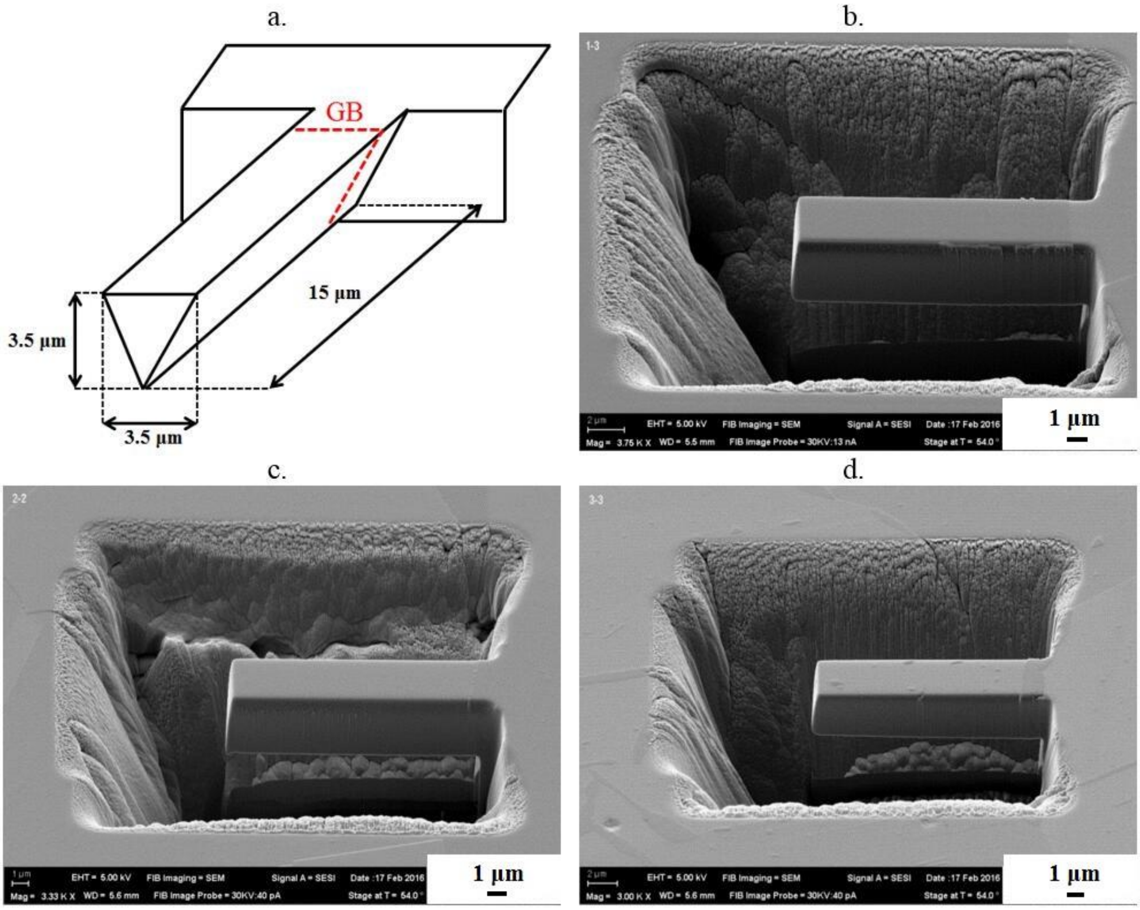

Figure 6.2 (a) schematic of triangular microcantilever beam and secondary electron images of as-milled grain boundaries of (b) SA, (c) S and (d) TT materials.

6.3.3 Uniaxial Tensile Measurements

Uniaxial tensile measurements were made using flat tensile samples (~2 mm thick) that were first machined from the commercial plate and then heat-treated to produce the SA, S or TT material. A drawing of the tensile sample is provided in Figure 6.3. The samples were mechanically-abraded to a 1200 grit surface finish using SiC abrasive papers and water as a lubricant and the polished to a 1 μm surface finish using a diamond paste suspension. A 100 kN tensile frame (MTS) was used to record the room temperature load-displacement response to fracture at a strain rate of 6.7 × 10^{-4} s^{-1}. The strain was calculated and monitored in real-time using a commercial digital image correlation (DIC) based stain measurement system (ARAMIS). One half of the fractured tensile sample was cold-mounted in cross-section, mechanically-abraded and polished to a 0.05 μm surface finish using the procedure describe above for the nano-scratching measurements. The other half of the fractured tensile sample was used for fractography, in which the fracture surface was rinsed in acetone and dried in air. Both samples were imaged using SEM (JEOL JSM-7000F).

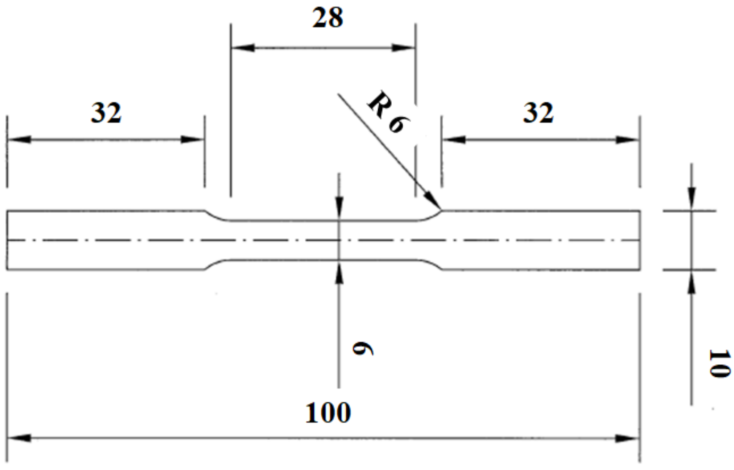

Figure 6.3 Drawing of the tensile bars.

6.4 Results

6.4.1 Nano-hardness Measurements

Figure 6.4a shows a secondary electron image of the nano-indentation array in part on the SA sample. Superimposed onto the image are symbols identifying indications that were assigned to a grain (G), twin (TW) or grain boundary (GB). This set of assignments show that the majority of indentations were made within the matrix, but a sufficient number of indentations on grain boundaries were made nevertheless. Table 6.2 compares the average grain (H_g) grain boundary hardness (H_{gb}) values. The uncertainty value listed along with the H value represents the 95% confidence interval of the data set. For illustrative purposes, Figure 6.4b compares the typical variation in hardness values measured along a horizontal line of the array (10 measurements) for each material. Qualitatively speaking, the TT material exhibited the greatest relative change in hardness values measured within the array, with the local increase in hardness values coinciding with grain boundaries. The H_{gb} value was higher than the H_g value for each material, which was the expected finding given that grain boundaries were decorated with precipitates: $M_{23}C_6$ in the SA and S materials and phase in the TT material. The TT material exhibited a higher H_{gb} value relative to the SA material. The H_{gb} value of the S material was lower relative to the SA material despite grain boundaries in both materials being decorated with $M_{23}C_6$ precipitates: more so in the S material (Figure 6.1.). Hardness values calculated from nano-indentation measurements are known to be highly sensitive to compositional variations [29] and indentation depths [23, 30]. The decorated grain boundaries in the S material were also associated with well-developed Cr-depleted zones, which were absent in SA material [21]. Thus, the decrease in H_{gb} value of the S material relative to the SA material, despite an increased degree of $M_{23}C_6$ decoration (Figure 6.1b), is likely a consequence of the softer Cr-depleted zone affecting the indentation depth on the grain boundary. A similar effect has been reported in the literature [31].

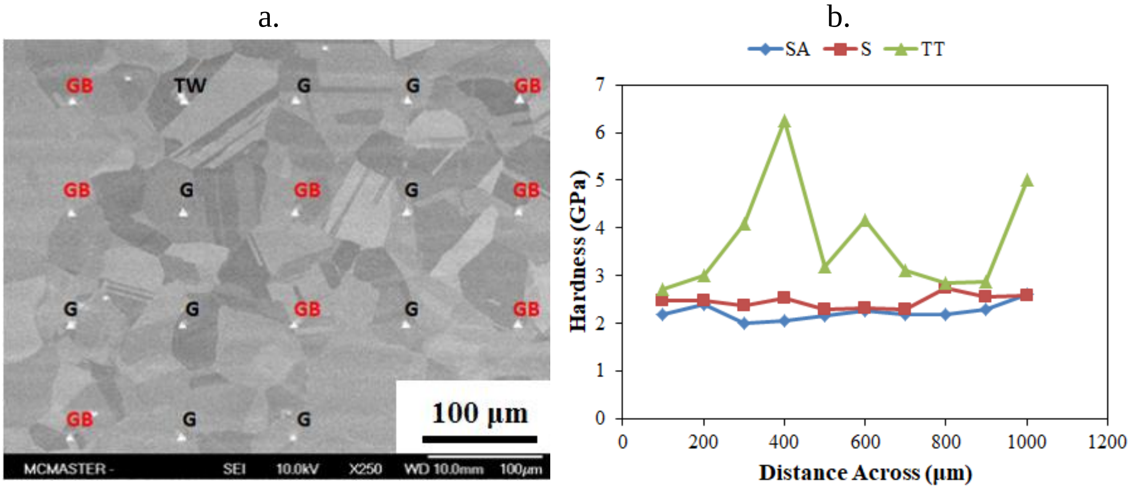

Figure 6.4 (a) a secondary electron image of the nano-indentation array in part on the SA sample and (b) the typical variation in hardness values measured along a horizontal line of the array (10 measurements) for each material.

Table 6.2 Summary of nano-indentation hardness data.

Material	Grain (GPa) (H_g)	Grain Boundary (GPa) (H_{gb})	% Relative Grain Boundary Strength
SA	2.45 (±0.11)	3.14 (±0.15)	---
S	2.60 (±0.12)	2.97 (±0.13)	−5%
TT	2.62 (±0.11)	6.13 (±1.27)	+95%

6.4.2 Micro-cantilever Beam Bending Measurements

Figure 6.5 shows the duplicate sets of interrupted bending load-deflection response of the grain boundary micro-cantilever beams prepared from the SA, S and TT materials. All curves exhibited similar features, consisting of presumably an initial elastic deformation region followed by a plastic deformation region. Two features immediately stand out. The first feature is the discontinuity between the first and second loading curves for the duplicate SA beams. The nature of the discontinuity implies that the SA beams were additionally deformed (further work hardened) during the interruption period (between the first and second load-deflection measurement). The cause of the additional work hardening is likely from accidently selecting the beam itself to conduct the zero depth position calibration measurement. The second feature is the significant difference between the duplicate load-deflection curves of the S material beams. This discrepancy is a result of the difference in beam dimensions, as the S-2 beam had a smaller cross-sectional area than the S1 beam. Small 'steps' features were evident in the plastic deformation region of each first loading curve. Such steps are believed to be indicative of a slip-type deformation mode [32]. The micro-mechanical instrumentation was likely unable to resolve the small load increase that occurs after slip, thus yielding a flat step appearance in the recorded data.

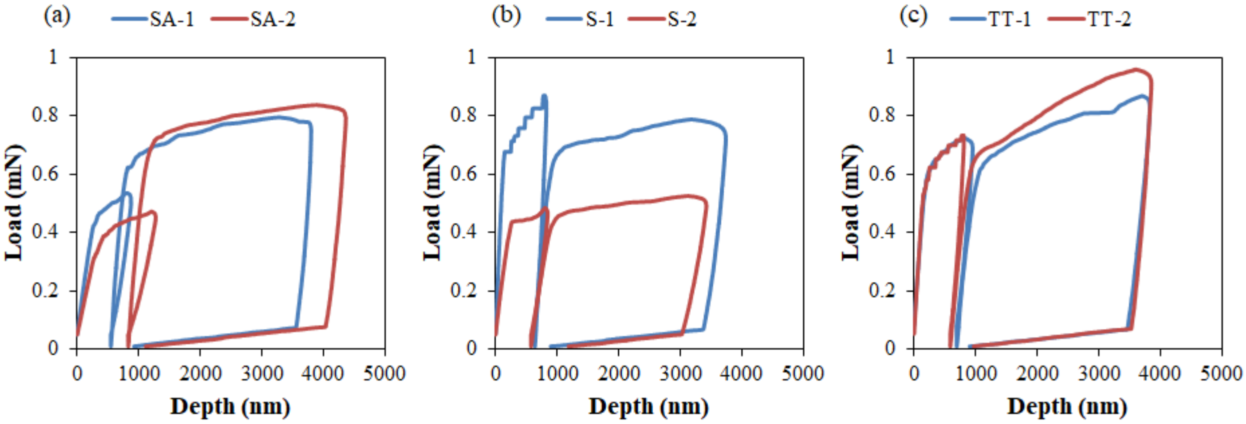

Figure 6.5 Interrupted bending load-deflection response of the grain boundary micro-cantilever beams of (a) SA, (b) S and (c) TT materials.

A set of SEM images of the grain boundary micro-cantilever beams (one per material) after interrupted loadings is shown in Figure 6.6. All beams were intact after bending (that is, no fracture was observed). Small slip displacements along many close-packed planes were clearly visible in the austenite matrix adjacent to grain boundary in the SA, S and TT material beams, after both low (first load cycle) and high (second load cycle) plastic deformation. Evidence of necking (plastic instability) was not observed on any of the beams after the first load cycle. However, significant necking was observed on the TT material beam (Figure 6.6f) and on the S material beam (Figure 6.6e) to a lesser extent. The necking in both materials occurred in the authentic matrix adjacent to the grain boundary. No obvious plastic deformation of the relatively coarse σ phase precipitate was observed, nor was any obvious decohesion between the austenite matrix and the σ phase precipitate observed. Micro-void formation was visible adjacent to the intact (non-cracked) $M_{23}C_6$ precipitates on the grain boundary of the S material beam after the first load cycle (Figure 6.6b). Similar micro-void formation was not observed on either the grain boundary of the SA material beam or adjacent to intact (non-cracked) σ phase precipitate on the grain boundary of the TT material beam, even after the second load cycle.

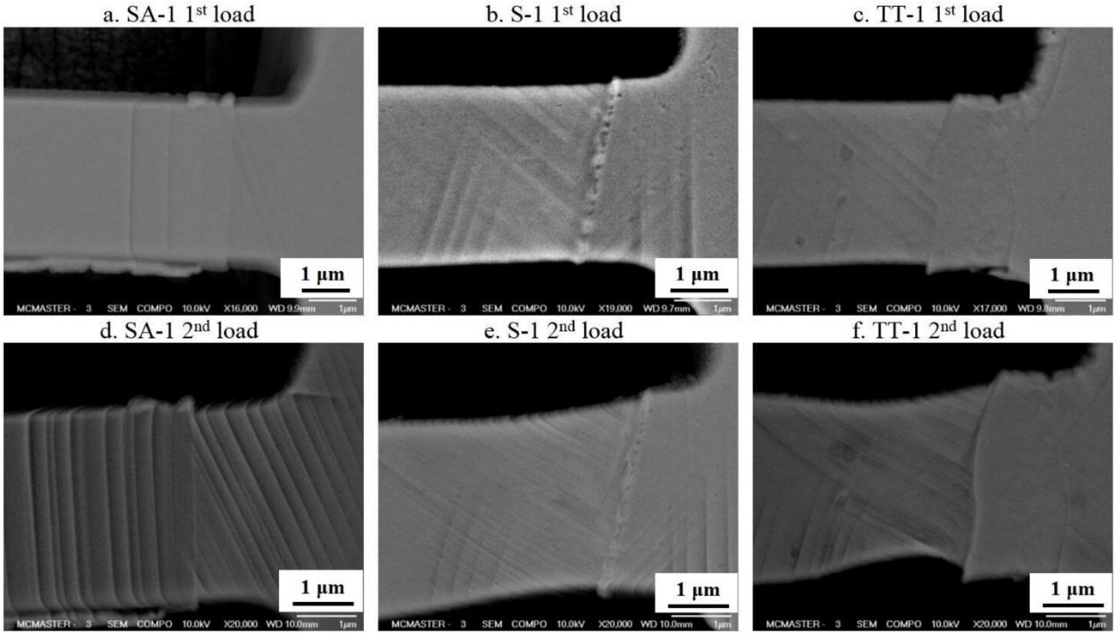

a. SA-1 1st load b. S-1 1st load c. TT-1 1st load

d. SA-1 2nd load e. S-1 2nd load f. TT-1 2nd load

Figure 6.6 SEM images of the grain boundary micro-cantilever beams after interrupted loadings: (a) SA, (b) S and (c) TT materials after 1st load; (d) SA, (e) S and (f) TT materials after 2nd load.

6.4.3 Uniaxial Tensile Measurements

Figure 6.7 shows the triplicate set of stress-strain responses measured for the SA, S and TT materials. Each material exhibited an initial elastic deformation region followed by a plastic deformation region. Table 6.3 lists the associated average values of the uniaxial tensile properties. The uncertainty value listed along with the H value represents the 95% confidence interval of the data set. Thermal ageing had a complex effect on the uniaxial tensile properties of Type 310S stainless steel. The S material exhibited similar yield strength, but higher ultimate tensile strength and lower fracture strain relative to the SA material. The fracture strain (ε_f) was calculated using ln (A_o/A_f), where A_o is the original cross-section area and A_f is the cross-sectional area at fracture. The TT material exhibited a higher yield and ultimate tensile strength but a lower fracture strain relative to the SA material. Comparing the two thermally-aged materials, the TT material exhibited a higher yield and ultimate tensile strength and lower fracture strain relative to the S material. Also listed in Table 6.3 is the embrittlement ratio (ER) determined by normalizing the fracture strain of the thermally-aged material relative to the SA material (ER_ε) and the % reduction in area (% RA) determined by normalizing the change in cross-sectional area at fracture relative to the original cross-sectional area (ER_A). Both of these metrics clearly show that, of the two thermally-aged materials, the TT material exhibits the largest extent of embrittlement (larger ER_ε and smaller ER_A relative to the SA material).

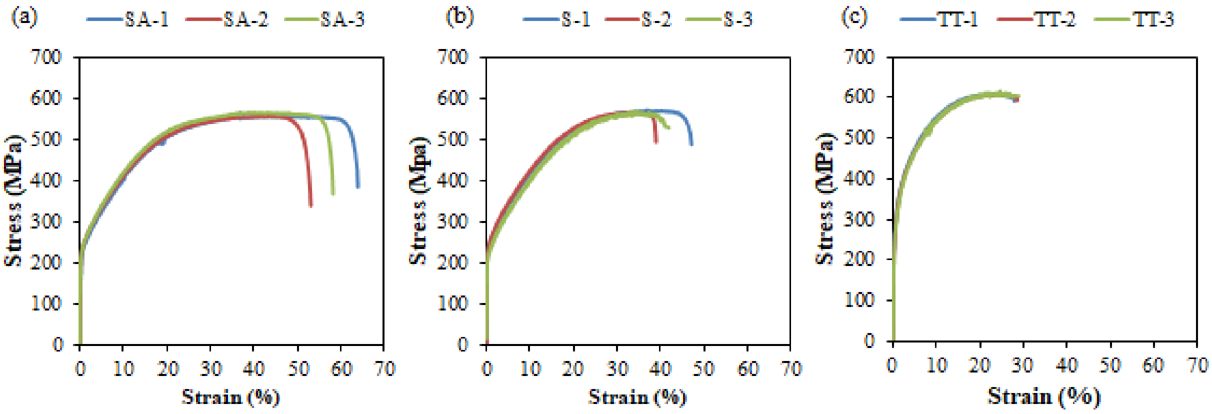

Figure 6.7 Strain stress curves of (a) SA, (b) S and (c) TT materials.

Table 6.3 Summary of uniaxial tensile testing data.

Material	YS (MPa)	UTS (MPa)	Fracture Strain (%)	ER_ε	% RA	ER_A
SA	211 (±8)	557 (±18)	59 (±7)	---	54 (±1)	---
S	212 (±14)	566 (±17)	43 (±10)	0.27	41 (±4)	0.24
TT	241 (±29)	610 (±2)	28 (±1)	0.53	20 (±4)	0.63

Figure 6.8 shows a set of SEM images of the fracture surfaces after uniaxial tensile testing in both plan and cross-sectional views. The fracture surface of the SA material (Figure 6.8a) revealed classic ductile tearing features via micro-void formation and coalescence. Both thermally-aged materials exhibited distinctly difference fracture surface, relative to the SA material and to each other. Classic intergranular fracture features were observed on the S material fracture surface (Figure 6.8b), whereas transgranular mixed-mode features were observed on the TT material fracture surface (Figure 6.8c). The mixed-mode features include cleavage of the large harder σ phase precipitates and ductile fracture of the softer austenite matrix. Figure 6.8d shows a backscattered image of a secondary intergranular crack propagating into the S material from the main fracture surface in cross-section. Micro-void formation was present on the grain boundary ahead of the crack tip. A similar backscattered image of the TT material fracture surface in cross-section is shown in Figure 6.8e. Micro-void formation was also evident on the grain boundaries (without associated secondary cracking), however it is clear that formation was caused by cracking of the relatively coarse σ phase precipitates in this material.

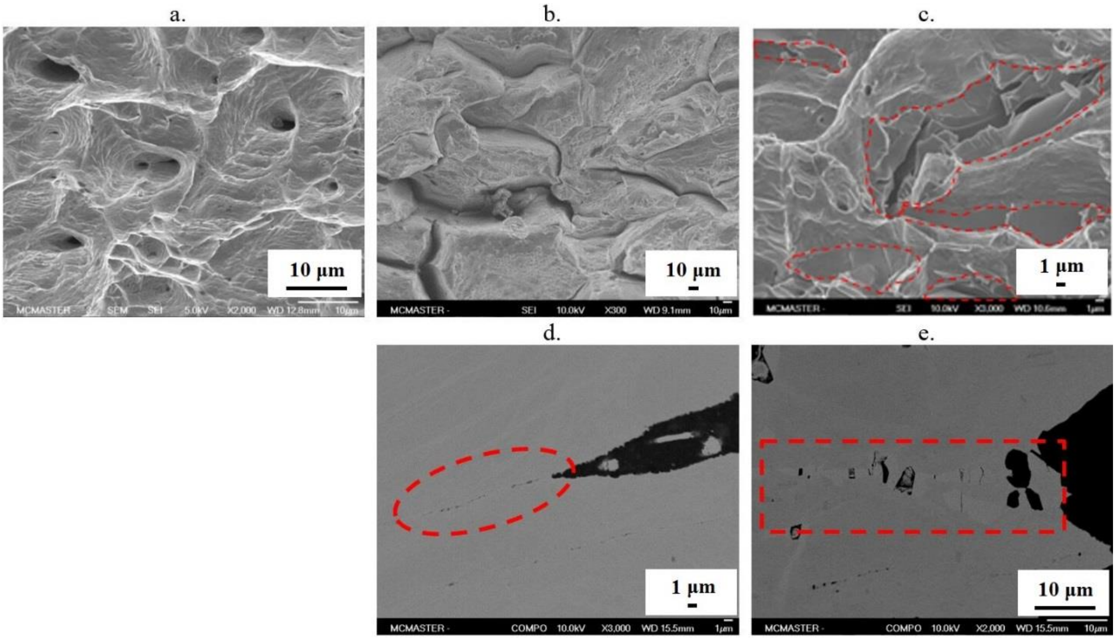

Figure 6.8 SEM images of the fracture surfaces after uniaxial tensile testing in both plan and cross-sectional views: (a) SA material, (b) and (d) S materials and (c) and (e) TT material.

6.5 Discussion

The objective of this work was to assess the relative extent of grain boundary hardening in two limiting cases of thermally-aged Type 310S stainless steel, relative to the SA baseline, by measuring individual grain boundary mechanical properties as a suitable indicator of intergranular fracture. As it happened, complementary bulk uniaxial tensile measurements revealed both the S and TT material were hardened relative to the SA material, but that the grain boundaries in the S material were sufficiently sensitized to cause intergranular fracture. This finding provided the opportunity to benchmark the two micro-mechanical approaches utilized as suitable indicators and to help elucidate key factors that control intergranular fracture in the process.

6.5.1 Grain Boundary Hardening

The approach of using nano-indentation measurement to assign a hardness value to the grain boundaries as a potential grain boundary hardening indicator proved to be problematic. Typically $M_{23}C_6$ precipitates are relative small in both size (nanometer scale) and volume fraction in austenitic stainless steels [17], even after long-term ageing [33]. The intrinsically small size made it very difficult to measure a meaningful hardness of such precipitates decorating grain boundaries using nano-indentation free of surrounding matrix influence since the plastic deformation zone is about typically three times larger than the indent itself. The hardness of the $Cr_{23}C_6$ phase has been estimated to be ~13-15 GPa [32, 34]. Thermal ageing induced $M_{23}C_6$ precipitate formation typically contain substitutional alloying elements such as Fe and Mn [17], which can decrease the hardness of the phase by weakening the bond strength [35]. As mentioned previously, the H_{gb} value of the S material (2.97 ± 0.13 GPa) was significantly under estimated because of the likely incorporation of the adjacent soft Cr-depleted zone in the measurement. On the other hand, the intrinsically coarser phase grain boundary precipitates in the TT material were more amenable for hardness measurements using nano-indentation. A value of 17.2 ± 1.3 GPa has been reported for σ phase grain boundary precipitates (using load-control indentations to a maximum of 500 μN) formed during long term thermal ageing of Type 316 stainless steel [30]. In that study, the indentation depth was ~20 nm, which is significantly shallower than the indentation depth of 500 nm displacement control approach used in this study. Therefore, the H_{gb} value of the TT material (6.13 ± 1.27 GPa) reported herein was also likely underestimated because of some incorporation of the adjacent softer austenite matrix in the measurement. Despite the likely underestimated H_{gb} values, the TT material exhibits the highest relative H_{gb} value and the SA material exhibits the lowest. Such a relative ranking suggests that the TT material would be more prone to embrittlement by intergranular fracture than either the S or SA material if the H_{gb} value proved to be a suitable indicator. The fractography of the uniaxial tensile samples reveal that this is not the case as the S material, rather than the TT material, fractured by intergranular cracking. Not too surprisingly, hardening and the associated fracture mode of thermally-aged Type 310S stainless steel is more complex than just simply being linked to the hardness of a given grain boundary precipitate.

The approach of using micro-cantilever grain boundary beam bending measurements also proved to be problematic since none of the beams fractured. Despite the absence of fracture, this approach did show some promise as significant deformation damage accumulation as a likely precursor to fracture was observed in both the S material beam (micro-void formation on grain boundaries) and the TT material beam (significant necking adjacent to the grain boundary σ phase precipitate). Regardless, these clear differences in deformation accumulation do provide insight into the factors contributing to the observed fracture modes exhibited by the bulk material caused by thermal ageing.

Intergranular fracture in the presence of grain boundary precipitates typically involves micro-void formation and coalescence along the grain boundaries. The process involves either precipitate cracking or precipitate/matrix interface decohesion when the normal stress at the interface exceeds the critical fracture stress or the strain energy stored during plastic deformation exceeds the energy of the new surfaces formed by micro-void formation [36]. Evidence of micro-void formation was found on the S material grain boundaries (Figure 6.6b and 6.8d), but not on the TT material grain boundaries (Figure 6.6d and 6.8e) despite the grain boundary precipitate cracking that was observed in the bulk material (Figure 8e). The size rather than the type of grain boundary precipitate is likely a controlling factor here similar to that voids formation during creep tests [35, 37, 38]. Grain boundary carbide precipitates are known to promote micro-void formation in austenitic stainless steel during elevated temperature creep testing due to their intrinsically small size [17, 30, 39, 40]. On the other hand, the ability for grain boundary σ phase precipitates to promote micro-void formation depends on the size: formation accompanying relatively small σ phase precipitates (short term thermal ageing) and not accompanying relatively large σ phase precipitates (long term thermal ageing) [41, 42].

Residual internal stresses developed around a second-phase precipitates due to plastic incompatibilities between a hard (elastic) precipitate embedded in a soft (elastic-plastic) matrix give rise to large Bauschinger effects that can induce precipitate/matrix decohesion [38]. During the uniaxial tensile test of S material, micro-stress accumulation likely induced $M_{23}C_6$/matrix decohesion, which in turn induced micro-void formation on the grain boundaries. Micro-void formation in TT material, however, was induced by fracture of relatively large σ phase precipitates on the grain boundaries (Figure 6.8e). As the hard σ phase has much higher Young's modulus than the austenite matrix [20], it is likely deforming elastically (during both uniaxial tensile testing and micro-cantilever beam bending) even though the surrounding softer austenite matrix is deforming plastically. The strain energy is consequently accommodated within the softer austenite matrix phase [43]. On the other hand, as the hard σ phase is brittle and resistant to plastic deformation during straining [20, 44], it likely will be prone to fracture far below the critical stress required to cause σ phase/matrix decohesion.

Figure 6.9 schematically shows the micro-mechanistic aspects governing the fracture process of the two thermally-aged bulk materials. Classic micro-void formation involving a $M_{23}C_6$/matrix decohesion process occurs on the S material grain boundaries. Intergranular facture occurs as these micro-voids coalesce on the grain boundaries. In contrast, micro-void formation involving cracking of the large hard σ phase precipitates occurs in the TT material grain boundaries. Transgranular ductile fracture of the softer austenite matrix occurs as these micro-voids coalesce across the grains as the softer grains need to accommodate the stress after fracture of hard σ phase precipitates. Due to the non-uniform distribution of the stresses within the grains [45], the degree of work hardening varies and ductile fracture tends to propagate along the grains accommodating the highest stress.

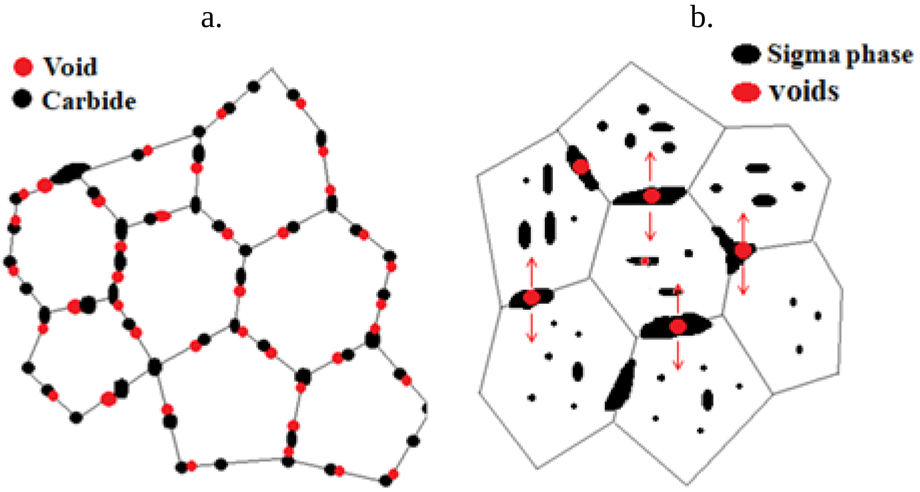

Figure 6.9 Schematic of cracking mechanism of (a) S and (b) TT materials during tensile tests at room temperature.

6.5.2 Localized Deformation Model for Intergranular SCC

During plastic deformation, slip steps will form on the surface resulting from slip lines intersecting the surface [46]. An example of such behavior is clearly apparent on the micro-cantilever beam surfaces, as shown in Figure 6.6a and 6.6b. Here, qualitatively speaking, the size and number of slip steps increase with increased plastic deformation. The size (height) of surface slip step is proportional to the strain energy stored in the slip line [47-49]: slip step height increasing with the extent of external stress applied (increased dislocations generation coupled with restricted dislocation movement) until a saturation value is attained. When slip lines interact with a grain boundary, slip can either transmit from one grain to another or be terminated the boundary [48]. Transmission of slip from one grain to another can serve to relive stress accumulation at grain boundary [48, 50]. When the slip is terminated at the grain boundary, the stress accumulated could either relatively high or low depending upon how many dislocations are piled-up [48]. The pile-up of dislocations at a grain boundary can induce a sufficiently large amount of localized deformation serving to induce grain boundary sliding or ledge formation as stress relief mechanisms [48]. Alternatively, the accumulated stress can be relieved by other means such as crack initiation [50]. During plastic deformation, alloys with lower stacking fault energy (SFE) tend to prompt planar slip with relatively large amount of deformation in each slip lines/dislocation channels, whereas alloys with high SFE tend to prompt cross-slip with more homogeneous slip line/channel height and spacing [47, 51]. Coarse secondary phase precipitates can be effective in blocking slip, serving to reduce localized stress accumulation at grain boundaries associated with slip line interactions [52, 53]. The blocking results in localized stress accumulation at the precipitate matrix interface, which can be relieved by precipitate cracking when the stress exceeds a critical value (fracture stress).

Significant σ phase precipitate cracking was observed in the TT material after uniaxial tensile testing to fracture. In light of the discussion above, such cracking may also prove to be a key micro-mechanistic aspect involved in the proposed localized deformation intergranular SCC mechanism. The working theory here is that the coarse σ phase precipitates in the TT material would effectively block slip, serving to reduce localized stress accumulation at grain boundaries associated with slip line interactions and thus decrease the intergranular SCC susceptibility in SCW. The theory will be investigated in some detail by conducting slow strain rate testing of the SA, S and TT material in 25 MPa flowing SCW at 500 °C, the results of which will be presented and discussed in a future publication. In the meantime, an initiative was taken here to pull electro-polished uniaxial tensile samples to 10% strain to provide some insight into the relative difference in slip line damage accumulation resulting from interaction with the sample surface. Figure 6.10 shows SEM plan-view images of the sample surfaces after being strained to 10%. Qualitatively speaking, the number of slip lines visible is significantly smaller on the TT material surface (Figure 6.10c) relative to the SA material (Figure 6.10a) and S material (Figure 6.10b) surfaces. Under higher magnification it is clear that slip lines terminated at σ phase precipitates (Figure 6.10d). Thus, there is less localized deformation damage accumulated at surface resulting from slip in the TT material than either the SA or S material for the same level of bulk uniform plastic strain. The observations are indeed consistent with the working theory that the coarse σ phase precipitates, formed as a consequence of longer-term thermal ageing, may actually be beneficial in decreasing the intergranular SCC susceptibility of Type 310S stainless steel exposed in SCW by mitigating localized deformation damage accumulation at grain boundaries.

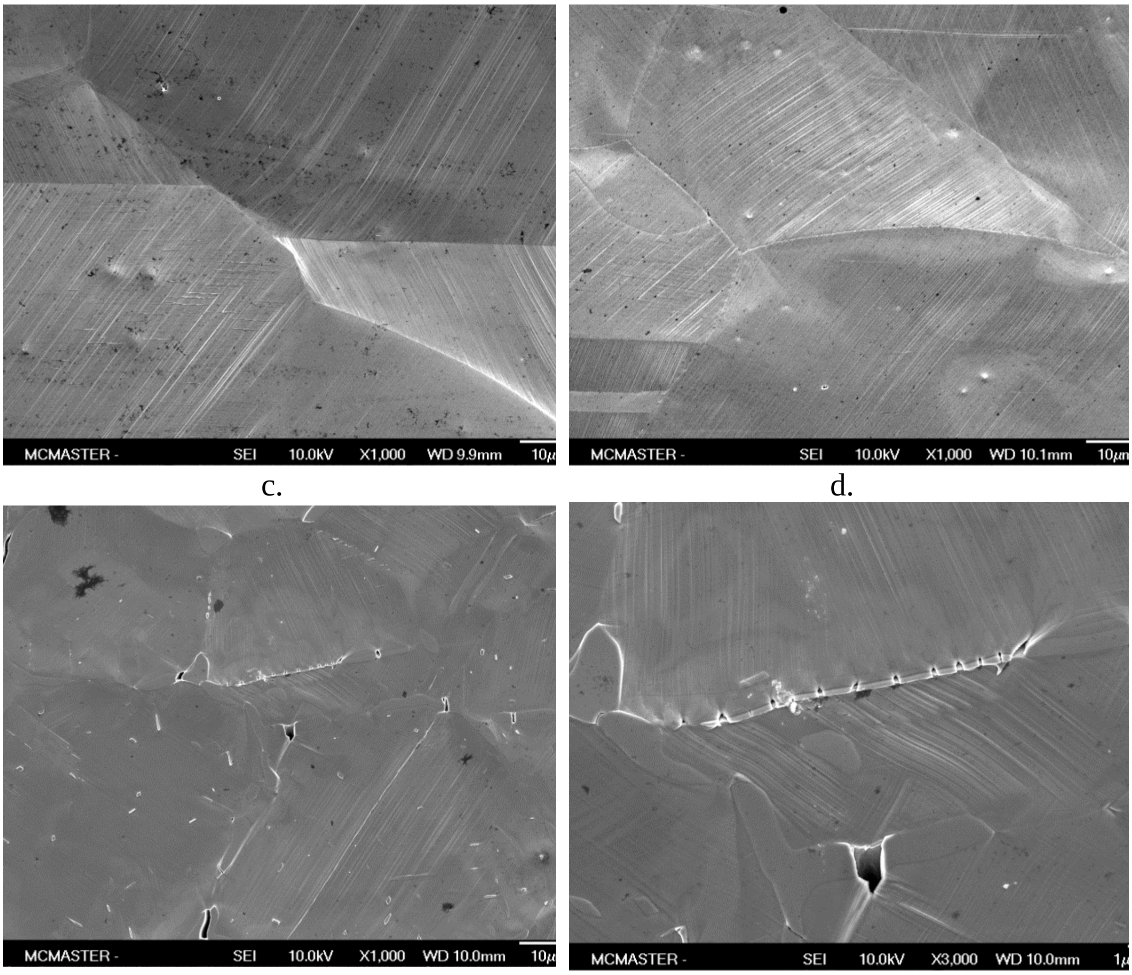
a. b. c. d.

Figure 6.10 SEM plan-view images of the electrochemical polished surfaces after being strained to 10% of (a) SA, (b) S, (c) and (d) TT materials.

6.6 Conclusions

- Both nano-indentation and micro-cantilever beam bending measurements were made on individual grain boundaries in two limiting cases of thermally-aged Type

310S stainless steel material. Of the two micro-mechanical measurements, micro-cantilever beam bending measurements is the more promising approach to quantitatively assess the relative extent of grain boundary hardening caused by thermal ageing.

- Bulk uniaxial tensile measurements revealed both the S and TT material were hardened relative to the SA material. The associated fractography revealed that the grain boundaries in the S material were sufficiently sensitized to cause intergranular fracture, whereas the grain boundaries in the TT material were not sufficiently weakened to cause intergranular fracture.
- Micro-void formation involving a $M_{23}C_6$/matrix decohesion process occurs on the S material grain boundaries. Intergranular facture occurs as these micro-voids coalesce on the grain boundaries. In contrast, cracking of the large hard σ phase precipitates occurs in the TT material grain boundaries. Transgranular ductile fracture of the softer austenite matrix occurs as these micro-voids coalesce across the grains as the softer grains need to accommodate the stress after fracture of hard σ phase precipitates.
- Less localized deformation damage was found to accumulated at grain boundaries in the TT material resulting from slip than either in the SA or S material, for the same level of bulk uniform plastic strain because the ability of the coarse σ phase precipitates to effectively block slip. This finding has meaningful implications

regarding the inter-granular SCC susceptibility of Type 310S stainless steel exposed in both light water and supercritical water reactors since coarse σ phase precipitate formation associated with longer-term thermal ageing may actually be effective in decreasing susceptibility.

6.7 References:

[1] G. Was, P. Ampornrat, G. Gupta, S. Teysseyre, E. West, T. Allen, K. Sridharan, L. Tan, Y. Chen, X. Ren, Corrosion and stress corrosion cracking in supercritical water, Journal of Nuclear Materials, 371 (2007) 176-201.

[2] X. Ru, R.W. Staehle, Historical experience providing bases for predicting corrosion and stress corrosion in emerging supercritical water nuclear technology: Part 1 - Review, Corrosion, 69 (2013) 211-229.

[3] S.J. Zinkle, P.J. Maziasz, R.E. Stoller, Dose dependence of the microstructural evolution in neutron-irradiated austenitic stainless steel, Journal of Nuclear Materials, 206 (1993) 266-286.

[4] D. Guzonas, R. Novotny, Supercritical water-cooled reactor materials – Summary of research and open issues, Progress in Nuclear Energy, 77 (2014) 361-372.

[5] W. Zheng, D. Guzonas, K.P. Boyle, J. Li, S. Xu, Materials Assessment for the Canadian SCWR Core Concept, JOM, 68 (2016) 456-462.

[6] Y. Behnamian, A. Mostafaei, A. Kohandehghan, B.S. Amirkhiz, J. Li, R. Zahiri, E. Aghaie, W. Zheng, D. Guzonas, M. Chmielus, Internal oxidation and crack

susceptibility of alloy 310S stainless steel after long term exposure to supercritical water at 500° C, The Journal of Supercritical Fluids, 120 (2017) 161-172.

[7] Y. Behnamian, A. Mostafaei, A. Kohandehghan, B. Zahiri, W. Zheng, D. Guzonas, M. Chmielus, W. Chen, J.L. Luo, Corrosion behavior of alloy 316L stainless steel after exposure to supercritical water at 500° C for 20,000 h, The Journal of Supercritical Fluids, 127 (2017) 191-199.

[8] Y. Tsuchiya, F. Kano, N. Saito, M. Ookawa, J. Kaneda, N. Hara, Corrosion and SCC properties of fine grain stainless steel in subcritical and supercritical pure water, in: Corrosion 2007, March 11, 2007 - March 15, 2007, National Assoc. of Corrosion Engineers International, Nashville, TN, United states, 2007, 074151-0741513.

[9] Y. Zeng, J. Li, B.S. Amirkhiz, W. Zheng, M. Matchim, M. Podlesny, Corrosion and stress corrosion cracking of UNS S31008 and UNS N08810 alloys in supercritical water, in: Corrosion 2015, NACE International, 2015.

[10] Y. Watanabe, H. Abe, Y. Daigo, R. Fujisawa, M. Sakaihara, Effect of physical property and chemistry of water on cracking of stainless steels in sub-critical and supercritical water, in: Key engineering materials, Trans Tech Publ, 2004, 1031-1036.

[11] S. Teysseyre, Z. Jiao, E. West, G. Was, Effect of irradiation on stress corrosion cracking in supercritical water, Journal of Nuclear Materials, 371 (2007) 107-117.

[12] E. West, G. Was, IGSCC of grain boundary engineered 316L and 690 in supercritical water, Journal of Nuclear Materials, 392 (2009) 264-271.

[13] E. West, G. Was, A model for the normal stress dependence of intergranular cracking of irradiated 316L stainless steel in supercritical water, Journal of Nuclear Materials, 408 (2011) 142-152.

[14] Y. Jiao, W. Zheng, D. Guzonas, J. Kish, Microstructure Instability of Candidate Fuel Cladding Alloys: Corrosion and Stress Corrosion Cracking Implications, JOM, 68 (2016) 485-489.

[15] D. Guzonas, M. Edwards, W. Zheng, Assessment of candidate fuel cladding alloys for the Canadian supercritical water-cooled reactor concept, Journal of Nuclear Engineering and Radiation Science, 2 (2016) 011016.

[16] W. White, I. Le May, Metallographic observations on the formation and occurrence of ferrite, sigma phase, and carbides in austenitic stainless steels: Part I: Studies of AISI Type 310 Stainless Steel, Metallography, 3 (1970) 35-50.

[17] T. Sourmail, Precipitation in creep resistant austenitic stainless steels, Materials science and technology, 17 (2001) 1-14.

[18] S.S.M. Tavares, V. Moura, V.C. da Costa, M.L.R. Ferreira, J.M. Pardal, Microstructural changes and corrosion resistance of AISI 310S steel exposed to 600-800C, Materials Characterization, 60 (2009) 573-578.

[19] J. Qian, C. Chen, H. Yu, F. Liu, H. Yang, Z. Zhang, The influence and the mechanism of the precipitate/austenite interfacial C-enrichment on the intergranular corrosion sensitivity in 310S stainless steel, Corrosion Science, 111 (2016) 352-361.

[20] E. Hall, S. Algie, The sigma phase, Metallurgical reviews, (2013).

[21] Y. Jiao, J. Kish, W. Zheng, D. Guzonas, On the Role of Grain Boundary Chemistry in the Intergranular Stress Corrosion Cracking Susceptibility of 310S Exposed in Supercritical Water, in: The 7th International Symposium on Supercritical Water-Cooled Reactors, Proc. ISSCWR-7, Helsinki, Finland, 2015.

[22] A.C. Fischer-Cripps, Nanoindentation testing, in: Nanoindentation, Springer, 2011, pp. 21-37.

[23] N. Tayebi, A.A. Polycarpou, T.F. Conry, Effects of substrate on determination of hardness of thin films by nanoscratch and nanoindentation techniques, Journal of materials research, 19 (2004) 1791-1802.

[24] K. Fujii, K. Fukuya, Development of micro tensile testing method in an FIB system for evaluating grain boundary strength, Materials transactions, 52 (2011) 20-24.

[25] H. Dugdale, D.E.J. Armstrong, E. Tarleton, S.G. Roberts, S. Lozano-Perez, How oxidized grain boundaries fail, Acta Materialia, 61 (2013) 4707-4713.

[26] J. Dohr, D.E. Armstrong, E. Tarleton, T. Couvant, S. Lozano-Perez, The influence of surface oxides on the mechanical response of oxidized grain boundaries, Thin Solid Films, 632 (2017) 17-22.

[27] D.E.J. Armstrong, A.J. Wilkinson, S.G. Roberts, Micro-mechanical measurements of fracture toughness of bismuth embrittled copper grain boundaries, Philosophical Magazine Letters, 91 (2011) 394-400.

[28] R. Ding, J. Gong, A.J. Wilkinson, I.P. Jones, Transmission electron microscopy of deformed Ti–6Al–4 V micro-cantilevers, Philosophical Magazine, 92 (2012) 3290-3314.

[29] M. Kunert, B. Baretzky, E. Mittemeijer, S. Baker, Hardness-depth profiling on nanometer scale, Metallurgical and Materials Transactions A, 32 (2001) 1201-1209.

[30] T. Ohmura, K. Tsuzaki, K. Sawada, K. Kimura, Inhomogeneous nano-mechanical properties in the multi-phase microstructure of long-term aged type 316 stainless steel, Journal of Materials research, 21 (2006) 1229-1236.

[31] P. Shankar, H. Shaikh, S. Sivakumar, S. Venugopal, D. Sundararaman, H.S. Khatak, Effect of thermal aging on the room temperature tensile properties of AISI type 316LN stainless steel, Journal of Nuclear Materials, 264 (1999) 29-34.

[32] K. Hirota, K. Mitani, M. Yoshinaka, O. Yamaguchi, Simultaneous synthesis and consolidation of chromium carbides (Cr_3C_2, Cr_7C_3 and $Cr_{23}C_6$) by pulsed

electric-current pressure sintering, Materials Science and Engineering: A, 399 (2005) 154-160.

[33] T. Sourmail, H. Bhadeshia, Modelling simultaneous precipitation reactions in austenitic stainless steels, Calphad, 27 (2003) 169-175.

[34] Y. Li, Y. Gao, B. Xiao, T. Min, Y. Yang, S. Ma, D. Yi, The electronic, mechanical properties and theoretical hardness of chromium carbides by first-principles calculations, Journal of Alloys and Compounds, 509 (2011) 5242-5249.

[35] S.D. Antolovich, R.W. Armstrong, Plastic strain localization in metals: origins and consequences, Progress in Materials Science, 59 (2014) 1-160.

[36] R.W. Hertzberg, Deformation and fracture mechanics of engineering materials, (1989).

[37] A. Argon, J. Im, R. Safoglu, Cavity formation from inclusions in ductile fracture, Metallurgical and Materials Transactions A, 6 (1975) 825-837.

[38] Y.W. Chang, R. Asaro, Bauschinger effects and work-hardening in spheroidized steels, Metal Science, 12 (1978) 277-284.

[39] H.U. Hong, S.W. Nam, Improvement of creep-fatigue life by the modification of carbide characteristics through grain boundary serration in an AISI 304 stainless steel, Journal of materials science, 38 (2003) 1535-1542.

[40] K. Kim, H. Hong, K. Min, S. Nam, Correlation between the carbide morphology and cavity nucleation in an austenitic stainless steels under creep-fatigue, Materials Science and Engineering: A, 387 (2004) 531-535.

[41] J. Lai, A. Wickens, Microstructural changes and variations in creep ductility of 3 casts of type 316 stainless steel, Acta Metallurgica, 27 (1979) 217-230.

[42] J. Lai, A. Wickens, Effect of intergranular particle size and spacing on creep ductility of type 316 stainless steel, Scripta Metallurgica, 13 (1979) 1197-1198.

[43] D. Dye, H. Stone, R. Reed, Intergranular and interphase microstresses, Current opinion in solid state and materials Science, 5 (2001) 31-37.

[44] J. Lee, Y. Earmme, H. Aaronson, K. Russell, Plastic relaxation of the transformation strain energy of a misfitting spherical precipitate: ideal plastic behavior, Metallurgical and Materials Transactions A, 11 (1980) 1837-1847.

[45] M. Marcinkowski, D. Miller, A study of defect sub-structures in the Fe–Cr sigma phase by means of transmission electron microscopy, Philosophical magazine, 7 (1962) 1025-1059.

[46] G.S. Was, D. Farkas, I.M. Robertson, Micromechanics of dislocation channeling in intergranular stress corrosion crack nucleation, Current Opinion in Solid State and Materials Science, 16 (2012) 134-142.

[47] Z. Jiao, J.T. Busby, G.S. Was, Deformation microstructure of proton-irradiated stainless steels, Journal of Nuclear Materials, 361 (2007) 218-227.

[48] Z. Jiao, G.S. Was, Localized deformation and IASCC initiation in austenitic stainless steels, Journal of Nuclear Materials, 382 (2008) 203-209.

[49] Z. Jiao, G. Was, T. Miura, K. Fukuya, Aspects of ion irradiations to study localized deformation in austenitic stainless steels, Journal of Nuclear Materials, 452 (2014) 328-334.

[50] B. Cui, J. Kacher, M. McMurtrey, G. Was, I.M. Robertson, Influence of irradiation damage on slip transfer across grain boundaries, Acta Materialia, 65 (2014) 150-160.

[51] G.S. Was, Y. Ashida, P.L. Andresen, Irradiation-assisted stress corrosion cracking, Corrosion Reviews, 29 (2011) 7-49.

[52] M. Gell, P.J. Worthington, The plastic deformation and fracture of Iron-3% Silicon in the temperature range 295°K–473°K, Acta Metallurgica, 14 (1966) 1265-1271.

[53] J.T. Barnby, The initiation of ductile failure by fractured carbides in an austenitic stainless steel, Acta Metallurgica, 15 (1967) 903-909.

7. Stress Corrosion Cracking of Thermal Treated Type 310S Stainless Steel in Supercritical Water

Y. Jiao, W. Zheng, J. Kish. Stress corrosion cracking susceptibility of thermally-aged Type 310S stainless steels in supercritical water, revised manuscript (minor revisions) submitted to Corrosion Science, December 2017.

7.1 Introduction

This chapter presents a draft article (not yet submitted for publication), which documents the research conducted to comparatively evaluate the intergranular SCC susceptibility of the two limiting thermally-aged Type 310S stainless steel conditions relative to the baseline in SCW. This article is the final of three that, as a set, specifically address the SCC implications of both short-term and long-term thermally-aged microstructures in SCW described in Section 1.2 above and in the Stress Corrosion Cracking Implications Section in Chapter 3. The results of SSRT measurements in 25 MPa SCW at 500 °C in combination with the post-exposure metallographic examinations were benchmarked against the findings presented of the two previous Chapters to elucidate key factors that likely control the intergranular SCC susceptibility of austenitic stainless steel exposed in SCW.

Prof. Kish at McMaster University and Prof. Zheng at CanmetMATERIALS are my supervisors. They were giving me guidance, instruction and edit manuscript. I was responsible for conceiving the research questions, collecting and analyzing the data, and writing the manuscripts. The study was approved by the McMaster Research Ethics Board at McMaster University (Hamilton, Ontario).

7.2 Key Factors Affect SCC Susceptibility

Design of advanced nuclear power plants with high energy efficiency are being planned for future deployment. The supercritical water-cooled reactor (SCWR) is an innovative concept that has directly evolved from existing water-cooled reactors [1-7]. In the SCWR concept, the primary coolant is operated above the critical point of water (374 °C, 22.1 MPa) in a direct once-through cycle that enables the elimination of some components, such as steam generators and steam separators and dryers for example. The Canadian SCWR design concept requires a fuel core inlet temperature of 350 °C and outlet temperature of 625 °C at 25 MPa for the SCW coolant, with an associated fuel cladding operating temperature range from 375 °C to 800 °C to achieve the significantly increased thermal efficiency [2, 3, 7]. Such extreme operation environment requires the fuel cladding to possess sufficient integrated material properties including general corrosion resistance, stress corrosion cracking (SCC) resistance, creep resistance, radiation damage resistance, microstructure stability and mechanical strength [1, 2, 4, 5, 7]. Austenitic stainless steels have received tremendous attention as candidate fuel cladding materials for the SCWR design concepts due to their expected combined integrated material performance [1-4, 7].

Type 310S stainless steel has been short-listed as a candidate alloy for the fuel cladding in the Canadian SCWR design concept [2, 7]. The SCC susceptibility of this alloy in the SCW coolant and how it is affected by microstructure instability expected from prolonged exposure to both high temperature and radiation has been identified as a key materials performance knowledge gap that needs addressing [8]. Microstructure instability of austenitic stainless steels resulting from corrosion [9], cold working [10], thermal ageing [11] and/or irradiation [12, 13] has been shown to coincide with a demonstrated intergranular SCC susceptibility when tested in SCW. Thus, tendency for grain boundaries to preferentially corrode/oxidize and/or mechanically embrittle plays a key role in the overall cracking process. The formation of Cr-rich $M_{23}C_6$ carbides on grain boundaries and the concomitant development of Cr-depleted zone from either prior thermal ageing [11, 14, 15] or long term immersion in SCW [16] has been identified as a key contributing factor, which suggests a strong preferential corrosion/oxidation effect. Alternatively, the degree of plastic deformation from either prior cold-working [7] or acquired during straining whilst immersed in SCW [7] has been identified as the key contributing factor, which suggests strong mechanical embrittlement effect. The understanding is further muddled when considering the increased intergranular SCC severity exhibited by pre-irradiated (protons) austenitic stainless steel when tested in SCW has been correlated with both a contaminant increase in radiation-induced segregation (RIS) (corrosion effect) and hardening (embrittlement effect) [8]. These initial findings are consistent with the well-documented SCC susceptibility of austenitic stainless steel in current generation light water nuclear reactors, which typically occurs via an intergranular process [5, 6, 12, 17-19]. The key contributing factors affecting intergranular SCC are also Cr depletion at the grain boundaries resulting from RIS and hardening resulting from irradiation and/or cold working [12, 17, 20], yet neither factor can control alone [12, 17, 20].

Given the in-service life expected of the fuel cladding (~30,000 h) [2, 7], the Type 310S stainless steel microstructure will be unstable at the higher cladding temperatures as precipitation of secondary phases will occur on grain boundaries and within the matrix grains [11, 15, 21-24]. Cr-rich carbides [11, 15, 21-23] and the sigma (σ) phase [11, 15, 21-23] are the main types of precipitates that are expected to form from thermal ageing. Formation of Cr-rich carbides ($M_{23}C_6$ type) precipitates within an intermediate temperature range (~ 450-750 °C) typically coincides with formation of adjacent Cr-depleted zones after short exposure times [15, 25], which serve to increase intergranular SCC susceptibility in aqueous environments [12, 18, 26, 27]. The Cr-rich σ phase, as an intermetallic precipitate, is brittle with significantly increased hardness compared with the austenite matrix [23, 24, 28-30]. Similar to $M_{23}C_6$ carbide precipitate formation, σ phase precipitate formation can also be accompanied by adjacent Cr-depleted zone formation, which gain serve to increase intergranular SCC susceptibility in aqueous environments [25, 28, 31]. Formation of σ phase precipitates at elevated temperature can also coincide with adjacent void formation [29] that adversely affects the mechanical properties (reducing ductility in particular) [11, 23, 24, 28, 30]. Prolonged thermal ageing is expected to help 'self-heal' microstructure instability in part by eliminating Cr-depleted zones via bulk diffusion of Cr from the matrix into the depleted zone [15, 25]. Eliminating Cr-depleted zones adjacent to grain boundaries is well known to decrease intergranular SCC susceptibility in simulated light water reactor environments [12, 13, 32-34]. However, simultaneous exposure to radiation may serve to maintain the Cr-depleted zones formed from thermal ageing via RIS [12, 18-20, 27].

The goal of this study was to assess the effect of limiting thermal ageing extents on the SCC susceptibility of Type 310S stainless steel in SCW. Slow strain rate testing (SSRT) in flowing (200 mL/min.) 25 MPa SCW at 500 °C with 20 ppm dissolved oxygen was used for this purpose. Test samples were thermally-aged to two limiting extents and compared relative to a solution-annealed condition, which represented an ideal starting microstructure baseline. The limiting extents consisted of a short-term thermal aging treatment to 'sensitize' the microstructure by forming Cr-rich $M_{23}C_6$ precipitates on the grain boundaries and adjacent Cr-depleted zones and a long-term thermal ageing treatment to 'embrittle' the microstructure by forming σ phase precipitates on the grain boundaries. As a 'first approximation', these limiting thermal ageing extents, relative to solution annealed baseline, served to help de-couple preferential grain boundary corrosion/oxidation and grain boundary embrittlement factors from one another for an isolated assessment. In one related study [35], we confirmed that the limiting sensitized material exhibited the highest relative degree of sensitization and associated intergranular IGSCC susceptibility (as measured by slow strain rate testing (SSRT) in a hot alkaline solution), which reflects the controlling role played by Cr-depleted zones. In another related study [36], we confirmed that the grain boundaries in the limiting 'sensitized' material were sufficiently embrittled to cause intergranular fracture, whereas the grain boundaries in the limiting 'embrittled' material were not sufficiently so. Based on our reported findings, the limiting 'embrittled' microstructure (long term thermal-ageing) may have an unanticipated beneficial effect on the intergranular SCC susceptibility of Type 310S stainless steel exposed in SCW coolant.

7.3 Experimental Methods

Test samples were prepared from commercial Type 310S stainless steel rod product (25.6 mm diameter) provided in the mill-annealed (MA) condition. The chemical composition as specified in the Mill Test Report is listed in Table 7.1. Sub-sections of the rod product were solution-annealed (SA), sensitized (S) or thermally-treated (TT) prior to preparing test samples. The SA treatment was conducted at 1050 °C for 1 h, followed by water-quenching to yield an ideal microstructure: one that would exhibit a low degree of sensitization and precipitate-induced grain boundary embrittlement. The S treatment was conducted at 650°C for 100 h, followed by air-cooling to yield a classic sensitized microstructure with significant $M_{23}C_6$ carbide precipitation on the grain boundaries concomitant with the development of adjacent Cr-depleted zones. The TT treatment was conducted at 800°C for 1000 h, followed by air-cooling to yield a degraded microstructure with significant σ phase precipitation on the grain boundaries and within the grains. This treatment was intended to represent a long-term exposure of the fuel cladding at the maximum cladding temperature expected in the Canadian SCWR design concept (800 °C) [2]. It was expected to, and indeed achieved, σ phase precipitate formation on grain boundaries without any associated Cr-depleted zone formation, which yielded a microstructure with a low degree of sensitization yet a high degree of grain boundary embrittlement. The characterization of pre-treated microstructure was reported in previous work [37]. Table 7.2 summaries the major precipitates that were found both on the grain boundaries and with the grains using electron microscopy [38]. Figure 7.1 shows a set of light optical images of the starting microstructures of the limiting thermally-aged material along with the SA baseline material.

Table 7.1 Chemical composition (wt.%) of the Type 310S stainless steel used in this work.

Cr	**Ni**	**Mo**	**Mn**	**Si**	**P**	**S**	**C**	**Fe**
24.3	19.56	0.29	0.96	0.76	0.04	0.04	0.06	Bal.

Table 7.2 Summary of precipitates confirmation by electron microscopy.

Material	SEM-EDS		TEM-EDS	
	GB	Grain	GB	Grain
SA	$M_{23}C_6$	-	$M_{23}C_6$	-
S	$M_{23}C_6$	$M_{23}C_6$	$M_{23}C_6$	$M_{23}C_6$
TT	σ	σ	σ	$M_{23}C_6$ + σ

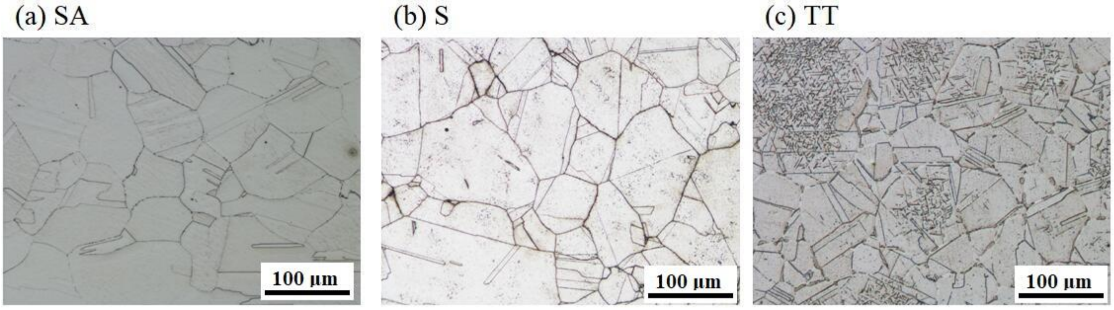

Figure 7.1 Standard light microscopy image showing the typical appearance of the heat-treated microstructure: (a) SA material, (b) S material and (c) TT material.

SSRT samples were machined from SA, S and TT material with the longitudinal axis oriented along the longitudinal direction of the rod product. The gauge length of each cylindrical sample was 14 mm and the gauge diameter was 6 mm. Figure 7.2 shows a dimensioned drawing of the SSRT sample. The gauge length was manually mechanically-abraded to a 1200 grit finish using SiC paper and water as a lubricant. A final abrasion finish (1200 grit) was applied manually along the longitudinal direction. The samples were then rinsed with distilled water, ultrasonically rinsed in acetone and allowed to dry prior to each test. SSRT was conducted in 25 MPa SCW at 500 °C with 20 ppm dissolved oxygen in an autoclave flow loop (200 mL/min.) facility. A triplicate set of SSRT samples were strained to 5% initially (about 2.5% plastic strain) and a second set of singular SSRT samples were strained to 10% (about 7.5% plastic strain) at a strain rate of 3×10^{-7} s^{-1}. The latter was necessary since crack indications were not observed on any of the triplicate SSRT samples strained to 5%. There was a malfunction with the data acquisition software when straining the SA sample 10% and that load–displacement data was not saved for that particular sample. However, the sample was indeed strained to 10%.

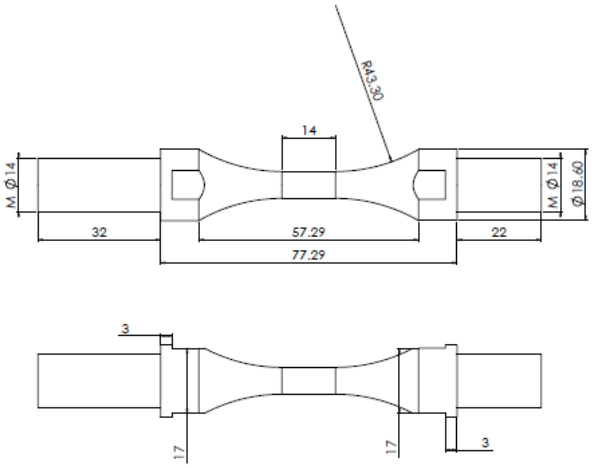

Figure 7.2 Dimensional drawing of the SSRT samples used in this study: dimensions are given in mm).

After straining, one half of the gauge length on each sample was descaled, mounted in cross-section and then imaged using scanning electron microscopy (SEM) to reveal the mode and extent of SCC in terms of the crack density and nominal crack growth rate. Details pertaining to the descaling procedure have been published elsewhere [3]. SEM imaging was performed using a JEOL JSM-7000F microscope equipped with a Schottky Field Emission Gun (FEG) filament and an integrated Oxford Synergy system with INCA EDS X-ray micro-analysis. Images were acquired using an accelerating voltage of 10 kV and a working distance of 10 mm.

Site-specific cross-sectional thin foils for subsequent examination by transmission electron microscopy (TEM) and associated techniques were extracted from cracked and intact grain boundaries using a dual focused ion beam (FIB)/SEM platform (Zeiss NVision 40) operated with a gallium (Ga) ion beam voltage of 30 k, a current beam of 80 pA and a working distance of 5.6-5.9 mm. A tungsten (W) strap (2 μm thick) was deposited on the plan-view surface to protect the oxide scale during ion milling. The TEM examination was conducted using the JEOL 2010F TEM/STEM equipped with an Oxford Instruments X-ray energy dispersive spectroscopy (EDS). Images and EDS elemental line scans were acquired using an accelerating voltage of 200 kV with a point-to-point resolution of 0.23 nm. Selected area diffraction (SAD) patterns were obtained from sites of interest and were compared to those of expected phases that were created using the JEMS software [31] and published reference diffraction patterns [32]. All imaging and EDS lines scans were acquired using the bright-field (BF) scanning TEM (STEM) mode.

7.4 Results

The engineering stress (σ)-strain (ε) curves of the Type 310S stainless steel SSRT samples strained to 5% (Figure 7.3a) and 10% (Figure 7.3b) strain in the flowing 25 MPa SCW at 500 °C with 20 ppm dissolved oxygen are shown in Figure 7.3. Only one curve is shown for each material in Figure 7.3a as the triplicate set of testing showed excellent reproducibility. As expected, neither strain extent was sufficient to cause fracture of the SSRT sample, regardless of the pre-heat treatment applied. Qualitatively speaking, the S material exhibited a slightly higher yield strength (σ_y) than the SA material, but a similar working hardening rate ($d\sigma/d\varepsilon$). This is consistent with the reported effect that $M_{23}C_6$ precipitate formation has on the uniaxial tensile properties of thermally aged Type 310S stainless steel measured at room temperature [36]. In contrast, the TT material exhibited a significantly higher yield strength (σ_y) and work hardening rate ($d\sigma/d\varepsilon$) than the S and SA material. This is also consistent with the reported effect that σ phase precipitate formation has on the uniaxial tensile properties of thermally-aged Type 310S stainless steel measured at room temperature [36].

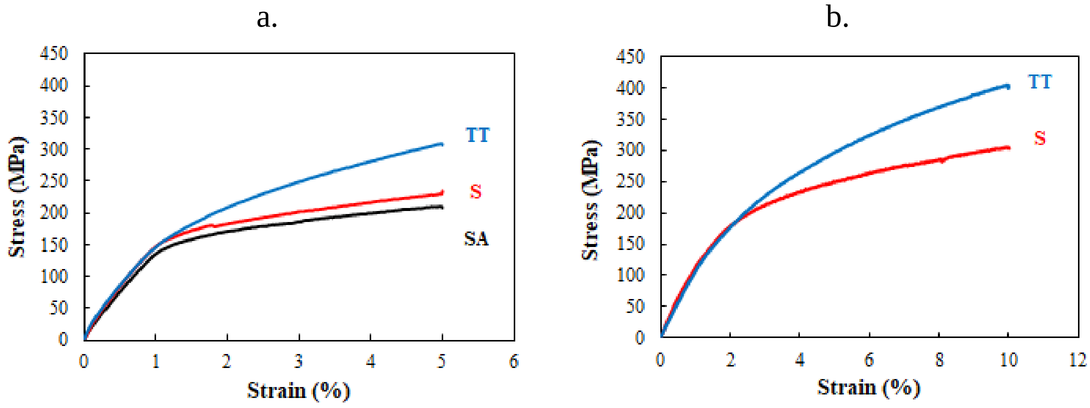

Figure 7.3 Stress-strain curves of the SSRT samples strained to (a) 5% and (b) 10% in flowing 25 MPa SCW at 500 °C with 20 ppm dissolved oxygen.

A set of plan-view and cross-sectional view secondary electron images of the descaled gauge length surfaces of the SA, S and TT samples after straining to 5% in the SCW environment are shown in Figure 7.4. Crack indications were not observed in any of the SSRT samples. The dominant features in the plan view image of the SA sample (Figure 7.4a) and the S sample (Figure 7.4b) were the horizontally-aligned mechanical-abrasion grooves visible along uniaxial tensile axis (longitudinal direction of the rod product). In contrast, intact σ phase precipitates were clearly visible along with the mechanical abrasion grooves on the surface of the TT sample (Figure 7.4c). The σ phase precipitates were intact, without any visible evidence of preferential cracking. The set of cross-sectional images (Figure 7.4d-f) reveals a surface free of incipient crack initiation in either the exposed surface grains or grain boundaries. As no evidence of any SCC in the SSRT samples strained to 5% was found, a set of singular SSRT samples was strained to 10% in the SCW environment.

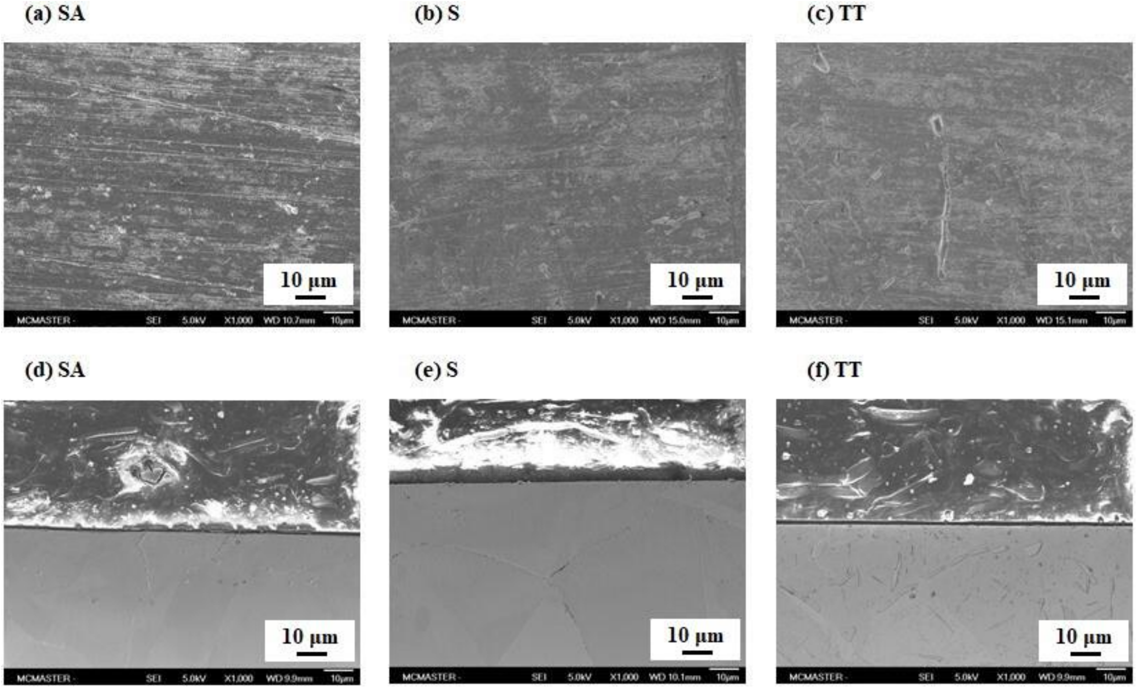

Figure 7.4 SEM images of the SSRT samples after straining to 5% in flowing 25 MPa SCW at 500 °C with 20 ppm dissolved oxygen. Plan view images of the descaled gauge length surfaces: SA sample (b) S sample and (c) TT sample. Associated set of cross-sectional images: (d) SA sample, (e) S sample and (f) TT sample.

Figure 7.5a to 7.5c shows a set of plan-view secondary electron images of the descaled gauge length surfaces of the SA, S and TT samples respectively after straining to 10%. Grain boundary crack indications were observed on the gauge length surface of the SA samples (Figure 7.5a) and the S sample (Figure 7.5b). The roughened surface regions on both images are likely corrosion/oxidation-induced, as revealed by descaling. Similar crack indications were not observed on the gauge length surface of the TT sample (Figure 7.5c). However, preferential cracking of σ phase precipices was observed, as indicted by the arrow. A mechanical abrasion groove traversing a grain boundary on the surface of the SA samples is clearly visible in Figure 7.5a (indicated by dashed line). The groove in no way appears be offset as it traverses across the grain boundary. Similar pre-existing scratch lines have been used with success to verify the occurrence of grain boundary sliding during high temperature deformation, as the pre-existing scratch line will be offset if it traverses a grain boundary that slides [39]. A cursory look at random grooves traversing grain boundaries in the SA, S and TT material provided no compelling evidence that grain boundary sliding occurred during the high temperature deformation.

The opportunity was taken prepare cross-sectional trenches using FIB milling prior to destructively sectioning the SSRT samples for a full cross-sectional examination of the gauge length. A secondary electron image of the milled cross-section through a crack indication in the SA sample and in the S sample is shown in Figure 7.5d and 7.5e respectively. A similar image of the milled cross-section through a σ phase precipitate intersecting the surface is shown in Figure 7.5f. The cracks in both the SA sample (Figure 7.6a) and S sample (Figure 7.6b) were sharp, unbranched, filled with corrosion product and definitely intergranular. The intergranular crack happened to be more developed in the S sample than the SA sample in this comparison. The relatively large σ phase precipitate in the TT sample, demarked by the dashed frames, was located on a grain boundary. The precipitate had preferentially cracked in several locations. Localized deformation in the form of a dislocation channel/slip band terminating at grain boundaries was visible in each of the three samples, consistent with straining being conducted into the plastic zone.

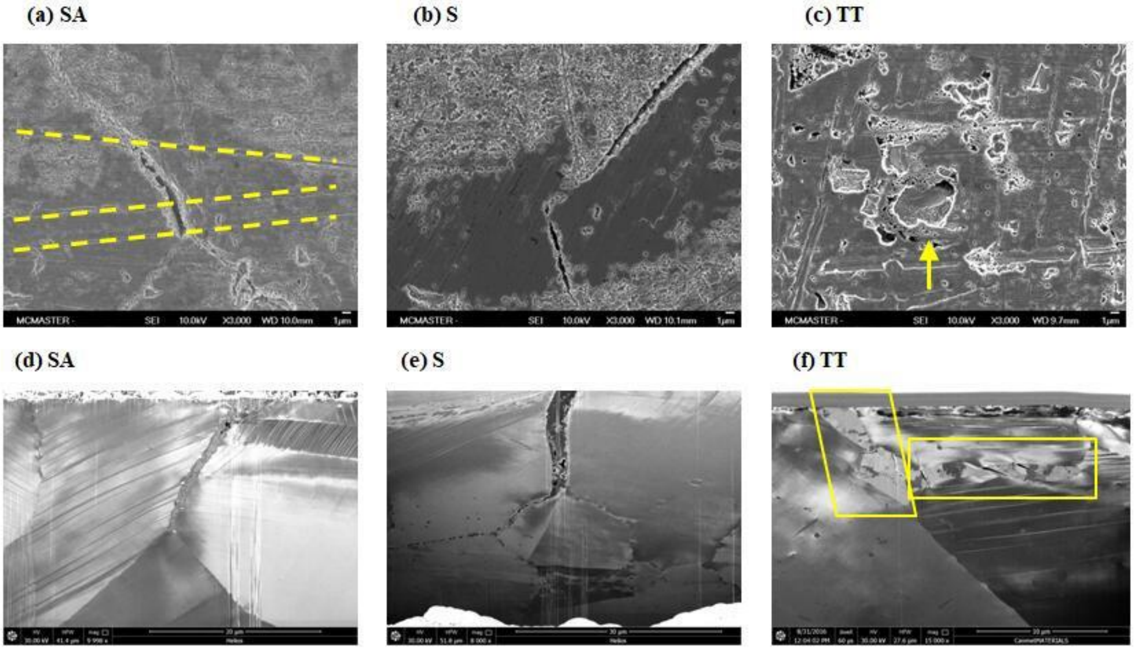

Figure 7.5 Plan view SEM images of the SSRT sample descaled gauge length surfaces after straining to 10% in flowing 25 MPa SCW at 500 °C with 20 ppm dissolved oxygen: (a) SA sample (b) S sample and (c) TT sample. Associated set of (FIB-prepared) cross-sectional images: (d) SA sample, (e) S sample and (f) TT sample. Dashed lines in (a) demark mechanical abrasion grooves. Arrow in (c) demarks cracked σ phase precipitate in plan view. Frames in (f) demark cracked σ phase precipitate in cross-sectional view.

Figure 7.6 shows cross-sectional view images of the gauge length of the SA, S and TT samples after straining to 10%. The cross-sections of the SA sample and the S sample were taken through a crack indication site, as revealed by the plan-view imaging. The cracks in both the SA sample (Figure 7.6a) and S sample (Figure 7.6b) here too were sharp, unbranched and sufficiently developed, having propagated up to 57 μm and 45 μm into the SA sample and the S sample respectively. In contrast, crack indications were not observed in the TT sample (Figure 7.6c). Higher magnification images reveal that the cracking mode was intergranular in both the SA sample (Figure 7.6d) and the S sample (Figure 7.6e). The grain boundary cracks were filled with corrosion product and significant micro-void formation was visible on the grain boundary ahead of the advancing crack tip in samples. Micro-void formation on the grain boundaries in both samples was associated with adjacent grain boundary precipitates (presumably $M_{23}C_6$ in both cases). Micro-void formation was restricted to only those grain boundaries that had cracked and to only a distant of about 20-30 μm ahead of the crack tip. The extent of precipitate formation ahead of the cracked grain boundary in the SA material was comparable to that observed ahead of the cracked grain boundary in the S material. This suggests that the exposure conditions in the SCW environment may have been sufficient to sensitize the SA material in-situ (about 100 h continuous training at 500°C in the SCW environment). The STEM-EDS data described later confirms the in-situ sensitization. Significant internal preferential cracking of the σ phase precipitates was again observed in the TT sample under higher magnification imaging (Figure 7.6f). No evidence of any linking up of the preferential σ phase cracking form a crack (transgranular or intergranular) was found despite preferential cracking of the grain boundary σ phase precipitates.

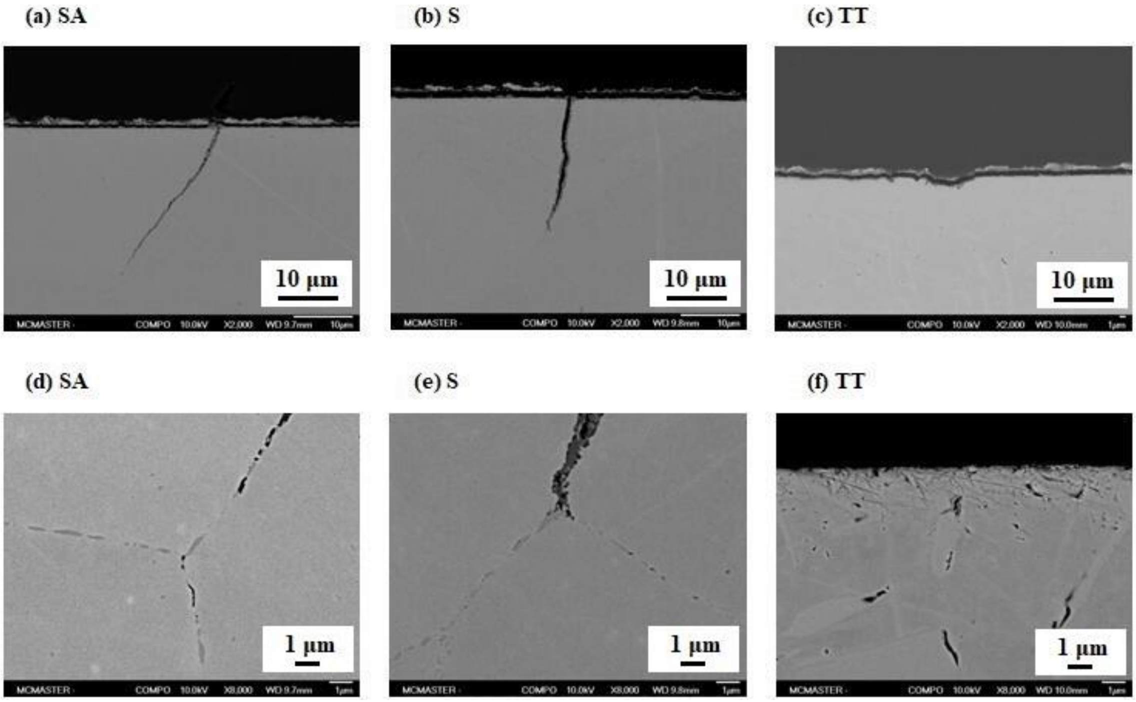

Figure 7.6 SEM images of cross-sectional view of the SSRT samples after straining to 10% in flowing 25 MPa SCW at 500 °C with 20 ppm dissolved oxygen. Low magnification images: (a) SA sample, (b) S sample and (c) TT sample. Associated set of high magnification images: (d) SA sample, (e) S sample and (f) TT sample.

Table 7.3 summaries the mode and extent of SCC in terms of the crack density and nominal crack growth rate that occurred during straining to 10% in the SCW environment. Crack depth along with crack density on the gage length [40-42] and % intergranular cracking on the fracture surface [43-45] parameters have been used as an indicator of intergranular SCC susceptibility. Unfortunately, these measures are not always in agreement [42] as crack density is more sensitive to small cracks and, therefore more sensitive to crack initiation. It has been suggested that crack initiation and propagation be separated when analyzing SCC susceptibility [46]. Following this, Table 7.3 considers crack density (number of cracks/unit area) to capture crack initiation and nominal crack growth rate (deepest crack/exposure time) to capture crack propagation. Crack density statistics for each sample were extracted from a set of 12 images encompassing a total area about 1.5 mm^2. The nominal crack growth rate was determined using the deepest crack among a set of about 20 cracks found over a 6 mm gage length. Considering the semi-quantitative nature of the analysis, there is likely no significant difference between the SA sample and the S sample in terms of both crack initiation and propagation. The predominant takeaways from Table 3 include: (i) S material exhibited a similar intergranular SCC as the SA material despite having well-developed Cr-depleted zones formed adjacent to grain boundaries in the starting microstructure (in contrast to the SA material, which did not) and (ii) TT material exhibited a significantly lower intergranular SCC susceptibility (no susceptibility in this test) than both the S material and SA material despite having preferential cracked σ phase precipitates located on grain boundaries.

Table 7.3 Summary of cracking statistics extracted from the SEM imaging.

Material	Crack Initiation (Plan View)	Crack Propagation (Cross-Section)	
	Density(#/mm^2)	Max. Depth (μm)	Growth Rate (μm/s)
SA	63	57	1.68×10^{-4}
S	87	45	1.33×10^{-4}
TT	0	0	0

Figure 7.7a shows a BF-STEM image of an intact grain boundary in the SA sample strained to 10% in the SCW environment. Localized deformation in the form of a dislocation channel/slip band (arrows) terminating at the intact grain boundary (dashed line) along with localized regions relatively high dislocation density was visible. The localized bright region located on the intact grain boundary itself (frame) is a void. The void is likely a micro-void formed during straining and likely has been enlarged to a certain extent by the FIB milling sample preparation sequence. Figure 7.7b shows a high angle annular dark-field (HAADF) image of the void region at higher magnification. The void is clearly associated with a precipitate, as demarked by the frame. An associated set of EDS maps for O, Fe, Cr and Ni is shown in Figure 7.7c to 7.7f respectively. A scale rich in Fe, Cr and O was present on the boldly exposed gauge length surface. Precipitates enriched in Cr but depleted in both Fe and Ni were found to decorate the grain boundary.

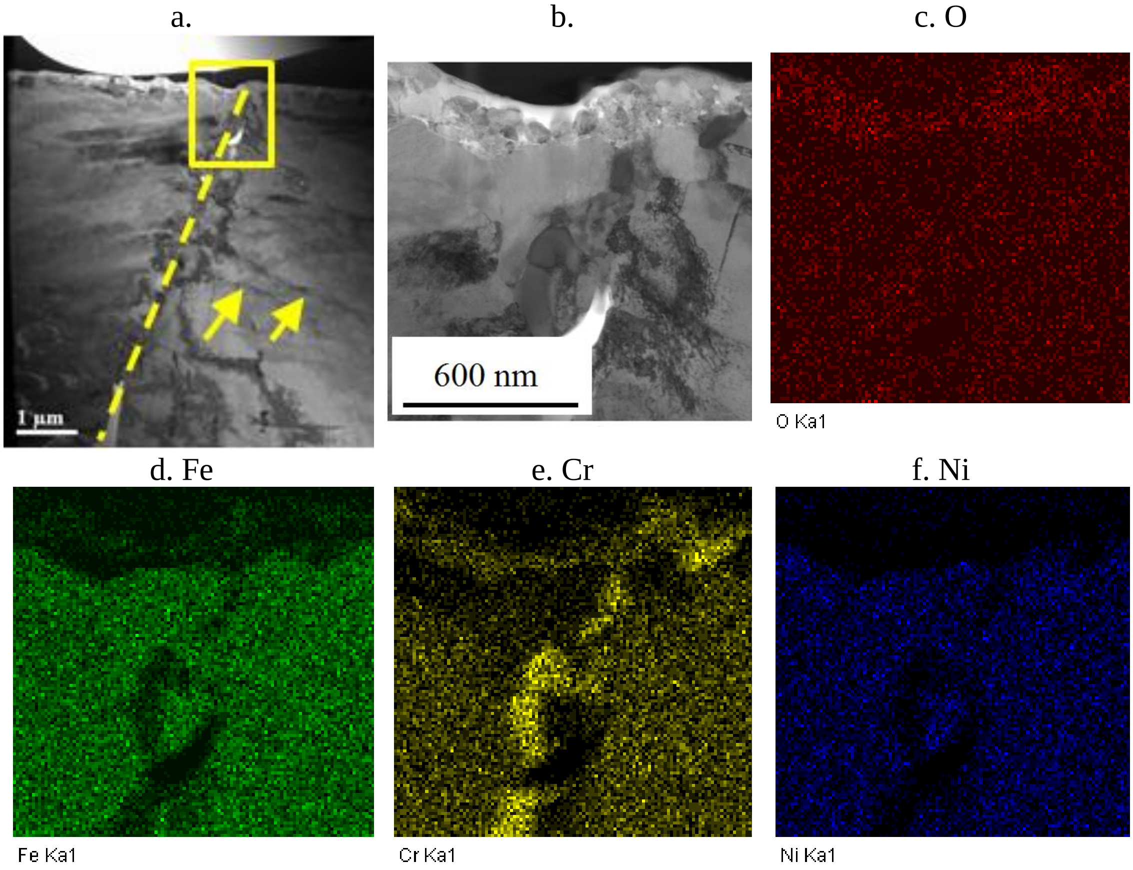
a. b. c. O

d. Fe e. Cr f. Ni

Figure 7.7 HAADF images of the FIB prepared cross-section foil of an intact grain boundary in the SA sample (a) and (b) and the associated set of EDS maps for (c) O, (d) Fe, (e) Cr and (f) Ni.

Figures 7.8, 7.9 and 7.10 show a similar set of images and EDS maps as Figure 7.7, but for cracked grain boundary in the SA sample, an intact grain boundary in the S sample and a cracked grain boundary in the S sample respectively. The HAADF image and the associated EDS maps were acquired from the midpoint region of the grain boundary crack in the SA material (Figure 8b) and from the crack tip region of the grain boundary crack in the S material (Figure 10b). Similar localized deformation features (dislocation channel/slip band (arrows) terminating at the intact grain boundary (dashed line) and localized regions relatively high dislocation density) were visible in the BF-STEM image of the cracked grain boundary in the SA sample (Figure 7.8a) and the intact (Figure 7.9a) and cracked (Figure 7.10a) grain boundary of the S sample. Other notable consistent observations include the presence of a scale rich in Fe, Cr and O on the surface exposed to the SCW environment (crack wall in the case of the cracked grain boundary in the SA and S material) and precipitates enriched in Cr but depleted in both Fe and Ni decorating the grain boundary (intact grain boundary in the SA sample and both the intact and cracked grain boundary in the S sample).

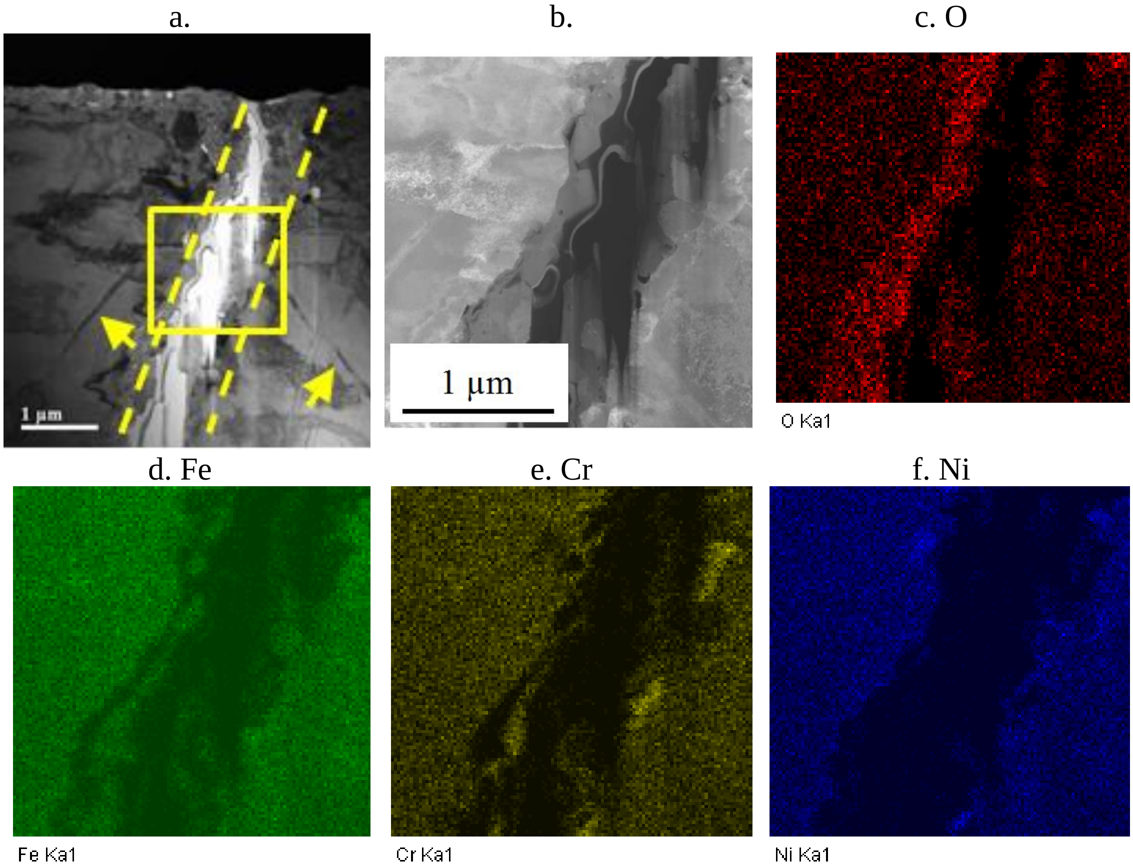

Figure 7.8 HAADF images of the FIB prepared cross-section foil of a cracked grain

boundary in the SA sample (a) and (b) and the associated set of EDS maps for (c) O, (d) Fe, (e) Cr and (f) Ni.

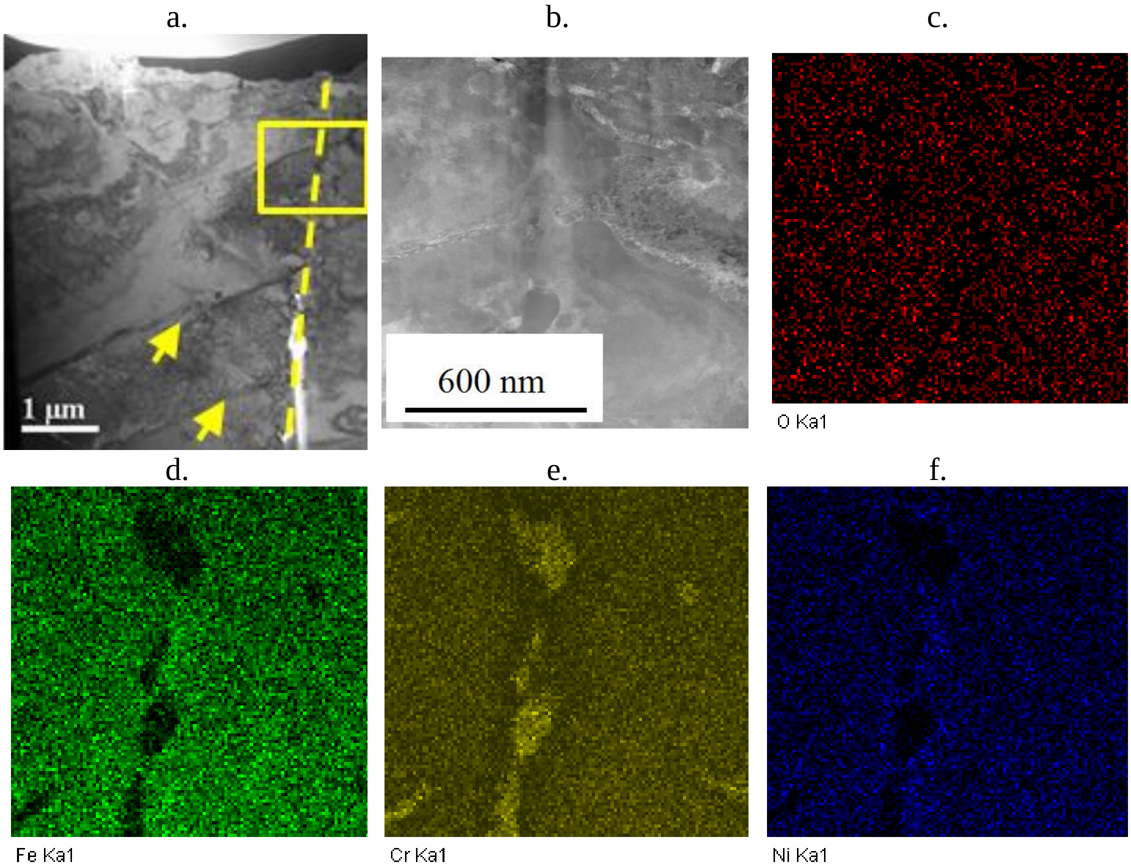

Figure 7.9 HAADF images of the FIB prepared cross-section foil of an intact grain boundary in the S sample (a) and (b) and the associated set of EDS maps for (c) O, (d) Fe, (e) Cr and (f) Ni.

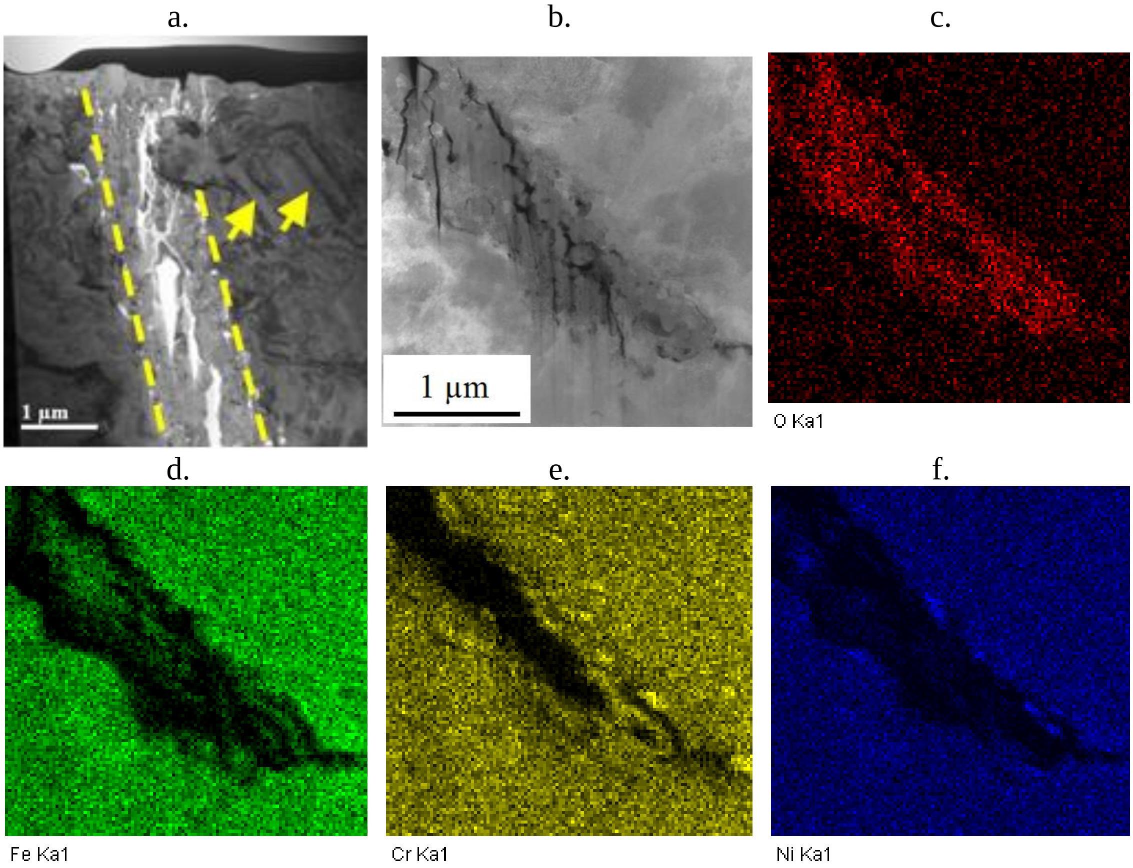

Figure 7.10 HAADF images of the FIB prepared cross-section foil of a cracked grain boundary in the S sample (a) and (b) and the associated set of EDS maps for (c) O, (d) Fe, (e) Cr and (f) Ni.

As mentioned above, the observation of significant Cr-rich precipitate decoration of the grain boundaries in the SA material suggests that the exposure conditions in the SCW environment may have been sufficient to sensitize the SA material in-situ (about 100 h continuous training at 500°C in the SCW environment). Figure 7.11 shows a HAADF image (Figure 7.11a) of a Cr-rich grain boundary precipitates in the SA sample along with a set of EDS lines profiles for C, Fe, Cr and Ni (Figure 11b) corresponding to the line superimposed on the HAADF image. Each of the three precipitates included in the scan were enriched in C and Cr and depleted in Fe and Ni relative to the matrix. Furthermore, the regions between the precipitates were depleted in Cr and enriched in Fe and Ni relative to the matrix. Thus, Cr depleted zones adjacent to grain boundary Cr-rich carbide precipitates did indeed form in-situ during the 10% straining in the SCW environment. It follows then that the SA samples would behave more like the S samples with increasing exposure time during SSRT in the SCW environment. The summary of the cracking observations listed in Table 3 indicates this is so.

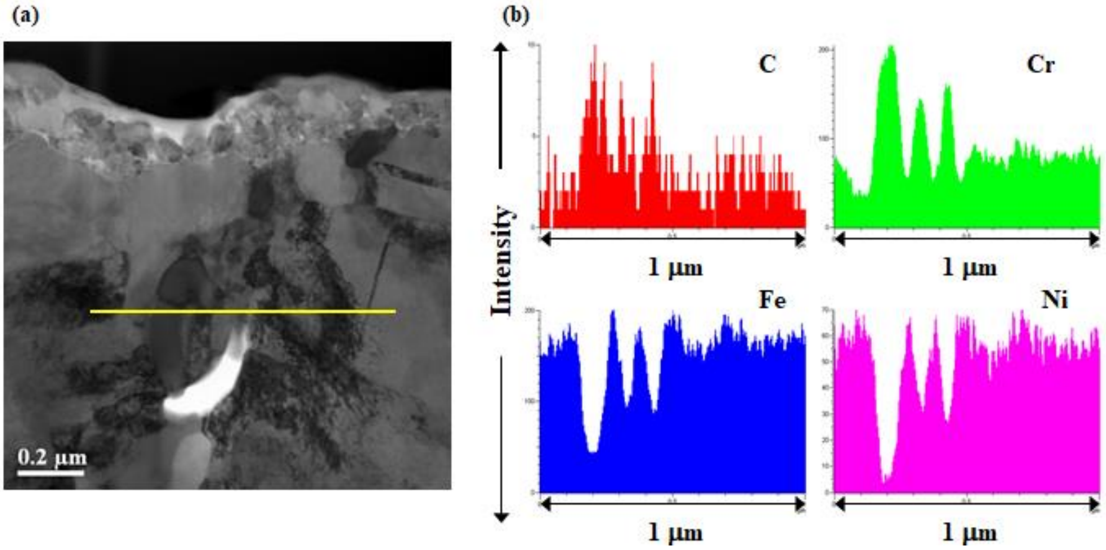

Figure 7.11 (a) HAADF image of FIB prepared cross-section foil of an intact grain boundary in the SA sample and (b) associated set of EDS line scans for O, Fe, Cr and Ni.

7.5 Discussion

The goal of this study was to assess the effect of limiting thermal ageing extents on the SCC susceptibility of Type 310S stainless steel in SCW relative to a solution annealed (SA) condition. Despite the SA samples becoming sensitized in situ during exposure to the SCW environment (Figure 7.11), the relative differences in susceptibility exhibited by sensitized (S and SA) samples relative to the TT samples provide some much needed insight into how thermally ageing (microstructure instability in general) can be expected to affect SCC susceptibility over the expected service life of a Type 310S stainless steel fuel cladding. As discussed, the relative differences in susceptibility, as highlighted in Table 7.3 can be rationalized within the mechanistic framework established for the intergranular SCC of irradiated authentic stainless steels in LWR environments.

7.5.1 SCC Initiation

The cross-sectional examinations of the SA, S and TT samples clearly showed that a relatively large number of slip lines/dislocation channels formed in each during straining to 10%. Slip is a common deformation mode for polycrystalline materials [47]. For irradiated alloys, the moving dislocations initially remove defects on the slip plane/channel by either annihilating or combining with the defects to facilitate and confine subsequent dislocations motion along the same path [12, 39, 47, 48]. An important consequence is that the localized stress accumulated in plane/channels could be up to one order of magnitude larger than the bulk applied stress, whereas the material between planes/channels remains undeformed [12, 39, 47, 48]. Slip planes/channels have been observed in both irradiated [12, 39, 47-50] and unirradiated

[13] materials and tend to be more widely spaced in irradiated alloys [12, 39, 47-50]. The interaction between slip planes/ channels and grain boundaries may result in large amount of localized deformation [12, 39, 48]. This localized deformation tendency is believed to be a contributing factor in the initiation of intergranular SCC of stainless steels in LWR environments [12, 48-50] and SCWR environments [26]. The model essentially involves the accumulation of stress at grain boundaries resulting from the interactions with slip lines/channels during mechanical deformation. When sufficiently large, the accumulated stress can rupture the protective oxide film at the surface, thereby initiating an intergranular crack.

It follows from the localized deformation crack initiation model that any mechanism that can help prevent stress accumulation at the grain boundaries should be beneficial in reducing intergranular SCC susceptibility. We think the preferential cracking of the coarse σ phase grain boundary precipitates in TT serves this purpose, as an intergranular SCC susceptibility was not observed in this study, whereas it was observed in the sensitized material without preferential cracking of the fine $M_{23}C_6$ grain boundary precipitates. Localized deformation is affected by presence of secondary phase particles on the grain boundary as they can block transmission of the slip plane/channel across the boundary [51, 52]. The resulting localized stress accumulation caused by blocking may be sufficient high to cause preferential cracking of the blocking particle, depending upon the hardness and size of the particle among other factors [51]. The strain partitioning around hard coarse-scale, opposed to fine-scale, precipitates tends be more uniform [53]. As the bonding strength between coarse hard σ phase precipitate and the matrix in austenitic stainless steels is typically strong enough to avoid decohesion of precipitate/matrix interface, but brittle enough to preferentially crack during plastic deformation [51, 52] as the local stress exceeds the fracture stress. This is exactly what we observe for the coarse σ phase grain boundary precipices in the TT samples strained to 10%. Such preferential cracking is believed to relieve the localized stress accumulation at the boundary, which is necessary for the localized deformation induced SCC initiation. On the other hand, strain partitioning around hard fine-scale $M_{23}C_6$ grain boundary precipitates in austenitic stainless steel typically results in decohesion of the precipitate/matrix, rather than preferentially cracking [54]. Decohesion occurs if either the normal stress at the interface exceeds the critical fracture stress or the strain energy stored during plastic deformation exceeds the energy of the new surfaces formed by cavitation [54]. Although we observed void formation (an alternative localized stress relief mechanism) the sensitized (SA and S) samples, they were only observed immediately ahead of the propagating crack. In other words, void formation in the SA and S samples occurred locally (within 20-30 μm from the surface), whereas preferred cracking of the coarse σ phase grain boundary precipices occurred globally.

7.5.2 SCC Propagation

Void formation ahead of the crack tips in the sensitized (SA and S) samples suggests that it has a contributing role in propagating SCC along the grain boundaries. Given the SSRT conditions used, such void formation could have been induced from either deformation-induced precipitate/matrix decohesion (described above) or high temperature creep (deformation-induced vacancy formation and strain gradient-induced diffusion to and coalescence at precipitates). In fact, creep has been proposed to have a contributing role in the intergranular SCC of stainless steels in both LWR environments [55, 56] and, more recently, SCW environments [57]. Building upon the film-cleavage model [58-60] a creep extension model was proposed to explain the intergranular SCC of cold worked (30%) Alloy 690 in SCW [57]. The model involves the oxide scale at the crack tip being ruptured by dislocation movement at the crack tip, which exposes bare metal at the crack tip to SCW, with crack propagation by both subsequent bare metal oxidation and vacancy incorporation before an intact oxide scale forms again, and the process repeats. Vacancy formation on the grain boundaries in that case was attributed to strain-gradient assisted deformation-induced vacancy diffusion ahead of the crack tip.

A similar mechanism is believed to be responsible for the intergranular crack propagation in sensitized Type 310S stainless steel exposed to SCW reported in this study, as oxide scale formation at the crack tip was observed along with void formation on grain boundaries ahead of the crack tip. However, the void formation observed in the sensitized Type 310S stainless steel is believed to be caused by deformation-induced precipitate/matrix decohesion rather than high temperature creep. The creep extension model described above was developed to explain observations from both creep testing and SCC testing of compact tension (CT) testing of significantly cold worked Alloy 690 samples. The initial stress intensity factor (K) of 25 MPa√m combined with 30% cold worked starting material provided conditions that were favorable for deformation induced vacancy formation and strain-gradient diffusion to grain boundaries ahead of a crack tip. It may be possible that initially large and rising K value of the CT samples during both creep and SCC testing of the cold worked Alloy 690 dominated the crack propagation, yielding a similar morphology and crack growth rate as a consequence of minimizing the SCW corrosion contribution to the SCC process. However, we showed through micro-mechanical testing of grain boundary cantilever beams at room temperature that void formation from precipitate/matrix decohesion on the grain boundary of sensitized Type 310S stainless steel occurs well before the onset of plastic instability [36]. Moreover, intergranular cracks were not observed on stainless steel SSRT samples strained to various extents of plastic deformation in air or inert gas at temperatures relevant to SCWR design concepts [7], suggesting the SCW environment is necessary for SCC. Further research is certainly necessary to develop the void-assisted film-cleavage model proposed with particular attention placed on the void formation mechanism.

7.5.3 Implications

The intergranular SCC susceptibility in the SCW environment exhibited by the sensitized (SA and S) material in the SCW environment suggests that the risk for SCC of a Type 310S stainless steel fuel cladding will likely be high under those temperature and time combinations that lead to the development of $M_{23}C_6$ grain boundary precipitation and concomitant Cr-depleted zone formation. Based on published sensitization data for Type 310 stainless steel, this would include a cladding temperature range of 600 °C to 800 °C for an exposure time up to 100 h [15]. However, as the results reported herein show, an exposure time of about 100 h at 500°C during the SSRT testing was sufficient to cause sensitization (formation of Cr-depleted zoned adjacent to grain boundaries). Conversely, the lack of SCC susceptibility exhibited by the TT material in the SCW environment suggests that the risk for SCC of a Type 310S stainless steel fuel cladding will likely be low under those temperature and time combinations that lead to the development of coarse σ phase grain boundary precipitation without concomitant Cr-depleted zone formation. Thus, an effective means to mitigate the SCC susceptibility of a Type 310S stainless steel fuel cladding would be replicate the TT condition, in which a coarse hard phase was present on the grain boundaries that would be preferentially cracked under applied loads during service to effectively relieve the localized stress accumulation that is believed to be a contributing factor in the initiation stage (localized deformation model). The more obvious, but likely impractical, means is to thermally-aged the Type 310S fuel cladding to TT condition as a pre-treatment.

Precipitation of grain boundary carbides without concomitant Cr-depleted zone formation is another possible SCC mitigation strategy since the practice has been found to reduce the intergranular SCC resistance of stainless steels in LWR environment [12, 27, 32, 33]. Proposed mechanisms include: (i) carbides releasing Cr on grain boundaries thereby increasing the diffusion flux of Cr to the surface to form protective oxide films [33] and (ii) carbides effectively blocking dislocation movement during grain boundary sliding [27, 32, 33]. The theory here is that the removing the Cr-depleted zone will reduce the tendency for the bare metal exposed at the crack tip during crack propagation via the film-cleavage model since higher Cr contents coincide with lower corrosion/oxidation rates in SCW environments [4, 6]. Possible strategies here included a stabilized version of Type 310S stainless steel, either chemically by alloying with a stronger carbide forming element than Cr or thermally by applying a heat treatment designed to promote $M_{23}C_6$ carbide formation on the grain boundaries without concomitant Cr-depleted zone formation.

7.6 Conclusions

- The SCC susceptibility of thermally-aged Type 310S stainless steel was evaluated in flowing 25 MPa SCW at 500°C with 20 ppm dissolved oxygen using the SSRT technique. The sensitized (SA and S) material exhibited well-developed intergranular SCC after straining to 10% (about 7.5% plastic strain). The TT material exhibited neither an inter-granular nor transgranular SCC susceptibility under the same exposure conditions. The in-situ sensitization of the starting SA material reveals that such microstructure stability can be expected at relative short exposure times (about 100 h) at temperature as low as 500°C.
- The significant difference in SCC susceptibility is believed to be related to the extent of localized deformation that accumulates at the grain boundaries during plastic deformation, which in turn depends upon the size and possibly type of precipitate that is decorating the grain boundaries. In this context, coarse-scale σ phase precipitates (TT material) are more effective than fine-scale $M_{23}C_6$ precipices (SA and S material) in accommodating localized deformation at grain boundaries by preferentially cracking.
- Void formation associated with carbide precipitates was observed on grain boundaries ahead of the crack tip in the sensitized (SA and S) material. The formation process is believed to be involved deformation-induced decohesion of the precipitate/matrix interface rather than a strain gradient assisted diffusion of deformation-induced vacancies.

- The localized deformation model for SCC initiation and a void-assisted film-cleavage model for SCC propagation can be used to explain the SCC susceptibility of thermally-aged Type 310S stainless steel in SCW.

7.7 References:

[1] T.R. Allen, Y. Chen, X. Ren, K. Sridharan, L. Tan, G.S. Was, E. West, D. Guzonas, 5.12 - Material performance in supercritical water, in: R.J.M. Konings (Ed.) Comprehensive nuclear materials, Elsevier, Oxford, 2012, 279-326.

[2] D. Guzonas, R. Novotny, Supercritical water-cooled reactor materials – summary of research and open issues, Prog. Nucl. Energy, 77 (2014) 361-372.

[3] D.A. Guzonas, W.G. Cook, Cycle chemistry and its effect on materials in a supercritical water-cooled reactor: A synthesis of current understanding, Corros. Sci., 65 (2012) 48-66.

[4] X. Ru, R.W. Staehle, Historical experience providing bases for predicting corrosion and stress corrosion in emerging supercritical water nuclear technology: Part 1 - review, Corrosion, 69 (2013) 211-229.

[5] X. Ru, R.W. Staehle, Historical experience providing bases for predicting corrosion and stress corrosion in emerging supercritical water nuclear technology: Part 3-review, Corrosion, 69 (2013) 423-447.

[6] C. Sun, R. Hui, W. Qu, S. Yick, Progress in corrosion resistant materials for

supercritical water reactors, Corros. Sci., 51 (2009) 2508-2523.

[7] W. Zheng, D. Guzonas, K.P. Boyle, J. Li, S. Xu, Materials assessment for the canadian scwr core concept, JOM, 68 (2016) 456-462.

[8] Y. Jiao, W. Zheng, D. Guzonas, J. Kish, Microstructure instability of candidate fuel cladding alloys: Corrosion and stress corrosion cracking implications, JOM, 68 (2016) 485-489.

[9] J.G. Duh, C.J. Wang, Formation and growth morphology of oxidation-induced ferrite layer in Fe-Mn-Al-Cr-C alloys, J. Mater. Sci., 25 (1990) 2063-2070.

[10] R. Bengochea, B. Lopez, I. Gutierrez, Microstructural evolution during the austenite-to-ferrite transformation from deformed austenite, Metall. Mater. Trans. A, 29A (1998) 417-426.

[11] T. Sourmail, Precipitation in creep resistant austenitic stainless steels, Mater. Sci. Technol., 17 (2001) 1-14.

[12] G.S. Was, Y. Ashida, P.L. Andresen, Irradiation-assisted stress corrosion cracking, Corros. Rev., 29 (2011) 7-49.

[13] P.J. Maziasz, C.J. McHargue, Microstructural evolution in annealed austenitic steels during netron irradiation, Int. Mater. Rev., 32 (1987) 190-219.

[14] H. Sidhom, T. Amadou, H. Sahlaoui, C. Braham, Quantitative evaluation of aged AISI 316L stainless steel sensitization to intergranular corrosion: Comparison between microstructural electrochemical and analytical methods, Metall. Mater. Trans. A, 38

(2007) 1269-1280.

[15] S.S.M. Tavares, V. Moura, V.C. da Costa, M.L.R. Ferreira, J.M. Pardal, Microstructural changes and corrosion resistance of aisi 310S steel exposed to 600-800c, Mater. Charact., 60 (2009) 573-578.

[16] J. Li, W. Zheng, S. Penttilä, P. Liu, O.T. Woo, D. Guzonas, Microstructure stability of candidate stainless steels for Gen-IV SCWR fuel cladding application, J. Nucl. Mater., 454 (2014) 7-11.

[17] J.T. Busby, G.S. Was, E.A. Kenik, Isolating the effect of radiation-induced segregation in irradiation-assisted stress corrosion cracking of austenitic stainless steels, J. Nucl. Mater., 302 (2002) 20-40.

[18] S.M. Bruemmer, E.P. Simonen, P.M. Scott, P.L. Andresen, G.S. Was, J.L. Nelson, Radiation-induced material changes and susceptibility to intergranular failure of light-water-reactor core internals, J. Nucl. Mater., 274 (1999) 299-314.

[19] G.S. Was, S.M. Bruemmer, Effects of irradiation on intergranular stress corrosion cracking, J. Nucl. Mater., 216 (1994) 326-347.

[20] J.T. Busby*, M. Sowa, G.S. Was, E.P. Simonen, Post-irradiation annealing of small defect clusters, Philos. Mag., 85 (2005) 609-617.

[21] Y. Jiao, J.R. Kish, G. Steeves, W.G. Cook, W. Zheng, D.A. Guzonas, Effect of thermal pretreatment on the corrosion of stainless steel in flowing supercritical water, J. Nucl. Eng. Radiat. Sci., 2 (2016) 011015.

[22] W. White, I. Le May, Metallographic observations on the formation and occurrence of ferrite, sigma phase, and carbides in austenitic stainless steels: Part i: Studies of AISI type 310 stainless steel, Metallography, 3 (1970) 35-50.

[23] K.H. Lo, C.H. Shek, J.K.L. Lai, Recent developments in stainless steels, Mater. Sci. Eng., R, 65 (2009) 39-104.

[24] B. Weiss, R. Stickler, Phase instabilities during high temperature exposure of 316 austenitic stainless steel, Metall. Trans. A, 3 (1972) 851-866.

[25] A. Kriaa, N. Hamdi, H. Sidhom, Assessment of intergranular corrosion of heat treated austenitic stainless steel (AISI316L grade) by electron microscopy and electrochemical tests, Prot. Met., 44 (2008) 506-513.

[26] R. Zhou, E.A. West, Z. Jiao, G.S. Was, Irradiation-assisted stress corrosion cracking of austenitic alloys in supercritical water, J. Nucl. Mater., 395 (2009) 11-22.

[27] S.M. Bruemmer, G.S. Was, Microstructural and microchemical mechanisms controlling intergranular stress corrosion cracking in light-water-reactor systems, J. Nucl. Mater., 216 (1994) 348-363.

[28] E. Hall, S. Algie, The sigma phase, Metall. Rev., 11 (1966) 61-88.

[29] T. Ohmura, K. Tsuzaki, K. Sawada, K. Kimura, Inhomogeneous nano-mechanical properties in the multi-phase microstructure of long-term aged type 316 stainless steel, J. Mater. Res., 21 (2006) 1229-1236.

[30] M. Pohl, O. Storz, T. Glogowski, Effect of intermetallic precipitations on the

properties of duplex stainless steel, Mater. Charact., 58 (2007) 65-71.

[31] J.K. Shin, H.J. Jang, K.W. Cho, C.J. Park, Effects of sigma and chi phases on the localized corrosion resistance of SR50A super austenitic stainless steel, Corrosion, 69 (2013) 364-371.

[32] K. Arioka, T. Yamada, T. Terachi, G. Chiba, Influence of carbide precipitation and rolling direction on intergranular stress corrosion cracking of austenitic stainless steels in hydrogenated high-temperature water, Corrosion, 62 (2006) 568-575.

[33] S.Y. Persaud, A. Korinek, J. Huang, G.A. Botton, R.C. Newman, Internal oxidation of alloy 600 exposed to hydrogenated steam and the beneficial effects of thermal treatment, Corros. Sci., 86 (2014) 108-122.

[34] K. Arioka, T. Yamada, T. Miyamoto, T. Terachi, Dependence of stress corrosion cracking of alloy 690 on temperature, cold work, and carbide precipitation—role of diffusion of vacancies at crack tips, Corrosion, 67 (2011) 035006-1-035006-18.

[35] Y. jiao, J. Mahmood, W. zheng, P.M. Singh, J. Kish, Effect of thermal ageing on the intergranular stress corrosion cracking susceptibility of type 310S stainless steel, Manuscript submitted for publication.

[36] Y. Jiao, Q. Wang, W. zheng, J. Mcdermid, M. daymound, J. kish, Effect of thermal ageing on grain boundary hardening of type 310S stainless steel, Manuscript submitted for publication.

[37] Y. Jiao, J. Kish, W. Zheng, D. Guzonas, On the role of grain boundary chemistry

in the intergranular stress corrosion cracking susceptibility of 310S exposed in supercritical water, in: The 7th International Symposium on Supercritical Water-Cooled Reactors, Proc. ISSCWR-7, Helsinki, Finland, 2015.

[38] Y. Jiao, Q. Wang, W. Zheng, D. Guzonas, M. Daymound, J. Kish, Constructing a grain boundary sensitization-embrittlement map for type 310S stainless steel fuel cladding in the Canadian SCWR concept, in: Canadian Nuclear Society, Toronto Marriott Downtown Eaton Centre Hotel, Toronto, ON, Canada, 2016.

[39] Z. Jiao, J. Busby, R. Obata, G. Was, Influence of localized deformation on irradiation-assisted stress corrosion cracking of proton-irradiated austenitic alloys, in: 12th International conference on environmental degradation of materials in nuclear pPower systems—water reactors. Salt Lake City, Utah, 2005.

[40] S. Teysseyre, Z. Jiao, E. West, G. Was, Effect of irradiation on stress corrosion cracking in supercritical water, J. Nucl. Mater., 371 (2007) 107-117.

[41] S. Teysseyre, G.S. Was, Stress corrosion cracking of austenitic alloys in supercritical water, Corrosion, 62 (2006) 1100-1116.

[42] G. Was, P. Ampornrat, G. Gupta, S. Teysseyre, E. West, T. Allen, K. Sridharan, L. Tan, Y. Chen, X. Ren, Corrosion and stress corrosion cracking in supercritical water, J. Nucl. Mater., 371 (2007) 176-201.

[43] Y. Tsuchiya, F. Kano, N. Saito, M. Ookawa, J. Kaneda, N. Hara, Corrosion and scc properties of fine grain stainless steel in subcritical and supercritical pure water, in:

Corrosion 2007, March 11, 2007 - March 15, 2007, National Assoc. of Corrosion Engineers International, Nashville, TN, United states, 2007, pp. 074151-0741513.

[44] Y. Tsuchiya, N. Saito, A. Shioiri, S. Kasahara, K. Moriya, Scc properties of metals under supercritical water cooled power reactor conditions, in: Corrosion 2004, NACE International, 2004.

[45] Y. Watanabe, H. Abe, Y. Daigo, R. Fujisawa, M. Sakaihara, Effect of physical property and chemistry of water on cracking of stainless steels in sub-critical and supercritical water, in: Key engineering materials, Trans. Tech. Publ., 2004, pp. 1031-1036.

[46] J.M. Cookson, G.S. Was, P.L. Andresen, Oxide-induced initiation of stress corrosion cracking in irradiated stainless steel, Corrosion, 54 (1998) 299-312.

[47] A. Luft, Microstructural processes of plastic instabilities in strengthened metals, Prog. Mater. Sci., 35 (1991) 97-204.

[48] Z. Jiao, G.S. Was, Localized deformation and iascc initiation in austenitic stainless steels, J. Nucl. Mater., 382 (2008) 203-209.

[49] Z. Jiao, G.S. Was, Impact of localized deformation on IASCC in austenitic stainless steels, J. Nucl. Mater., 408 (2011) 246-256.

[50] Z. Jiao, J.T. Busby, G.S. Was, Deformation microstructure of proton-irradiated stainless steels, J. Nucl. Mater., 361 (2007) 218-227.

[51] J.T. Barnby, The initiation of ductile failure by fractured carbides in an austenitic

stainless steel, Acta Mater., 15 (1967) 903-909.

[52] M. Gell, P.J. Worthington, The plastic deformation and fracture of iron-3% silicon in the temperature range 295°k–473°k, Acta Mater., 14 (1966) 1265-1271.

[53] J. Lee, Y. Earmme, H. Aaronson, K. Russell, Plastic relaxation of the transformation strain energy of a misfitting spherical precipitate: Ideal plastic behavior, Metall. Mater. Trans. A, 11 (1980) 1837-1847.

[54] A. Argon, J. Im, R. Safoglu, Cavity formation from inclusions in ductile fracture, Metall. Mater. Trans. A, 6 (1975) 825-837.

[55] K. Arioka, 2014 whitney award lecture: Change in bonding strength at grain boundaries before long term SCC initiation, in: Corrosion, 2014, pp. 403-419.

[56] K. Arioka, T. Miyamoto, T. Yamada, T. Terachi, Formation of cavities prior to crack initiation and growth on cold-worked carbon steel in high-temperature water, Corrosion, 66 (2010) 015008-015008-015014.

[57] L. Zhang, K. Chen, D. Du, W. Gao, P.L. Andresen, X. Guo, Characterizing the effect of creep on stress corrosion cracking of cold worked alloy 690 in supercritical water environment, J. Nucl. Mater., 492 (2017) 32-40.

[58] P.L. Andresen, Emerging issues and fundamental processes in environmental cracking in hot water, Corrosion, 64 (2008) 439-464.

[59] A. Paskin, K. Sieradzki, D. Som, G. Dienes, Environmentally induced crack nucleation and brittle fracture, Acta Mater., 30 (1982) 1781-1788.

[60] K. Sieradzki, R. Newman, Brittle behavior of ductile metals during stress-corrosion cracking, Philos. Mag. A, 51 (1985) 95-132.

8. Conclusions

The influence of thermal ageing on the corrosion and stress corrosion cracking susceptibility of Type 310S austenitic stainless steels exposed in supercritical water environments was investigated. The motivation for this study is the exiting knowledge gap associated with these two material performance aspects, which are considered essential to help guide the selection of a fuel cladding material for application in the Canadian Gen IV SCWR design concept. The focus was placed on the pressurized light water coolant outlet conditions (25 MPa SCW at 500-550 °C) considering that the likelihood for corrosion and SCC in combination with microstructure instability resulting from thermal ageing is presumed to be relatively high. Two limiting thermal ageing treatments were evaluated. The ‘S’ treatment, designed to ‘sensitize’ the microstructure, induced significant Cr-rich $M_{23}C_6$ carbide precipitation on the grain boundaries concomitant with the development of adjacent Cr-depleted zones. This limiting case represented a short-term exposure condition for the fuel cladding. The ‘TT’ treatment, designed to ‘mechanically embrittle’ the microstructure, induced significant Cr-rich sigma (σ)-phase precipitate formation on the grain boundaries and within the grains. This limiting case represented a long-term exposure condition for the fuel cladding. The ‘SA’ treatment, designed to solution anneal the microstructure, served as the baseline microstructure exhibiting a low extent of microstructure instability.

The research conducted to evaluate the influence of long term thermal ageing on the general corrosion/oxidation susceptibility of Type 310S austenitic stainless steel in SCW was reported in Chapter 4. The major finding of this part of the thesis can be summarized as:

- Long term thermal ageing of Type 310S stainless steel at the maximum expected fuel cladding temperature induced significant σ phase precipitate formation within the grains and on grain boundaries, all without the concomitant adjacent Cr-depleted zone formation.
- Relatively large intermetallic σ phase precipitates embedded at the oxide scale/alloy interface were observed to significantly reduce the thickness of the oxide layer residing directly on top of it. This is attributed to the formation of a more protective corundum-type M_2O_3 oxide scale on the Cr-rich intermetallic precipitates.
- The significant σ phase precipitate formation did not have a major effect on the general corrosion/oxidation susceptibility since the thermally-aged material exhibited a similar weight gain and oxide scale structure as the solution annealed material. The likely reason for this was the discontinuous nature of the σ phase precipitate formation.
- Of the test parameters under study, alloying was found to have the more pronounced effect on the corrosion/oxidation susceptibility than the combined

effect of dissolved oxygen and flow. The lower corrosion/oxidation susceptibility (weight gain) exhibited by Type 310S stainless steel, in comparison with Type 316L stainless steel, is associated with the presence of a more protective chromia inner layer in the oxide film.

The remaining research conducted was aimed towards investigating the effect of thermal ageing on the intergranular SCC susceptibility of Type 310S stainless steel in SCW. A 'first approximation' attempt to isolate and assess the potential contribution of the likely chemical factor (sensitization) and mechanical factor (embrittlement) to the overall cracking mechanism. The chemical factor (sensitization) was isolated and assessed first, with the research results presented and discussed in Chapter 5. The mechanical factor (embrittlement) isolated and assessed next, with the research results presented and discussed in Chapter 6. A summary of the major conclusions from both chapters is provided below.

- Both limiting thermal ageing treatments were successful in producing the intended microstructure instability expected of a Type 310S stainless steel fuel cladding in service: Cr-rich $M_{23}C_6$ precipitate formation on the grain boundaries in the S material (limiting short-term sensitization exposure) and relatively large σ phase precipitate formation on the grain boundaries in the TT material (limiting long-term embrittlement exposure). TEM-EDS analysis revealed the presence of a well-developed Cr-depleted zone in the S material and the absence of such a zone in the TT material.

- The overall ranking in terms of an increasing degree of sensitization, as determined by DL-EPR testing, of three heat treatments studied is: SA ~ TT << S. The ranking reflects the controlling role played by Cr-depleted zones, which were only observed in the S material. The absence of a Cr-depleted zone accompanying the σ phase grain boundary precipitates in the TT material indicates that the treatment time of a 1000 h was sufficient to “self-heal” the Cr-depleted zone, which was expected to have formed during the early stages of the treatment at 800 °C.
- SSRT conducted in a hot alkaline solution readily showed an intergranular SCC susceptibility of the S material, consistent with the associated sensitized microstructure (exhibiting a well-developed Cr-depleted zone formation adjacent to grain boundaries). The relatively large σ phase grain boundary particles in the TT material preferentially cracked during SSRT in both the hot dry sand and hot alkaline solution indicating that the preferential cracking was controlled by mechanical factors only. The absence of Cr-depleted zone formation adjacent to grain boundaries prevented intergranular SCC from developing in the hot alkaline solution. Bulk fracture of this material occurred via a transgranular mixed-mode process.

- Bulk uniaxial tensile measurements revealed both the S and TT material were embrittled relative to the SA material. The associated fractography revealed that the grain boundaries in the S material were sufficiently embrittled to cause intergranular fracture, whereas the grain boundaries in the TT material were not sufficiently embrittled to cause intergranular fracture.
- Classic micro-void formation involving a $M_{23}C_6$/matrix decohesion process occurs on the S material grain boundaries. Intergranular facture occurs as these micro-voids coalesce on the grain boundaries. In contrast, micro-void formation involving cracking of the large hard σ phase precipitates occurs on the TT material grain boundaries. Transgranular ductile fracture of the softer austenite matrix occurs as these micro-voids coalesce across the grains as the softer grains need to accommodate the stress after fracture of hard σ phase precipitates.
- Less localized deformation damage is expected to be accumulated at grain boundaries in the TT material resulting from slip than either in the SA or S material for the same level of bulk uniform plastic strain because ability of the coarse σ phase precipitates to effectively block slip.

Finally, Chapter 7 investigates the effect of thermal ageing on the SCC susceptibility of Type 310S in SCW. SCC was evaluated using the SSRT technique, straining samples to 10% in a flowing autoclave test facility using 25 MPa SCW at 500 °C with 20 ppm dissolved oxygen. The results were interpreted in light of the likely contributions of the chemical (sensitization) and mechanical (embrittlement) factors extracted from the conclusions of Chapter 5 and Chapter 6 respectively. A summary of the major conclusions are provided below.

- The sensitized (SA and S) material exhibited well-developed intergranular SCC after straining to 10% (about 7.5% plastic strain). The TT material exhibited neither an inter-granular nor transgranular SCC susceptibility under the same exposure conditions. The *in-situ* sensitization of the starting SA material reveals that such microstructure stability can be expected at relative short exposure times (about 100 h) at temperature as low as 500°C.
- The significant difference in SCC susceptibility is believed to be related to the extent of localized deformation that accumulates at the grain boundaries during plastic deformation, which in turn depends upon the size and possibly type of precipitate that is decorating the grain boundaries. In this context, coarse-scale σ phase precipitates (TT material) are more effective than fine-scale $M_{23}C_6$ precipices (SA and S material) in accommodating localized deformation at grain boundaries by preferentially cracking.
- Void formation associated with carbide precipitates was observed on grain boundaries ahead of the crack tip in the sensitized (SA and S) material. The formation process is believed to be involved deformation-induced decohesion

of the precipitate/matrix interface rather than a strain gradient assisted diffusion of deformation-induced vacancies.

- The localized deformation model for SCC initiation and a void-assisted film-cleavage model for SCC propagation can be used to explain the SCC susceptibility of thermally-aged Type 310S stainless steel in SCW.

Collectively the research findings provide a knowledge framework from which strategies to mitigate general corrosion/oxidation and SCC of a Type 310S fuel cladding exposed in the SCW coolant of the Canadian GEN-IV SCWR design concept can be developed. Some possible strategies are described below.

- A promising corrosion/oxidation mitigation strategy would be to modify the surface in a manner that could produce a continuous layer of the σ phase. As the phase is quite brittle, the key to mitigating corrosion/oxidation to the underlying stainless steel substrate would be the ‘self-healing’ tendency of the phase to form a protective Cr_2O_3 scale in any cracks that would develop in service. Such a layer may also prove beneficial in mitigating the SCC susceptibility as well by preferentially cracking to alleviate and localized deformation-induced crack initiation at grain boundaries. Again, the key to the strategy would be for the cracked σ phase to rapidly ‘self-heal’ by forming a protective Cr_2O_3 scale in the cracks.
- One promising strategy to mitigate the SCC susceptibility would be to

replicate the TT condition, in which a coarse hard phase was present on the grain boundaries that would be preferentially cracked under applied loads during service to effectively alleviate localized deformation accumulation at grain boundaries. The more obvious, but likely impractical, means is to thermally-aged the Type 310S fuel cladding to TT condition as a pre-treatment.

- Another promising strategy to mitigate the SCC susceptibility is to circumvent the formation of the Cr-depleted zone during service. Possibilities here include a stabilized version of Type 310S stainless steel, either chemically by alloying with a stronger carbide forming element than Cr or thermally by applying a heat treatment designed to promote $M_{23}C_6$ carbide formation on the grain boundaries without concomitant Cr-depleted zone formation.

It is worth mentioning here that thermal ageing (as researched in this thesis) is one aspect of the microstructure instability that is expected to occur with a Type 310S fuel cladding. The other aspect, as discussed in Chapters 1 to 3, is irradiation damage accumulation. A similar research program as used in this thesis needs to be conducted using pre-irradiated Type 310S stainless steel to addresses the exiting knowledge gap surrounding this aspect. Of particular value would be the systematic study of the combined effects of thermal ageing and irradiation damage.